

BINARY INFORMATION FROM OPEN CLUSTERS USING SEDS (BINOCS)
PROJECT: THE DYNAMICAL EVOLUTION OF THE BINARY POPULATION IN
CLUSTER ENVIRONMENTS

by

BENJAMIN A THOMPSON

Bachelor of Arts, 2010
Ohio Wesleyan University
Delaware, Ohio

Submitted to the Graduate Faculty of the
College of Science and Engineering
Texas Christian University
in partial fulfillment of the requirements
for the degree of

Doctor of Philosophy

May 2015

BINARY INFORMATION FROM OPEN CLUSTERS USING SEDS (BINOCS)
PROJECT: THE DYNAMICAL EVOLUTION OF THE BINARY POPULATION IN
CLUSTER ENVIRONMENTS

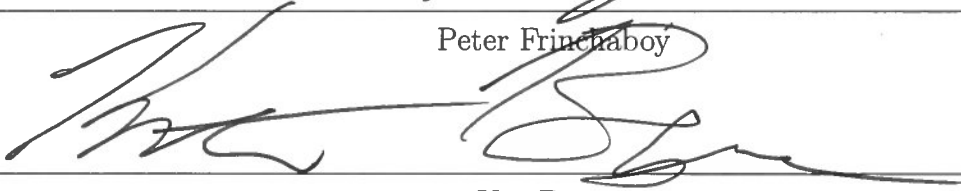
by

Benjamin A Thompson

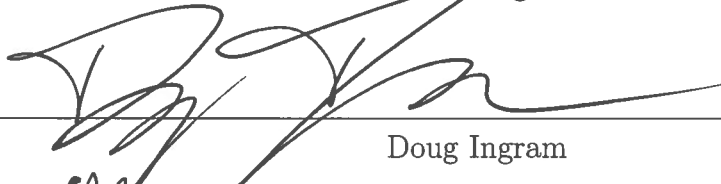
Dissertation Approved:



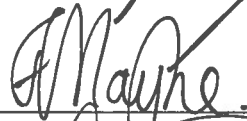
Peter Frinchaboy



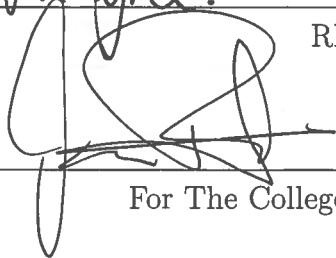
Kat Barger



Doug Ingram



Rhiannon Mayne



For The College of Science and Engineering

ACKNOWLEDGEMENTS

I would never have been able to finish (or start) my dissertation without guidance from many others; first and foremost my wife, who celebrated my research gains every day, even though most of the time she had no idea what I was rambling about.

I would like to thank Dr. Peter Frinchaboy for coming up with the idea for this project, setting me along the path, and constantly supporting me throughout my graduate school journey. I also thank him for constantly interrupting that journey with his many side projects, without which I would not have been able to pursue my future career.

I would like to thank Dr. Ata Sarajedini, Dr. Aaron Geller, and the other members of the WOCS consortium who did much of the heavy lifting for this work on outside projects, and quickly transferred that data and knowledge to me.

Lastly, I would like to thank my friends, inside and outside the lab, who made it an enjoyable five years in Texas.

Contents

List of Terms	1
1 Introduction	2
1.1 Basic Astrophysics	2
1.1.1 The Magnitude System	2
1.1.2 Filter Systems	5
1.1.3 Color-Magnitude Diagrams & Stellar Evolution	9
1.1.4 Metallicity	13
1.1.5 Interstellar Reddening	15
1.1.6 Star Clusters	16
1.1.7 Binary Star Systems	19
2 Science Questions	27
3 BINOCS	31
3.1 Current Binary Detection Techniques	31
3.1.1 Two-Band Photometry	31
3.1.2 Radial Velocity Studies	34
3.2 The BINOCS Method	36
3.3 The BINOCS Code	38
4 Data Overview	42
4.1 Instrumentation and Processing	42
4.1.1 Visual Wavelength Detectors	42
4.1.2 Infrared Wavelength Detectors	43
4.1.3 Image Reduction	44
4.1.4 Magnitude Measurements	46
4.2 Cluster Sample	49
4.3 Available Data	51
4.3.1 Optical Data Sources [0.3 – 1.0 μm]	51
4.3.2 Near-Infrared Data Sources [1.0 – 2.5 μm]	57
4.3.3 Mid-Infrared Data [2.5 – 10 μm]	65
4.3.4 Membership Data	68
4.3.5 Data Overview	70

5	Isochrone Systems	72
5.1	Isochrone Physics	73
5.2	Comparison to CMDs	74
5.3	Isochrone Preparation	76
5.3.1	Metallicity	76
5.3.2	Age	77
5.3.3	Atmospheres	77
5.4	Empirical Ridgelines	79
5.5	Comparison	80
5.5.1	M37	82
5.5.2	NGC 2420	83
5.5.3	M67	85
5.6	Isochrone Adjustment	87
6	BINOCS Testing	89
6.1	Number of Iterations	89
6.2	Close Filter Threshold	91
6.3	Number of Required Filters	93
6.4	Minimum Mass Ratio	95
6.5	Comparison to RV	98
6.5.1	Binary Classification	98
6.5.2	Mass Determination	102
7	BINOCS Results	105
7.1	Binary Fraction Versus Age	106
7.2	Binary Fraction Versus Metallicity	107
7.3	Binary Fraction Versus Galactocentric Radius	108
8	Radial Migration of Binary Systems	110
8.1	Mass Segregation	110
8.2	Binary Segregation	111
8.3	BINOCS Radial Profiles	115
8.3.1	NGC 1960 (M36)	118
8.3.2	NGC 2168 (M35)	118
8.3.3	NGC 2099 (M37)	119
8.3.4	M67	121
8.4	Comparison to NGC 1818	122
8.5	Discussion	124
9	Summary & Future Work	125
A	Empirical Ridgelines	129
	Vita	
	Abstract	

List of Figures

1.1	Filter functions	8
1.2	Hubble Space Telescope color-magnitude diagram	10
1.3	Illustration of eclipsing binary system	21
1.4	Inclination effect on observed radial velocities	24
3.1	Position of binaries on CMD	33
3.2	BINOCS method example	37
4.1	Example of aperture photometry	47
4.2	Example of PSF photometry	48
4.3	Distribution of cluster sample ages and metallicities	50
4.4	SDSS telescope and camera	52
4.5	Example MOSAIC image	54
4.6	MOSAIC photometric quality plots	56
4.7	MOSAIC transformation residuals	58
4.8	2MASS instrumentation diagram	59
4.9	NEWFIRM 4Q-mode description	60
4.10	Example NEWFIRM images	62
4.11	NEWFIRM photometric quality plots	63
4.12	IRAC-to-WISE residuals	67
5.1	Comparison of isochrone systems to M37	75
5.2	Example of empirical ridgelines	80
5.3	Isochrone-to-empirical ridgeline residuals for M37	81
5.4	Isochrone-to-empirical ridgeline residuals for NGC 2420	84
5.5	Isochrone-to-empirical ridgeline residuals for M67	86
6.1	BINOCS iterations test results	91
6.2	BINOCS threshold test results	93
6.3	BINOCS minimum mass ratios for M37	97
6.4	BINOCS minimum mass ratios for M67	97
6.5	Comparison of RV and BINOCS results for M35	99
6.6	Comparison of RV and BINOCS results for M67	100
6.7	Comparison of BINOCS and RV-derived mass ratios for NGC 188	103
6.8	Comparison of BINOCS and RV-derived mass ratios for NGC 6819	103
7.1	Binary fraction versus cluster age	106

7.2	Binary fraction versus cluster metallicity	107
7.3	Binary fraction versus cluster R_{gc}	108
8.1	Previous NGC 1818 results	112
8.2	N-Body simulation binary radial profiles	113
8.3	BINOCs derived binary radial distributions for all clusters	116
8.4	BINOCs binary radial distributions in M36	118
8.5	BINOCs binary radial distributions in M35	119
8.6	BINOCs binary radial distributions in M37	120
8.7	BINOCs binary radial distributions in M67	121
8.8	Comparison of BINOCs results in M37 to NGC 1818 Elson et al. results .	122
8.9	Comparison of BINOCs results in M37 to NGC 1818 de Grijs et al. results	123

List of Tables

1.1	List of standard filter centers and wavelengths	7
1.2	Extinction values	16
4.1	Dataset cluster parameters	50
4.2	MOSAIC transformation coefficients	57
4.3	NEWFIRM observing log	61
4.4	NEWFIRM transformation coefficients	64
4.5	Available data for cluster sample	70
4.6	Possible analysis for each cluster in sample	71
5.1	Isochrone input physics	74
5.2	Sample of BT-Settl color-temperature grid	78
6.1	Number of filters test results	94
6.2	Confusion matrix between RV and BINOCS results for M35	98
6.3	Confusion matrix between RV and BINOCS results for M67	98
7.1	Overall binary fractions for analyzed clusters	105
8.1	Spectral class mass ranges	117
9.1	Comparison of classified stars in RV studies to BINOCS	125
A.1	Empirical ridgelines for M36	129
A.2	Empirical ridgelines for M35	130
A.3	Empirical ridgelines for M37	131
A.4	Empirical ridgelines for M67	132
A.5	Empirical ridgelines for NGC 2420	133

List of Terms

CMD	<i>Color-Magnitude Diagram.</i> Observational form of H-R Diagram, usually used for star clusters.
H-R Diagram	Plot of stellar temperature against luminosity. Separates stars into defined evolutionary phases.
2MASS	<i>Two-micron All Sky Survey.</i> Near-IR (JHK_S filter, 1-3 μm) all-sky photometric survey.
WISE	<i>Wide-field Infrared Survey Explorer.</i> Mid-IR ([3.4][4.6], 3-5 μm) all-sky photometric survey space telescope.
IR	<i>Infrared.</i> This work is concerned with IR wavelengths from 1-8 μm .
CCD	<i>Charge-Coupled Device.</i> Detector type used for most optical-wavelength observations.
NGC	<i>New General Catalogue.</i> Catalog of 7,840 deep-sky objects, including most of the open clusters considered in this work.
RV	<i>Radial Velocity.</i> Line-of-sight doppler shift.
SED	<i>Spectral Energy Distribution.</i> Integrated flux profile of a star across considered filters. As a first approximation, a blackbody curve.

Chapter 1

Introduction

1.1 Basic Astrophysics

1.1.1 The Magnitude System

Ancient astronomers found it beneficial to classify the stars they observed in the night sky. The Greek astronomer Hipparchus grouped all observable stars into 6 *magnitude* groups: magnitude 1 stars were the brightest, while magnitude 6 stars were the dimmest observable with the naked eye. With the advent of sensitive observing equipment, it was discovered that magnitude 1 stars were 100 times brighter than magnitude 6 stars. From this historical groundwork, the magnitude system was defined: a difference of 5 magnitudes corresponds to a factor of 100 in brightness. With modern telescopes and sensitive observing equipment, astronomers can observe stars that are much dimmer than 6th magnitude, opening up the magnitude scale to high positive magnitudes. The Hubble

Space Telescope has a limiting magnitude of roughly 30; stars that are one billionth as bright as what can be seen with the naked eye.

A magnitude increase of 1 corresponds to a brightness difference of $\sqrt[5]{100}$; the magnitude difference between stars will be a logarithm of the ratio of fluxes with a base of $\sqrt[5]{100}$. To determine the difference in magnitudes of two different stars (A and B):

$$m_A - m_B = -\log_{\sqrt[5]{100}} \left(\frac{F_A}{F_B} \right) \quad (1.1)$$

Converting to more familiar \log_{10} ,

$$m_A - m_B = -\log_{\sqrt[5]{100}} \left(\frac{F_A}{F_B} \right) = -\frac{\log_{10} F_A/F_B}{\log_{10} \sqrt[5]{100}} = -2.5 \log_{10} \left(\frac{F_A}{F_B} \right) \quad (1.2)$$

Equation (1.2) defines magnitudes relative to one another, and a zero point is required to complete the scale. There are three different conventions for handling the magnitude scale zero point:

Vega System: Historically, the star Vega was chosen to have a magnitude of 0, with all other stars measured relative to it. Due to uncertainties in flux measurements, however, Vega's magnitude has been refined over time. While the defined zero point of the magnitude scale has stayed the same, Vega now has a magnitude of 0.03. The magnitude of a general star in the Vega magnitude system is calculated by:

$$m_{VS} = -2.5 \log_{10} \left(\frac{F}{F_{Vega}} \right) + 0.03 \quad (1.3)$$

AB System: The zero point of the magnitude scale in the AB system is a flat spectrum.

A star in the AB system will have a magnitude:

$$m_{\text{AB}} = -2.5 \log_{10}(F_{\nu}) - 48.6 \quad (1.4)$$

STMag System: The STmag system, used on space telescopes such as Hubble, is analogous to the AB system, but with flux defined as a function of wavelength instead of frequency. As such, the zero point is different:

$$m_{\text{ST}} = -2.5 \log_{10}(F_{\lambda}) - 21.1 \quad (1.5)$$

One issue with the magnitude system, as defined by ancient astronomers, is that star brightness is not intrinsic, but correlated with distance from Earth. Light intensity of a star falls off with an inverse square law. In order to compare stars that may be at different distances, the observed magnitudes, called *apparent magnitudes*, are converted to *absolute magnitudes*. The absolute magnitude of the star is its apparent magnitude if it was located at a distance of 10 parsecs¹ from Earth.

We compare the apparent magnitudes of a generic star at a distance d (in parsecs) and at a distance of 10 parsecs (denoted by a capital M). Using the fact that flux is $L/4\pi r^2$ (inverse square law), the difference in apparent and absolute magnitude is:

$$m - M = -2.5 \left(\log_{10} \frac{L}{4\pi d^2} - \log_{10} \frac{L}{4\pi (10)^2} \right) \quad (1.6)$$

¹A parsec is a geometric astronomical distance unit. It is defined as the distance at which 1 AU (the average distance between the Earth and the Sun) subtends an angle of one arcsecond.

The distance dependence is pulled out of the logarithm, and a majority of the equation cancels.

$$m - M = -2.5 \left(\log_{10} \frac{L}{4\pi} - \log_{10} d^2 - \log_{10} \frac{L}{4\pi} + \log_{10} (10)^2 \right) = -2.5 (\log_{10} (10)^2 - \log_{10} d^2) \quad (1.7)$$

Rearranging and getting rid of exponents gives the absolute magnitude conversion a simple form:

$$m - M = 5 \log_{10} d \text{ (pc)} - 5 \quad (1.8)$$

Equation (1.8) is known as the *magnitude-distance relation*. In apparent magnitude, the Sun dominates the scale with an apparent magnitude of -26.7. In absolute magnitude, however, the Sun is a fairly average 5th magnitude star. Getting distances, and therefore absolute magnitudes, allows for inter-comparison of stars anywhere in the Universe.

1.1.2 Filter Systems

Astronomers use photometric filters to allow only specific wavelengths of light into a detector. *Broadband filters*, which allow relatively wide wavelength ranges (50+ nm) of light through, are created using two panes of glass that are fused together: *cut-on* and *cut-off* layers. The cut-on layer is opaque to short wavelength photons, up to a certain point where it “cuts on” and becomes transparent to longer wavelength photons. The cut-off layer acts oppositely: transparent to short wavelength photons and opaque to long wavelength photons. The combination of these two layers yields a filter where only

a small range of wavelengths are able to pass through. By changing the two layers used, filters with the desired wavelength range can be created.

To allow easy comparison of results between telescopes, there are several standard filter systems to which all other measurements are calibrated. Of particular importance to this project are filter systems that cover the visual and infrared portions of the spectrum.

Optical Filters: This project will utilize two sets of standard filters that cover the optical range of the electromagnetic spectrum, from 300 – 1000 nm. The first filter systems is called the Johnson-Cousins system, consisting of five filters, *UBVRI* (Bessell 1990). Alternatively, there is the Sloan filter system, *ugriz* (Fukugita et al. 1996). Both visual filter systems provide near seamless coverage between 300 – 900 nm, illustrated in figure 1.1. The Sloan filters have much reduced throughput in figure 1.1 due to the fact that the Sloan system includes the filters themselves, the CCD detectors, and the Sloan telescope (described in §4.3.1). The inclusion of the entire optical and detector system vastly reduces the throughput as compared to the actual filter throughput measured for the Johnson-Cousins system.

Near-IR Filters: The 1.0 – 2.5 μm wavelength range is covered by three near-infrared filters that comprise the 2-Micron All Sky Survey (2MASS; Skrutskie et al. 2006) filter system, *JHK_S*. Unlike the visual systems, 2MASS filters do not provide uniform coverage throughout this range. The gaps between the filters, at 1.4 and 1.9 μm , correspond to regions of absorption from water vapor and CO₂ in the atmosphere. These spectral regions would not provide any photons from the star, so the 2MASS filters were designed to avoid sky contamination.

System	Filter	Central λ (nm)	Width (nm)
Johnson-Cousins	<i>U</i>	365	66
	<i>B</i>	445	94
	<i>V</i>	551	88
	<i>R</i>	658	138
	<i>I</i>	806	149
Sloan	<i>u</i>	350	57
	<i>g</i>	480	137
	<i>r</i>	625	137
	<i>i</i>	770	153
	<i>z</i>	910	95
2MASS	<i>J</i>	1235	162
	<i>H</i>	1662	251
	<i>K_S</i>	2159	262
IRAC	[3.6]	3567	776
	[4.5]	4485	1060
	[5.8]	5729	1427
	[8.0]	7893	2901

Table 1.1: Central wavelengths and effective widths of all filters used in this project.

Mid-IR Filters: Beyond $2.5 \mu\text{m}$, absorption from the Earth’s atmosphere becomes so strong that few stellar photons will reach the surface. To overcome this, mid-infrared observations are usually taken from space. The mid-IR standard filter system used in this project, [3.6][4.5][5.8][8.0], are from the Infrared Array Camera (IRAC) on the *Spitzer* Space Telescope (Fazio et al. 2004). Additional data were used from the Wide-Field Infrared Survey Explorer (WISE) (Wright et al. 2010), which is an all-sky mid-IR survey. WISE uses the mid-IR filters of [3.4] and [4.6], very similar to the shorter-wavelength filters for IRAC. In §4.3.3, the WISE filter magnitudes will be transformed into IRAC magnitudes, creating a single mid-IR filter system.

Table 1.1 lists the filters that will be used in this project along with the central wavelengths and approximate width of the transparent region.

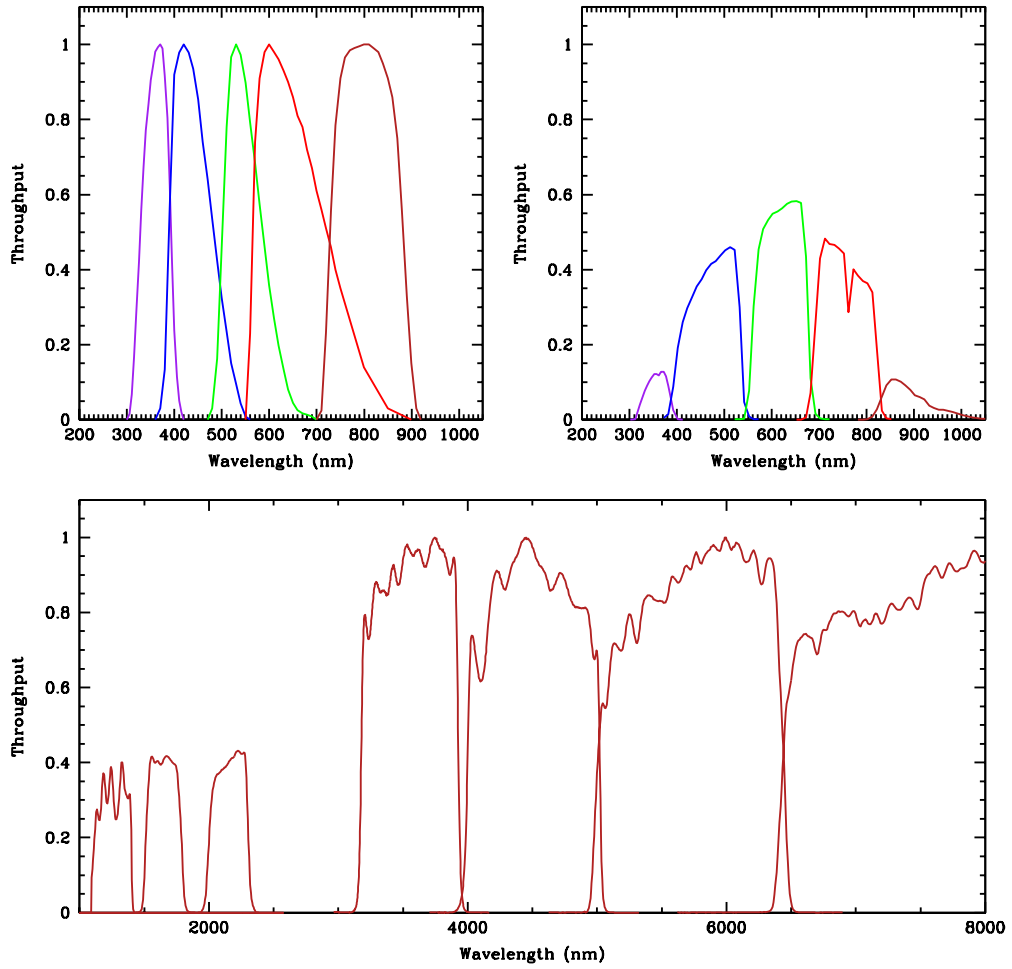


Figure 1.1: Effective ranges of all filters used in this paper. (*Top Left*) Johnson Filters: *UBVRI*. (*Top Right*) SDSS Filters: *ugriz* + CCD + Sloan Telescope. (*Bottom*) 2MASS (which includes detector and telescope effects) and IRAC filters: *JHK_S[3.6][4.5][5.8][8.0]*.

1.1.3 Color-Magnitude Diagrams & Stellar Evolution

Stars go through a variety of stages during their lifetime, and the easiest way to visualize stellar evolution is through the use of a *Hertzsprung-Russell* (H-R) diagram. A H-R diagram plots stars with Luminosity on the y-axis, and Temperature on the x-axis. While a H-R diagram is the easiest way to visualize stars, neither Luminosity nor Temperature is an observed quantity. Instead, we create *color-magnitude* diagrams (CMDs), which plot a filter magnitude on the y-axis and a *color* on the x-axis. A color is calculated by subtracting the magnitude of a star in a higher wavelength filter from the star's magnitude in a lower wavelength filter, e.g. $B - V$ or $V - K$.

CMDs are much easier to create, due to the fact that no other information about the stars need to be known besides their observed magnitude. If other information is known, it is possible to convert a CMD into a H-R diagram. Equation (1.8), along with stellar models, can be used to convert a filter magnitude to an absolute magnitude and then to a luminosity. A color is related to temperature due to the fact that bluer (hotter) stars will have a negative color, while a red star (cooler) will have a positive color. Using known relations, colors of stars can be transformed into temperatures, if needed.

While H-R diagrams can be plotted for any collection of stars, CMDs are usually created for star clusters (to be discussed later in section 1.1.6). A CMD of Hubble Space Telescope data for a cluster is plotted in figure 1.1.3. Stages of stellar evolution are labeled 1 through 5. The list below explains what changes the star is experiencing during each stage of evolution.

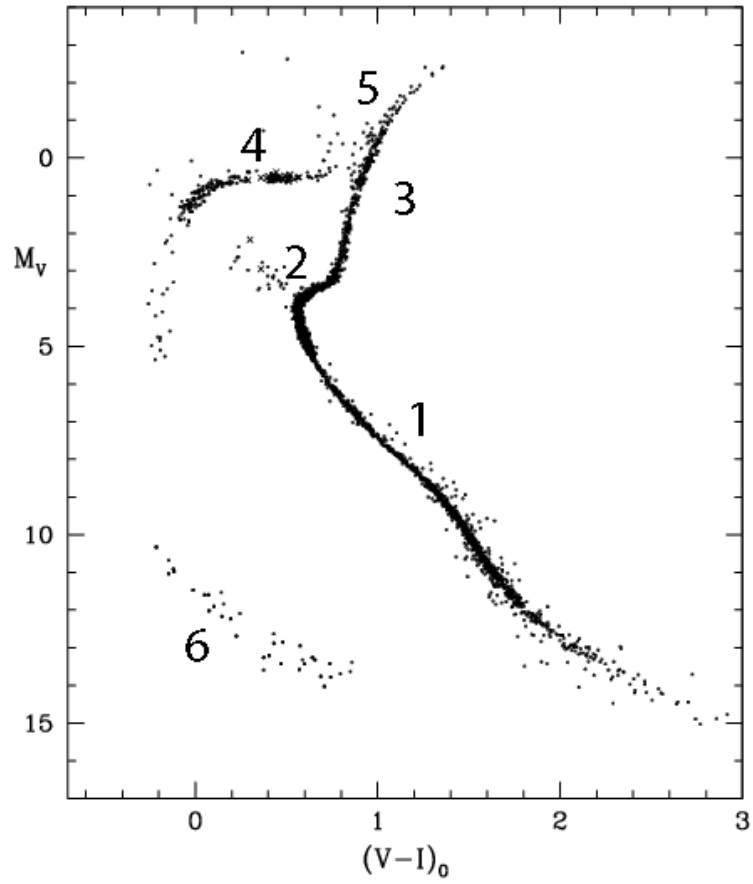


Figure 1.2: Hubble Space Telescope CMD for a globular cluster. Evolutionary stages are labeled.

1. **The Main Sequence (MS):** For a majority of a star's life, hydrogen to helium conversion in the core is the main source of energy. During this phase, the star is located on a region of the CMD called the *main sequence*. Larger mass stars are brighter and hotter than lower mass ones, and are therefore located at the top of the MS. As the hydrogen fuel in its core begins to become depleted, a star cools slightly, moving right on the CMD. For the most part, however, MS stars are located in a well-defined sequence in the CMD.
2. **Turnoff + Subgiant branch:** When hydrogen in the star's core becomes depleted, it can no longer create enough energy to sustain the weight of the layers above it, and the core begins to collapse. These stars have completed their time on the main sequence, and can be seen on the CMD at the *turnoff point*. As the core collapses and releases gravitational energy, a shell of hydrogen around the core begins to heat until hydrogen fusion begins in the shell. As the shell has more volume than the core below it, the increased energy output expands the outer layers of the star, cooling it and increasing its brightness as it moves through the *subgiant branch*. During this phase and the next, the hydrogen-depleted core remains inert.
3. **Red Giant Branch (RGB):** As the shell continues to convert hydrogen to helium, the stellar atmosphere opacity increases due to the decrease in temperature and, thus, increase in H^- ions. This opacity increase leads to convection becoming the most efficient energy transport method and convection cells forming near the surface. The increase in energy transport efficiency leads to an increase in luminosity as well as causing the outer layers of the star to expand again. This expansion

causes the temperature to decrease even more, and the entire cycle repeats. As stars near the tip of the RGB, they become so large that their outer layers may be blown off by stellar winds. While all stars experience mass loss during their ascent of the RGB, the mass loss rates for some stars can be substantial, exceeding nearly 25% of the total mass.

During the RGB phase, the inert core of the star continues to collapse and heat until the temperature is high enough to begin helium fusion. While some stars gradually enter the next phase of evolution, some stars begin helium fusion nearly simultaneously throughout the core in a *helium flash*.

4. **Horizontal Branch (HB):** With core temperatures now high enough to convert helium into Carbon, the *horizontal branch* evolutionary phase is the helium analogue of the hydrogen main sequence. The star remains almost stationary on the CMD as it converts all of the helium within the core. As there is much less helium within the star than hydrogen, the timescale of the horizontal branch is much less than that of other evolutionary phases.

There are two distinct halves of the horizontal branch, a red and blue section (visible in figure 1.1.3). The difference between these sections is not completely understood, but is thought to be related to the mass loss of the star along the RGB. If the outer layers of the star are lost near the tip of the RGB, we are observing further into the star than if there was no mass loss, leading to a higher observed temperature and bluer color.

5. **Asymptotic Giant Branch (AGB):** As the HB is an analogue of the MS, the asymptotic giant branch is the helium analogue of the RGB. Named because it approaches the RGB asymptotically from the left of the CMD, the AGB contains stars that are burning helium in a shell around the core and are at least partly convective.

6. **Post AGB Evolution:** While a star is on the AGB, it experiences a high rate of mass loss. Strong stellar winds continue after the star reaches the tip of the AGB, blowing off most of the star's outer cooler layers, leaving only the hotter inner regions. Since the star's helium shell continues burning, the luminosity stays the same. This results in the star tracking blueward at the top of the CMD. When only a small layer of material remains on top of the helium burning shell, the temperature drops rapidly and fusion stops. The star's luminosity drops rapidly, and the star ends its life as a white dwarf on the bottom left of the CMD.

The AGB to white dwarf transition only happens for medium to low mass stars, less than $8 M_{\odot}$. Higher mass stars will end their lives in supernovae explosions, ending as either a neutron star or black hole. The transition to these stellar remnants is beyond the scope of this work.

1.1.4 Metallicity

A star's *metallicity* is an important quantity when determining its properties. Astronomers consider anything besides hydrogen and helium to be “metals”. Metallicity is the fraction of mass within a star that is metals, and is often denoted by the letter

Z^2 . The Sun has a metallicity of $Z = 0.0188$, meaning that slightly less than 2% of the mass of the Sun is comprised of something heavier than helium. While denoting a star's metallicity using Z is fairly common, it can also be expressed in terms of dex, which is the log of the ratio of the star's Z to the Sun's. Given a metallicity of N dex, Z can be found using:

$$Z_{star} = Z_{\odot} \times 10^{N \text{ dex}} \quad (1.9)$$

While the term metallicity is most often used to describe the overall metal content of the star, metallicity can also refer to the abundance of particular elements within the star. Usually the ratios of these elements are consistent, but sometimes anomalous stars will be observed with certain elements far more abundant than predicted. Individual elemental abundances are calculated as ratios of that element to hydrogen, and then calibrated to the Sun's value (similar to the dex definition). For iron, its abundance is written as $[\text{Fe}/\text{H}]$ and calculated by:

$$[\text{Fe}/\text{H}] = \log \frac{(N_{\text{Fe}}/N_{\text{H}})_{Star}}{(N_{\text{Fe}}/N_{\text{H}})_{\odot}} \quad (1.10)$$

Metallicity measurements will not be the focus of this project, but are essential in computing accurate comparison stellar models. Metallicity information used in the analysis will be gathered from outside sources.

²Astronomers define the chemical makeup of stars using the parameters X, Y and Z. X = mass fraction of hydrogen, Y = mass fraction of helium, Z = mass fraction of metals.

1.1.5 Interstellar Reddening

Interstellar space contains gas and dust that scatters and absorbs stellar photons. The scattering of light by interstellar gas causes two related effects: *extinction* due to the fact that photons being absorbed or scattered by gas means that the star will appear dimmer than it actually is, and *reddening* due to the fact that shorter (bluer) wavelengths are scattered more than longer wavelengths, altering the color of the star so that is measured to be redder than it actually is.

Extinction is denoted using the term A_X , where X is the specific band you are interested in, and is calculated using:

$$A_X = (M_X)_{\text{intrinsic}} - (M_X)_{\text{observed}} \quad (1.11)$$

Extinction adds another term to equation (1.8), converting the magnitude-distance relation to:

$$m_X - M_X = 5 \log_{10} d - 5 + A_X \quad (1.12)$$

Reddening for a given color, say $B - V$, is denoted by the value $E(B - V)$:

$$E(B - V) = (B - V)_{\text{intrinsic}} - (B - V)_{\text{observed}} = A_B - A_V \quad (1.13)$$

Extinction and reddening are intertwined effects, as seen in equation (1.13), and have been related experimentally. This is done by comparing spectra of two stars of the same spectral type: one which is not reddened, and the other which is observed through dust.

Filter	A_X/A_V	Source
U	1.531	Binney & Merrifield (1998)
B	1.324	
V	1.000	
R	0.748	
I	0.482	
u	1.593	Fan (1999)
g	1.199	
r	0.858	
i	0.639	
z	0.459	
J	0.282	Binney & Merrifield (1998)
H	0.175	
K_S	0.112	
[3.6]	0.063	Chapman et al. (2008)
[4.5]	0.048	
[5.8]	0.048	
[8.0]	0.048	

Table 1.2: Extinction Relations in Relevant Filters

The stars are assumed to have similar physical properties, but the flux from the reddened star will be less than that from the non-reddened one.

It was found that galactic extinction curves (extinction vs wavelength) could be approximated by an analytic function with a single variable: $R_V = A_V/E(B - V)$, the total-to-selective extinction ratio (Cardelli et al. 1989). For the nearby regions of the Milky Way being explored, an assumption of the galactic average, $R_V = 3.1$, is acceptable. Extinction values for visual and near-IR filters used in this project are listed in table 1.2.

1.1.6 Star Clusters

A star cluster is a gravitationally-bound collection of stars that formed from the same large cloud of interstellar gas at roughly the same time, and are fundamentally important

in astrophysics, due to the fact that they are some of the only reliably age-dateable objects in the known Universe.

Of all the parameters that determine the observable properties of a star, age is the hardest to determine. Metallicity can be measured through spectroscopy, distance can be found using parallax (for close stars), but determining the age of a single star is near-impossible. The Sun — the star we know the most about — is dated through radioactive dating analyses of meteorites instead of through direct measurements.

Most stellar clusters are assumed to have a common age and homogeneous chemical composition. A cluster's distance from Earth is usually much larger than the size of the cluster, and therefore it can be approximated that all stars are at the same distance. It is also assumed that all stars within a cluster have their light pass through the same line of sight to Earth. Any gas clouds that redden the light from one star in the cluster will have the same effect on all stars in the cluster. There are clusters that experience *differential reddening*, where reddening throughout the cluster is not constant, but for the most part this assumption holds.

While field stars will have varying values of metallicity, age, distance and reddening, star clusters will have a single set of parameters for all stars. Using the cluster as a uniform ensemble, age determinations are possible, allowing for the correlation of many stellar properties with time.

Star clusters come in two forms: globular and open clusters.

Globular clusters are dense collections of 10,000 to a few million stars. Globular clusters are usually very old, around 13 Gyr (for reference, the Universe is 13.7 Gyr old),

and have a large metallicity spread (~ 1.5 dex) between clusters. Globular clusters are distributed roughly symmetrically around the galactic center (or centers of other galaxies) and have highly eccentric orbits, usually at an angle from the galactic plane. The Milky Way has roughly 150 globular clusters (Harris 1996), while the nearby Andromeda Galaxy may have as many as 500 (Barmby & Huchra 2001).

Using globular clusters for evolutionary studies is problematic due to their very similar and advanced ages. Studies have also shown that the assumption of homogeneous populations to be false, with some of the most massive globular clusters showing multiple stellar populations (Piotto et al. 2007). It is possible that the explosions of first generation massive stars in the cluster caused another round of star formation. This second generation of stars will not only be younger than the first generation, but the “pollution” of the interstellar medium by supernovae remnants will cause the metallicity to change as well. These *multiple starburst* clusters are harder to study, as it cannot be assumed that the cluster can be modelled using a single age and metallicity.

Open clusters are loose collections of a few hundred to a few thousand stars all formed from the same interstellar gas cloud within the Galactic disk. In distinction to globulars, open clusters are found within the disk of the Galaxy and are usually significantly younger and more metal-rich. Open clusters are extremely important for galaxy evolution; a vast majority of stars (70-90%) are formed in open clusters (Lada & Lada 2003).

Star clusters are not infinitely-lived; they slowly “evaporate” and disappear over a few Gyr on average. When a cluster is far from all other large gravitational sources, the tidal radius of the cluster — within which stars are gravitationally bound — stays

fairly constant, r_{t0} . When the cluster passes by a large mass, such as a spiral arm or giant molecular cloud, the tidal radius shrinks to r_t as the outside mass pulls on the outer members of the cluster. Cluster stars that are now outside of r_t move away from the cluster under the influence of the foreign mass. After the cluster passes the outside mass, the tidal radius expands back to its original size, but some of the cluster stars have migrated such that they are now outside of r_{t0} and are therefore no longer bound to the cluster. These escaped stars then become integrated into the galactic field population.

Both globular and open clusters experience these effects, but globulars have much longer lifetimes than open clusters. Large clumps of mass are common within galactic disks, where most open clusters are located, and multiple of these “collisions” will remove many of the cluster members over a few Gyr. Understanding the evolutionary dynamics of open clusters, including their destruction, will inform how galactic stellar populations evolve.

1.1.7 Binary Star Systems

Binary star systems, or sometimes *binary stars*, are a system of two stars orbiting a common center of mass. The more massive star in the system is called the *primary* star while the smaller is called the *secondary*, or companion, star. Binaries are very important within a cluster environment due to the energy locked within their orbit, and will be described further in §8.

There are several classifications of binary systems, based on how a system is observed. An overview of each class is included below, along with an explanation of any relevant information that can be gained.

1.1.7.1 Visual Binaries

If a binary is close enough to Earth, and the separation between stars in the system is great enough, both stars in the system can be individually resolved by a telescope. The star Castor in the constellation Gemini is an example of this type of system, called a *visual binary*.

Observing the system through an appreciable portion of its period allows for a complete determination of each stars' orbital path. In addition to all of the orbital information on the system, the masses of each star can be determined for visual binaries. Getting magnitudes and colors from each star also allows determination of the temperature and spectral type of each member.

Visual binaries are extremely important to much of astronomical understanding due to the large number of system parameters that can be determined observationally.

1.1.7.2 Eclipsing Binaries

Similar to lunar and solar eclipses that are witnessed on Earth, a binary system can have eclipses when one of the stars passes in front of the other as seen from Earth. A diagram of an eclipsing binary system, along with a plot of observed brightness over time is shown in figure 1.3. For this example, the smaller star is assumed to be hotter: a main sequence star with a red giant companion.

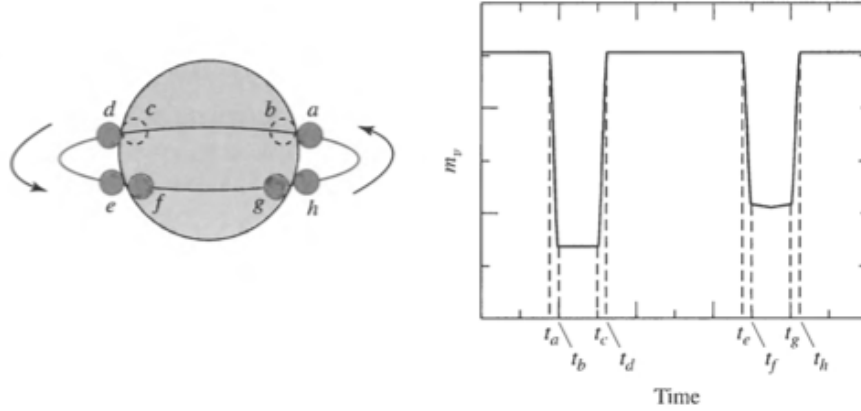


Figure 1.3: Light curve of an eclipsing binary system. Times denoted on the light curve correspond to the star positions on the left. Figure reproduced from Carroll & Ostlie (2006)

The first quantity that can be easily measured from an eclipsing binary is the ratio of temperatures of each star. At each point in the orbit, the flux from the system is measured (right panel of figure 1.3). When both stars are visible, the flux from the system is

$$B_0 = k (\pi r_L^2 F_L + \pi r_S^2 F_S) \quad (1.14)$$

Here, L corresponds to the larger star, and S to the smaller star. The parameter k is a multiplicative factor that accounts for the distance to the system as well as the filters and optics that are used for the measurement. When the smaller star is between positions b and c in figure 1.3, only the large star is visible, making the measured flux:

$$B_{bc} = k (\pi r_L^2 F_L) \quad (1.15)$$

The final configuration of the eclipsing system happens when the smaller star is between positions f and g. Then the total flux is:

$$B_{fg} = k [(\pi r_L^2 - \pi r_S^2) F_L + \pi r_S^2 F_S] \quad (1.16)$$

Combining these equations and utilizing the Stefan-Boltzmann equation $F = \sigma T^4$, we find:

$$\frac{B_0 - B_{bc}}{B_0 - B_{fg}} = \frac{F_S}{F_L} = \left(\frac{T_S}{T_L}\right)^4 \quad (1.17)$$

If the velocities of the stars in the system are known (which is possible using techniques described in §1.1.7.3), it is also possible to deduce the radii of the individual component stars in the system. Below, it is assumed that stars have a constant speed over the regions we are interested in, but these equations can be modified if there are appreciable changes in velocity as well. The radius of the each star is computed, where v is the relative velocity of the two stars:

$$r_S = \frac{v}{2} (t_b - t_a) \quad (1.18)$$

$$r_L = \frac{v}{2} (t_c - t_a) \quad (1.19)$$

Being able to determine temperatures and radii of stars allow for an easy determination of each stars' spectral type and evolutionary stage, which is helpful in understanding the internal mechanics of the binary system.

While the above two types of binary systems are important due to the wealth of information that can be gained, they are also quite rare. The linear resolution of a telescope falls off with distance, so any visual binaries detected must be fairly close to Earth. Binaries can also be formed in almost any orientation; their plane of orbit may be at any angle with respect to our line of sight, called *inclination*. Only for binaries with an inclination of almost 90° will Earth observers see eclipses, therefore eclipsing binaries are extremely rare. To study binaries in a wide range of environments, more than visual and eclipsing binary systems will be needed.

1.1.7.3 Spectroscopic Binaries

If a star is moving along the line of sight from Earth, its light is shifted due to the Doppler effect. Observed spectral lines will be blue- or red-shifted depending on the star's velocity. By comparing the observed spectral lines from a star to known wavelengths, the speed of the star can be determined, which is called a *radial velocity* (RV). Single stars will have roughly a constant radial velocity throughout a short period of time (hundreds of days), while many binary systems will show systematic shifts in RV as the stars orbit each other.

If both stars in the binary system are of comparable luminosity, spectral lines from both stars may be observed. These *double-lined binaries* allow for an estimation of the masses of both stars in the system as well as an understanding of the orbits of each star.

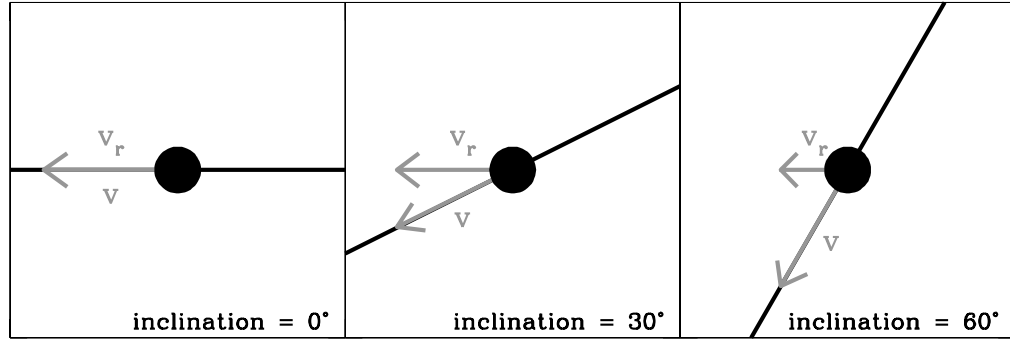


Figure 1.4: Difference between true velocity v and observed radial velocity v_r for various values of orbital inclination.

Using the velocity of each star, as well as the orbital period, the semi-major axis of the system can be calculated.

$$a = a_1 + a_2 = \frac{P}{2\pi v_1} + \frac{P}{2\pi v_2} \quad (1.20)$$

Plugging this into Kepler's 3rd law and solving for the mass of the individual stars gives,

$$m_1 + m_2 = \frac{P}{2\pi G} (v_1 + v_2)^3 \quad (1.21)$$

Radial velocities from spectroscopic binaries are complicated due to the inclination angle, i , of the system. If the orbit of the system is angled with respect to the line of sight from Earth, the radial velocity measured will be less than the orbital velocity of the system by a factor of $\sin i$, where i is the inclination of the system (illustrated in figure

1.4). Adding this to equation (1.21),

$$m_1 + m_2 = \frac{P}{2\pi G} \frac{(v_{1r} + v_{2r})^3}{\sin^3 i} \quad (1.22)$$

Here v_{1r} and v_{2r} are the actual radial velocities measured by astronomers. This equation gives lower bounds on the possible masses of the stars in the system, but cannot exactly determine them due to the uncertain inclination.

Regardless of the inclination, the center of mass of the binary system remains at a constant velocity, so the ratio of masses in the system is easily determined:

$$m_1 v_1 = m_2 v_2 \quad (1.23)$$

$$\frac{m_1}{m_2} = \frac{v_2}{v_1} = \frac{v_{2r} \sin i}{v_{1r} \sin i} = \frac{v_{2r}}{v_{1r}} \quad (1.24)$$

This relation works on both the “true” orbital velocities of the stars, as well as the observed velocities, v_{1r} and v_{2r} .

Often, the secondary star is too dim to be observed in the spectra, but some information can still be gained from these *single-lined binaries*. Plugging (1.24) into (1.22) yields,

$$\frac{m_2^3}{(m_1 + m_2)^2} \sin^3 i = \frac{P}{2\pi G} v_{1r}^3 \quad (1.25)$$

The right hand side of equation (1.25) is called the *mass function*, and only depends on observable quantities: the period and primary star radial velocity. Although the individual masses of the stars cannot be determined with only one star’s velocity information,

it does give a lower bound for m_2 since the left hand side of equation (1.25) is always less than m_2 .

Due to the fact that no detailed masses can be determined from single-lined binaries, they are only useful for statistical studies and not for determining the detailed mechanics of the system itself.

The above classifications are not mutually exclusive: A spectroscopic binary may have an inclination of 90° and therefore also experience eclipses. Such a system is called an *eclipsing spectroscopic binary*. These systems are powerful tools, as the inclination is removed from (1.22) and (1.25). Double-lined eclipsing spectroscopic binaries allow for the determination of the masses of both stars as well as the period and eccentricity of each star's orbit.

Chapter 2

Science Questions

This work will attempt to answer three fundamental questions about binary populations in open clusters:

1. *How is the binary population affected by cluster parameters?*

Star clusters form when some outside force (other cluster passing through the Galactic disk, supernova, etc.) shocks a large cloud of gas. Small perturbations in density within the cloud form into single and binary cluster stars. How the distribution of pre-binary density perturbations change with metallicity and overall cluster mass has not been well studied, nor has how the binary fraction of a cluster changes with time. Using a large sample of clusters, trends between binary fraction and intrinsic cluster parameters can be understood.

2. *How do binaries affect the dynamical evolution of a cluster?*

Open clusters are slowly destroyed over time, with external effects being described in §1.1.6. In addition to the external tidal effects, stars can be ejected from the

cluster due to gravitational interaction with other member stars. When a less-massive star gravitationally interacts with a more massive one, it may pick up enough energy to be accelerated beyond the escape velocity of the cluster. Binary systems may amplify this process by contributing part of their orbital energy to interactions, which is usually greater than the kinetic energy of the system moving through the cluster.

Due to the vast timescale over which clusters evolve, stellar ejection cannot be studied observationally. Cluster ejection is usually studied via detailed N-Body simulations (Hurley et al. 2001; 2005), which can give a detailed description of what stars were ejected, when they were ejected, and how fast they were moving at the time of ejection. Each of these parameters dictate how the field population of the galaxy may have been built up by open cluster dissolution.

N-Body body simulations have already been run to analyze the binary population's effect on escaping stars, discovering only a slight difference when varying the cluster binary percentage from 0 to 70% (Moyano Loyola & Hurley 2013). These studies have made assumptions about the primordial binary population, however, such as an even mass-ratio (ratio of larger to smaller star mass) distribution, which may not be the case in reality.

Measuring the cluster binary fraction and mass-ratio distribution (as a function of primary mass) for real clusters will go a long way in calibrating these N-Body simulations. Analyzing open clusters with various ages will also allow N-Body sim-

ulations to check intermediate steps against these “benchmarks,” further improving their accuracy and predicting power.

3. *How does the cluster environment affect the dynamical evolution of its binary population?*

A primordial open cluster contains a uniform distribution of stellar masses, when scaled by density. Although the core is more dense than the outer regions of the cluster, there is no physical mechanism that would cause a different distribution of density perturbations in each region. This means that, when the cluster is newly formed, there are the same *percentage* of $4 M_{\odot}$ stars in a given area of the cluster as there are $1 M_{\odot}$ stars.

More massive stars preferentially transfer energy to smaller stars via gravitational interactions such that, over time, the cluster approaches an equipartition of energy. When kinetic energy is a constant, the maximum velocity of a star during its path through the cluster, and hence the furthest distance it can travel, scales inversely with mass. This means that, over time, more massive stars become more centrally concentrated than less massive ones. This phenomenon is called *mass segregation*, and is seen observationally in many open clusters.

Because binary systems are more massive than a comparable single star, they too experience mass segregation. Initially, the binary fraction is constant with radius, just as with single stars. Over time, binaries become more centrally concentrated, leading to higher binary fractions near the core of the cluster and lower binary

fractions towards the outskirts. This has also been seen observationally in many old open clusters (Mathieu & Latham 1986, Geller & Mathieu 2012).

Most recently, there were two binary studies of the young, dense cluster NGC 1818, located in the Large Magellanic Cloud. The first study, published in Elson et al. (1998), confirmed what had been seen many times before: a decreasing binary percentage with radius, indicative of mass segregation. Even with the relative youth of NGC 1818 (30 Myr), Elson et al. found binary systems have undergone enough dynamical evolution to become segregated. A follow-up study in de Grijs et al. (2013) found a completely different, and somewhat remarkable, result: not only were binary systems not mass segregated, but binary fraction actually *increased* with radius.

Using open clusters with a variety of ages, from 30 Myr to 3.5 Gyr, the radial migration of the binary population can be tracked through time. Using these data, the conflicting NGC 1818 studies can be understood and reconciled.

Chapter 3

BINOCES

3.1 Current Binary Detection Techniques

Current cluster binary studies are carried out using one of two methods, each of which experience issues which limit their effectiveness in answering the above science questions.

The strengths and limitations of the two current methods are described below.

3.1.1 Two-Band Photometry

Binary stars will be brighter than a single star with the same mass as the primary, due to additional flux from the secondary star. In addition, the star's color will be shifted by the smaller (and hence redder) star. When plotted on a CMD, main sequence binaries will be offset above and to the right from the single star main sequence. Considering the special case of an equal-mass binary system, the binary will have the same color as a component single star, but will be twice as bright. Using equation (1.2), we find the difference in magnitudes:

$$m_{\text{Single}} - m_{\text{Binary}} = -2.5 \log_{10} \left(\frac{F_{\text{Single}}}{F_{\text{Binary}}} \right) = -2.5 \log_{10} \left(\frac{F_{\text{Single}}}{2F_{\text{Single}}} \right) = 0.753 \quad (3.1)$$

An equal-mass binary system will be located 0.753 magnitudes above the corresponding single star on a CMD. Binaries with a mass ratio less than one will be located at various locations between the single star main sequence and the equal mass binary sequence on the CMD. Two-band photometry studies attempt to measure the binary properties of a cluster using a single CMD by measuring the distance between a star and the single star main sequence.

The distance a binary star is from the single star main sequence depends not only on the mass ratio of the system, but also the primary mass. Figure 3.1 shows the position of binary stars on a CMD for various primary masses and mass ratios. Binaries with a mass ratio of 0.5 (open squares) lie close to the single star main sequence for primary stars with mass $< 2M_{\odot}$ and close to the equal mass binary sequence for primary masses of $> 3M_{\odot}$.

This binary detection technique is very sensitive to uncertainties. For low mass primaries, small color errors will blend together single stars and binaries with a mass ratio of < 0.5 . On the high mass end, it becomes hard to differentiate between primary masses, as all binaries with mass ratios > 0.5 lie along the equal mass binary track. Figure 3.1 shows binary positions for high primary masses in a grid of $1 M_{\odot}$. Attempting to measure using a finer grid is impossible, as many binaries will begin to overlap.

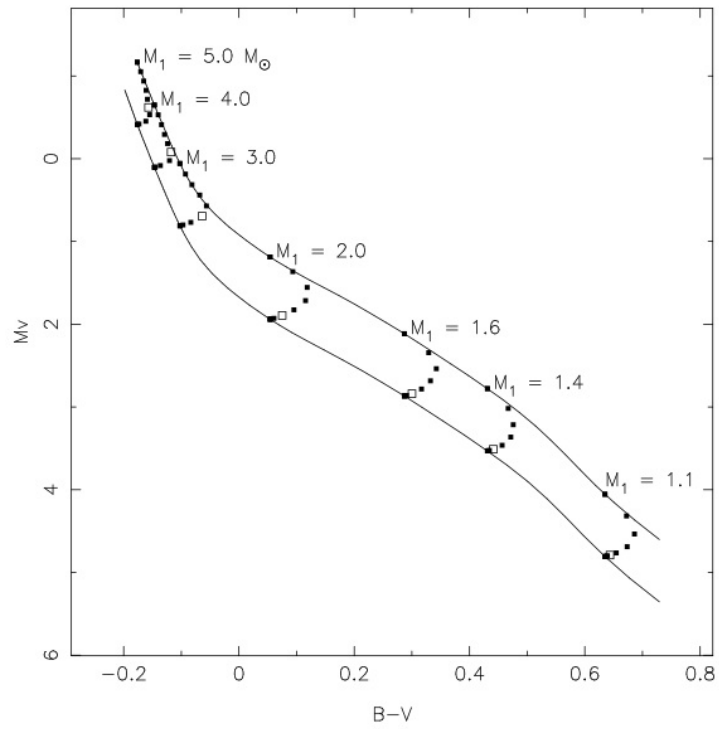


Figure 3.1: Figure reproduced from Hurley & Tout (1998). Theoretical single star and equal mass binary main sequences for a star cluster covering a range of magnitudes. For each primary mass, points are plotted on the CMD for every binary mass fraction in steps of 0.1. Open squares are binaries with a mass ratio of 0.5.

Two-band photometry studies are most useful for quickly determining the binary fraction of a cluster; it only requires measurements in two filters. While it is impossible to accurately determine individual masses of binary systems, binaries with mass ratios greater than 0.5 can be grouped together and measured (see Milone et al. 2012). Determining the individual mechanics of the binary systems within a cluster, necessary for the science drivers of this research, requires a more robust approach.

3.1.2 Radial Velocity Studies

The most accurate way of detecting binaries is through the use of radial velocities of spectroscopic binaries (described in §1.1.7.3). The value of these studies is the wealth of information on star orbits that can be determined (orbital period, eccentricity). RV studies of cluster binaries, while powerful due to the amount of information they give, are limited in several ways.

Sample Size: Since RVs are determined spectroscopically, there are only a small number of stars that can be measured at a single time. Photometry (imaging) of a cluster can determine magnitudes for thousands of stars with a single image, while spectroscopy, at maximum, can measure spectra for a few hundred stars at once. In order to survey a cluster, a large amount of telescope time must be used to cover all stars.

Multiple Visits: Stellar spectra must be obtained at least 3 times in order to determine whether a star displays shifting velocities. Fully characterizing the orbits of both stars

requires many repeat observations, depending on the orbital period of the system. This multiplies the necessary telescope time for a quality RV study in order to detect and classify binaries.

Limiting Magnitude: In order to accurately determine a star’s velocity, a certain level of signal-to-noise must be achieved. For a high-resolution spectrometer ($R \sim 20,000$), the incoming flux is spread across all resolution elements. Comparing to a comparable length photometric exposure, we find the limiting magnitude difference:

$$m_{\text{phot}} - m_{\text{spec}} = -2.5 \log_{10} \left(\frac{1}{20000} \right) = 10.8 \quad (3.2)$$

In the time it will take a spectroscopic measurement to complete on a 10th magnitude star, all stars down to 20th magnitude could be measured photometrically to the same signal-to-noise. Low-mass stars are more numerous than high-mass stars, and therefore very important when understanding the dynamics of the cluster system. Ignoring a vast majority of the low-mass members within a cluster will severely hamper the power of the results.

Inclination & Orbital Period: Mass determination using double-lined binaries is complicated by the inclination of the system. While RV studies can determine the orbital mechanics of the system, they cannot accurately determine masses for all binaries. Without accurate masses for a large percentage of binary systems within the cluster, our science goals cannot be achieved. In addition, RV studies are limited by the resolution of

their spectrometer; systems with doppler shifts less than the resolution of the spectrometer will not be registered as variable. Only binary systems with short enough orbital periods will produce large enough doppler shifts to be detected.

Both of the current binary detection methods are inadequate to answer the science questions posed in §2. To deeply understand the binary populations of open clusters, and new method must be employed which can determine accurate masses for all members of a cluster within a reasonable amount of telescope time.

This new binary detection method is presented below, nicknamed BINOCS: BINARY INFORMATION FROM OPEN CLUSTERS USING SEDS. The BINOCS moniker will be used in reference to several different concepts throughout this paper:

- This project and body of work as a whole
- The method of binary detection to be described below
- The computational code which implements this method

3.2 The BINOCS Method

As a first approximation, stars are blackbodies, with characteristic energy distribution curves determined solely by their temperature. By imaging a star using multiple filters (which only allow a specific range of wavelengths) across the spectrum, one should be able to “re-build” this blackbody curve. By comparing the rebuilt curve to blackbodies of

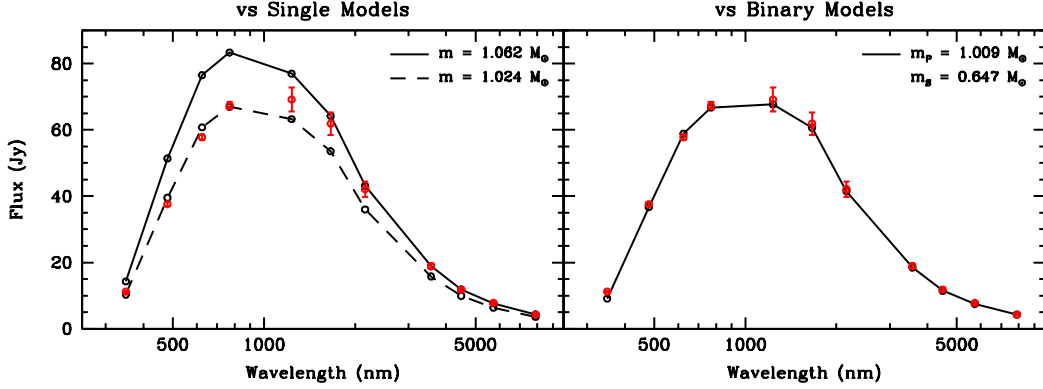


Figure 3.2: Comparison of star in open cluster M67 with model SEDs. Observed data in 11 filters shown in red. (Left) Observed SED compared to two best-fit single models. (Right) Observed SED compared to best-fit binary model.

different temperatures, one would be able to determine the temperature of the observed star. Similarly, a binary system could not be accurately modelled by a single blackbody curve, but instead by two blackbodies added together. In this theoretical scenario, if a star did not fit any single blackbody curve, but fit a combination of two curves, it would be classified as a binary system with component stars having the associated temperatures.

In practice, stars are not blackbodies, but the main premise stays the same. Stellar structure models exist which predict the *spectral energy distribution* (SED) of a star given its parameters: age, metallicity, mass. The star is a member of a cluster with known parameters, so age and metallicity are given. By matching stars to these models, mass can be determined, similar to how temperature could be determined in the idealized blackbody case. If a star does not fit any of the single-star SEDs, it is determined to be a binary system, and is compared to combinations of SEDs.

An example of this method is shown in figure 3.2. A star within the open cluster M67 (NGC 2682) was imaged in 11 filters, $ugriJHK_S[3.6][4.5][5.8][8.0]$, and an observed SED

was created. This observed SED was compared to all available single-star models for the cluster, producing two close-fitting models. As seen in the left panel of figure 3.2, the $1.024 M_{\odot}$ model fits the optical region of the observed SED, but diverges for the IR. The $1.062 M_{\odot}$ model fits much more accurately in the mid-IR, but overestimates the flux in the optical. There are no single-star model SEDs which approximate what was observed, but when compared to binary SED models, the data is fit much more closely. This star was classified as a single star in a previous RV study of M67 (Mathieu et al. 1997), but from this comparison of the SED, it is most likely a binary system.

3.3 The BINOCS Code

Star clusters often contain thousands of stars, which need to be compared to tens of thousands of SED models. These comparisons cannot be done by hand; a computational code is necessary. The BINOCS code used in this work is publicly available from GitHub¹ as a Python module.

The BINOCS code first creates a library of synthetic binary SEDs. Using a stellar structure model called an *isochrone*, the code reads in all single-star model SEDs: magnitude measurements in all 17 possible bands ($UBVRIugrizJHK_S[3.6][4.5][5.8][8.0]$) for stars with varying masses in the cluster. The isochrone magnitudes are shifted to the distance of the cluster being observed, using (1.8), and adjusted for extinction.

Isochrones often come in coarse mass grids, however, hampering the code’s ability to accurately determine masses. To overcome this, stellar parameters and magnitude are

¹<http://github.com/bathomps0/binocs>

cubically interpolated with respect to mass onto a new mass grid. For most clusters, a grid spacing of $0.01 M_{\odot}$ is used. Using these newly-interpolated single-star models, the BINOCS code creates binary models by combining filter fluxes from the component primary and secondary models:

$$V_{binary} = -2.5 \log_{10} (F_{V,primary} + F_{V,secondary}) \quad (3.3)$$

$$V_{binary} = -2.5 \log_{10} (10^{-V_{primary}/2.5} + 10^{-V_{secondary}/2.5}) \quad (3.4)$$

Using (3.4) for each of the 17 filters, binary SEDs can be created for every possible configuration.

Next, each observed star is compared to every binary SED model using:

$$\Phi = \sum_{\text{filters}} \frac{1}{m_{\text{star}} - m_{\text{model}} + 0.01} \quad (3.5)$$

If any of the elements of the sum is < 7 , meaning that the difference in magnitudes is > 0.13 (well above the usual observational uncertainty), then the filter is considered “distant” and not included in computing Φ . To ensure a quality comparison, a model must have three of five “close” optical filters (from *UBVRI* or *ugriz*), all three near-IR filters considered “close”, and two of four mid-IR filters marked “close.” After removing those models without enough close filters, all Φ values are divided by the number of filters used in the sum. This ensures that a worse-fitting model will not be chosen over a better-fitting one simply because it may be marked “close” for more filters. The model

with the highest Φ per filter is chosen as the best-fit model, and recorded. If no models have enough close filters, the star is marked as a *non-member*.

After comparing each star to the full model library, it is compared to only single models, using a much less stringent close filter cut — each sum element must be > 1 . The purpose of this comparison is two-fold: first is to be able to compare best-fitting single and binary models for illustrative purposes, as shown in figure 3.2. Secondly, some stars, while classified as binaries through the BINOCS method, are better classified as singles due to other considerations (these cuts will be explained in §6.4). If a star is forced to be classified as single, the parameters from this stage of fitting will be used to estimate its parameters.

When taking an image of a cluster, stars that are not part of the cluster will also be included: star within the field of view of the telescope but not within the bounds of the cluster, or stars in front of or behind the cluster. These stars contaminate a plotted CMD: bright stars that are at a further distance than the cluster may intersect with the cluster’s main sequence. Because open clusters are formed in the disk of the Milky Way, where there are many field stars, this contamination can be significant. Two-band detection cannot disentangle these contaminants, throwing off some measurements using the technique. Using a wide wavelength range, and a minimum of 8 filters, allowed the BINOCS code to disentangle some of these problem stars. Although a star may lie on the main sequence in an optical CMD, it may lie far off of it in the IR. By eliminating stars without the necessary “close” magnitudes, much of the contamination which plagues two-band methods can be removed.

Using a Monte Carlo method, observational uncertainties are accounted for by randomly varying the input magnitudes using a Gaussian distribution where $\sigma =$ the magnitude’s associated uncertainty. The BINOCs fitting is run 200 times, and a best-fit model is recorded for each iteration. If the majority of fits of a star classify it as a non-member, then it is deemed a non-member overall. For member stars, best-fit primary and secondary masses are determined to be the median of all best-fit models.

By relying on, at minimum, 8 filters, individual observational uncertainties become much less important than in the two-band method. The degeneracies that plague that method are severely reduced, allowing accurate mass determinations over nearly the entire mass range available in the cluster. Additionally, because imaging data is relied upon instead of spectroscopy, limited telescope time is needed. Assuming access to the right instruments, all necessary data can be obtained in a few nights, making this approach highly efficient.

§4 will give an overview of the instruments used to collect the data necessary for the BINOCs routine, the sample of clusters to be used in answering the science questions, and what data is available for each cluster. §5 will explore the stellar structure models used to create the comparison SEDs, as the mass results from the BINOCs code are only as accurate as the underlying models themselves. §6 will test some of the assumptions made in the description of the BINOCs code above (number of “close” filters, number of iterations), as well as compare the results of the SED fitting to that of previously-published RV studies. §7 and §8 will use the BINOCs results to answer the science questions posed in §2.

Chapter 4

Data Overview

4.1 Instrumentation and Processing

4.1.1 Visual Wavelength Detectors

Astronomy was ushered into a new era in 1979 when the first charge-coupled device (CCD) detector was installed on the 1-meter telescope at Kitt Peak National Observatory. Before this, photographic plates had been the standard, but the new CCD cameras were much more efficient, allowing the detection of fainter objects than even the best photographic plates.

A CCD detector is an array of individual CCDs that make up the pixels of the camera. CCDs use a layer of silicon as the main optical element, so when a photon strikes the silicon, an electron is excited to the conduction band and transferred to a “gate” where the charge is stored. When an image is ready to be read out, the first row in the array dumps its charge into a charge amplifier, converts that charge to a voltage, and stores that

voltage as a numerical value for that pixel. Once the first row is completely converted, an electric field is applied to transfer the charge from the second row into the first, where it is then read out. This process continues until all rows of the chip have been counted.

Silicon has a band gap height of roughly 1.0 eV, depending on temperature. This corresponds to a photon with a wavelength of 1240 nm, around the location of the J filter. Photons with wavelengths greater than this (most of the infrared range) will not be able to excite an electron to the conduction band, and therefore different types of detectors must be used for infrared filters.

4.1.2 Infrared Wavelength Detectors

IR detectors function similarly to CCDs. A semiconductor is struck by a photon, exciting it to the conduction band and transferring the charge. Instead of storing the charge in a gate and reading out all pixels at the end of an exposure, each pixel of a IR detector has its own readout amplifier. As charge accumulates, the amplifier keeps track of the accumulated voltage, and results can be accessed and stored when required. Reads of the chip are *non-destructive*, meaning that the accumulated charge is not altered by measuring a pixel's value, much different than for a CCD. IR detectors allow for reading out only parts of a chip, or reading out a chip multiple times throughout an exposure.

There are several different types of semiconductors used in IR detectors. Mercury cadmium telluride (HgCdTe) detectors have a band gap of 0.5 eV, corresponding to a limiting photon wavelength of 2500 nm, making them ideal for near-IR studies. Another choice is indium antimonide (InSb) which has a band gap of 0.25 eV (5000 nm), allowing

for use in the near- and part of mid-IR range. For further mid-IR filters, silicon arsenide (SiAs) detectors are ideal due to their very small band gap of 48 meV ($25 \mu\text{m}$).

4.1.3 Image Reduction

To prepare a science image for analysis, the following corrections must first be made to account for a variety of instrumental effects. As CCDs and IR detectors function differently, each correction will be labelled with the type(s) of detectors it needs to be applied to.

Bias Correction [CCD]: To transfer charge between rows in a CCD, an electric field is applied. The energy stored in this electric field may cause extra electrons to be excited as the charge migrates across the chip. These extra electrons are not part of the signal, and must be corrected out. To remove them, the chip is read out multiple times in succession without exposing. These “0 second” bias images will show no counts besides those from the charge transfer process. Bias frame counts are subtracted from all images.

Dark Current [CCD, IR]: The detector is usually cooled to liquid nitrogen temperatures, but this still leaves some thermal energy that can excite an electron within the detector to the conduction band. Additionally, there may be defects on the chip that cause some pixels to register large counts regardless of where they are pointed, called *hot pixels*.

To correct for this, an image is taken with the shutter closed, ideally of the same exposure length as the science images. Because no light from the sky hits the chip, all the detected counts are from the electronics themselves. Averaging several of these *dark frames*, after subtracting bias counts, will determine the average thermal excitation counts for each pixel as well as other electronic defects. Dark frames are subtracted from all images.

Flat Fielding [CCD, IR]: When a photon strikes a pixel of the detector, an electron will not always be excited and recorded for that pixel. The percent chance that an incoming photon will register a count with the detector is called the *quantum efficiency*. The quantum efficiency of a CCD detector is usually above 90%, but it is not always the same for each pixel. In addition, the filter being used may not be manufactured perfectly or there may be dust grains lying on the various surfaces of the telescope. Imperfections of the filter may cause light to be refracted in unintended ways, limiting the effectiveness of certain pixels on the chip. This effect is lumped into each pixels' overall efficiency.

Correcting for this effect can be accomplished in two ways. First, the telescope can be pointed at a flat surface that is uniformly lit by a lamp, or multiple lamps. The resulting image, called a *flat field*, should have identical counts for all pixels, but due to the non-uniform efficiency, some pixels will register fewer counts.

The lamps used for flat-fielding have a specific temperature, so the flux through some filters may not be very high (for example, *U* and *B* filters). Instead of using the lamps, the telescope is pointed at several different points in the sky and images are taken. If the images are taken high enough in the sky, away from high light pollution areas near the

horizon, the photon counts from the sky should be roughly constant. Combining these multiple images using a median will create a *sky flat*, removing any stars in the frames and leaving only a sky background. Similar to the flat field image, this sky flat should be uniform, but some pixels will register fewer counts due to lowered efficiency.

Once the flat image is taken (be it a flat field or sky flat), the bias and dark frame are subtracted (to remove electronic effects), and it is then normalized. In the normalized image, each pixel's value represents its efficiency. The science image counts are divided by the normalized flat field to bring all pixels to the same effective level. Analogous to dark frames, which correct for effects from the electronics, flat fielding corrects for effects within the optical elements of the system.

4.1.4 Magnitude Measurements

Measuring star brightnesses, and thus magnitudes, from images is accomplished through a process called *photometry*. There are two different approaches to photometry, described below.

Aperture Photometry: This technique uses three circles, called apertures, to determine the number of photons from a star. The setup of the three apertures for a fictional star is shown in figure 4.1. The innermost circle, called the *image circle*, is centered on the star and has a radius such that it encloses the entire image of the star. The number of photon counts within this circle come from two effects: photons coming from the star itself, as well as scattered photons from the sky background. To remove these sky

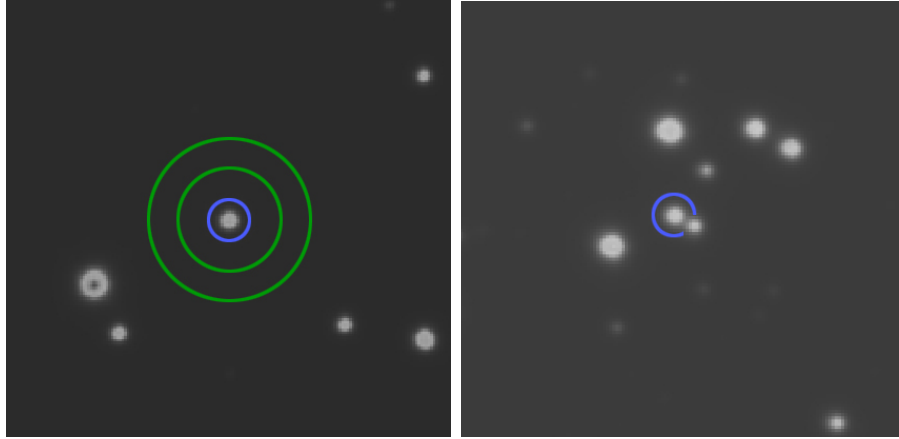


Figure 4.1: *Left:* Aperture photometry set-up for observed star in the cluster M67. Blue circle is the image circle, green circles are edges of sky annulus. *Right:* Failure of aperture photometry in the dense cluster M37. No reasonable image circle can be drawn without being contaminated by nearby star.

photons, the next two circles are used to form a ring, called the *sky annulus*. The counts within the sky annulus are assumed to all come from the sky background, because there are no stars enclosed, and is used to determine the average number of sky photons per pixel in the image. Using this information, sky photon counts can be removed from the image circle, leaving only a count of photons from the star.

The benefit of this technique is that it is simple to do, and fast to compute. The only input parameters are the three circle radii, and a computer can determine magnitudes for thousands of stars very quickly. This technique breaks down, however, when stars are too close together for any sky annulus to accurately determine sky photon counts, or if the field is so dense that stars begin to overlap, as seen in the right-hand panel of figure 4.1. For sparse fields, aperture photometry is the most efficient way to determine magnitudes.

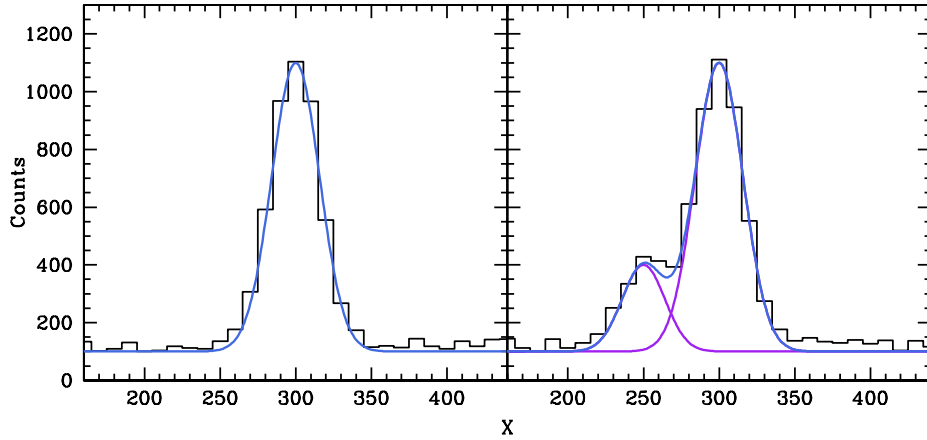


Figure 4.2: Brightness profiles along a single row of a chip. *Left:* Gaussian fitting to a single star, sky background of ~ 100 counts. *Right:* Gaussian fitting of two overlapping stars, sky background of ~ 100 counts. Blue curve is sum of both purple individual star gaussian fits.

PSF Photometry: Diffraction due to light passing through the aperture of the telescope produces a pattern called an *Airy disk*. Point-source function (PSF) photometry measures the magnitude of a star by fitting a mathematical function (Gaussian / Lorentzian) to the Airy disk, then integrating over it to find the total photon counts. Figure 4.2 shows an example of a PSF fitting. In both cases, the sky background is roughly 100 counts, setting the baseline of the gaussian fit function. The power of PSF photometry is shown in the right hand panel of figure 4.2, where two stars in the frame partially overlap. Aperture photometry can not handle crowded fields, but PSF fittings are able to separate partially overlapping brightness profiles, allowing accurate magnitudes in dense environments. This approach is especially useful for clusters, where the density of stars is higher than in the field.

PSF photometry involves first selecting a number of “template” stars, with which to calculate the mathematical form of the PSF. Using these templates, the parameters of

the PSF, as well as how they may vary with position, are determined via a χ^2 minimization. The PSF photometry in this project was completed using the DAOPHOT suite of programs: DAOPHOT II and ALLSTAR (Stetson 1987). DAOPHOT allows variation of PSF parameters linearly or quadratically across the chip, as well as the option to use a gaussian, lorentzian, or sum of both as the shape for the PSF. In most cases, around 3% of the total detected sources are initially used as template stars for the PSF. This list of template stars was then pruned to remove stars which degraded the fit.

First, stars near bad or saturated pixels were removed, so as not to alter the PSF fit with these outliers. Next, stars that were less than 4 full-widths at half-maximum (FWHM; a measure of the width of the PSF) from another source were removed. While PSF photometry can handle overlaps, template stars are assumed to be individual sources. Lastly, stars whose PSF χ^2 fit values were 2σ or more above the mean were removed, as they clearly did not fit the general profile of the other candidate template stars.

PSF parameters are determined by fitting a PSF profile to the pruned list of template stars. After the PSF parameters are determined, it is applied to all sources in the image, with only the amplitude being varied. Integrating over the PSF gives the flux, and thus the magnitude, of each star in the image.

4.2 Cluster Sample

In total, 16 clusters were targeted for use in this work. The distribution of cluster parameters for our targeted sample is shown in table 4.1, and visually in figure 4.3.

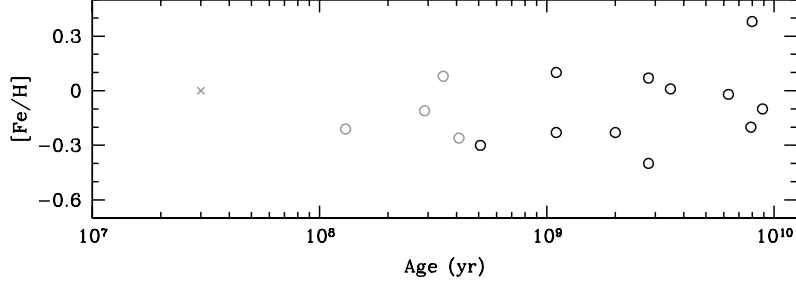


Figure 4.3: Distribution of 16 targeted clusters in age and $[\text{Fe}/\text{H}]$ (Dias et al. 2002). X's represent clusters which do not have any published metallicity information. Points in grey correspond to clusters with ages < 500 Myr, usable for primordial binary studies.

Cluster	Age (Gyr)	$[\text{Fe}/\text{H}]$	Distance (pc)	$E(\text{B}-\text{V})$
NGC 1960 (M36)	0.03	...	1320	0.22
NGC 2168 (M35)	0.13	-0.21	870	0.20
NGC 1912 (M38)	0.29	-0.11	1070	0.25
NGC 2099 (M37)	0.35	+0.08	1390	0.30
NGC 1817	0.41	-0.26	1980	0.33
NGC 1039 (M34)	0.51	-0.30	500	0.07
NGC 2158	1.10	-0.23	5080	0.36
IC 4651	1.10	+0.10	1050	0.00
NGC 2420	2.00	-0.23	2500	0.03
NGC 6819	2.80	+0.07	2400	0.13
Melotte 66	2.80	-0.40	5250	0.00
NGC 2682 (M67)	3.50	+0.01	860	0.04
NGC 188	6.30	-0.02	1820	0.06
Berkeley 39	7.90	-0.20	5750	0.00
NGC 6791	8.00	+0.38	4170	0.15
Collinder 261	8.90	-0.02	3160	0.00

Table 4.1: Cluster parameters for all clusters in dataset (Dias et al. 2002).

The cluster sample covers a large area of the parameter space: ages range from 25 Myr to 9 Gyr while $[\text{Fe}/\text{H}]$ varies from -0.38 to $+0.32$ — 40% to 200% the Iron content of the Sun. Exploiting this parameter range is critical in answering the posed science questions. In reference to science question 1, there are five clusters with ages < 500 Myr. Using BINOCS results from these five clusters, an understanding of the primordial cluster binary population can be conceived.

4.3 Available Data

Data that will be used in this project were compiled from a number of sources.

4.3.1 Optical Data Sources [0.3 – 1.0 μm]

Sloan Digital Sky Survey (SDSS): Beginning operations in 2000, the SDSS Legacy Survey aimed to provide uniform and well-calibrated photometry for much of the northern sky. Observations were taken using the Sloan 2.5m telescope at Apache Point Observatory (APO) (Gunn et al. 2006). To efficiently cover large contiguous areas of sky, SDSS observations were taken using a technique called *drift scanning*. In drift scanning, the telescope is kept stationary as the stars move horizontally across the chip over time. The CCD chip is read out at exactly the same speed as the stars move across a single pixel, allowing for the electrons from a star to track with it. While a star may only be located on a single pixel for less than a second, the final image will have an integrated exposure length of almost a minute.

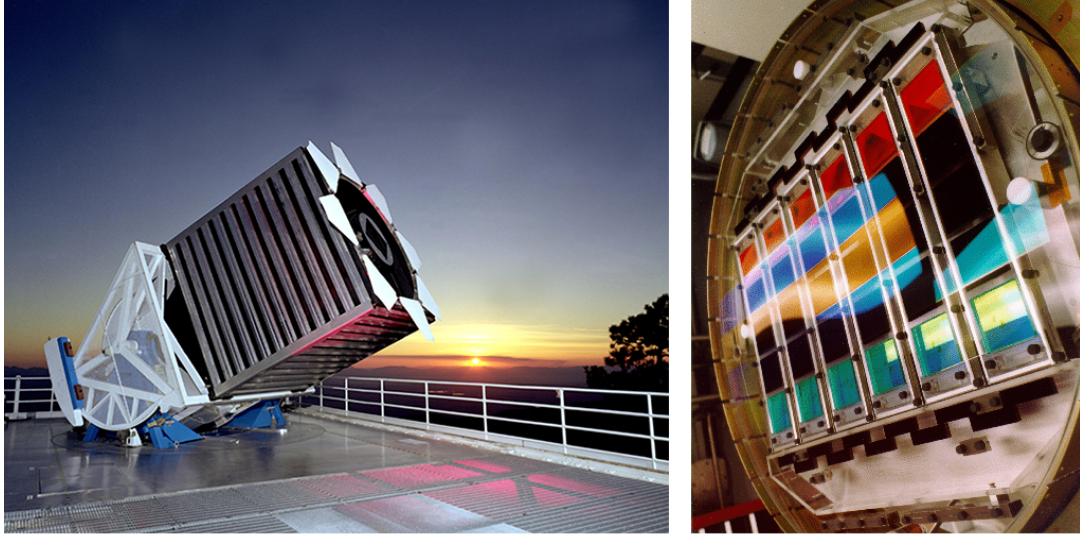


Figure 4.4: *Left:* SDSS 2.5m telescope at APO.¹ *Right:* SDSS Legacy Survey camera.²

SDSS imaged the sky using five different filters, *ugriz*, and to do so built one of the most complex cameras in all of astronomy, shown in figure 4.4. Each column of the camera contains 5 CCD chips, each with a different SDSS filter above it. A star would move across the column of chips (top to bottom in the figure), being imaged through each of the five filters in quick succession. To cover large areas of sky at a time, the camera contained six of these filter columns.

From 2000 to 2008, the SDSS Legacy Survey imaged more than 8200 square degrees of sky, covering several of the clusters in this project (Abazajian et al. 2009). Magnitudes released from SDSS were measured using aperture photometry; such a large area of sky required the least computationally costly approach. Most of the region imaged by the Legacy Survey was in the low density halo of the Milky Way, where aperture photometry works accurately.

¹<http://astro.uchicago.edu/~frieman/SDSS-telescope-photos/sdss-telescope.jpg>

²<http://www.sdss.org/dr3/instruments/imager/faceplat.gif>

Magnitudes for stars in the densely packed globular and open clusters in the imaged region were unable to be measured accurately by the aperture photometry technique. An et al. (2009) re-derived magnitudes for several globular and open clusters within the Legacy Survey region using PSF photometry. The open clusters NGC 2682 (M67), NGC 2420 and NGC 6791 were included in this imaged area, with PSF magnitudes measured down to $g \sim 23$.

MOSAIC: The MOSAIC instrument (Sawyer et al. 2010), outfitted with *UBVRI* filters, contains an array of eight 2048-by-4096 pixel CCD chips to create a single 8192-by-8192 pixel image. While it has been attached previously to the 4-m telescope at Kitt Peak National Observatory (KPNO), the data used in this project is from the WIYN 0.9-m telescope at KPNO. With roughly a square degree field of view, the MOSAIC images will allow us to analyze the entire spatial extent of any cluster observed.

Images of several open clusters were obtained with MOSAIC over several nights in Feb 2000 (Sarajedini & Kinemuchi, *private communication*). *UBVI* photometry was obtained on five clusters in the same set: M35, M36, M37, M38, M67. For all clusters, both short and long sequences of images were taken. Short images had exposure lengths of 25s, 8s, 5s, 5s in *UBVI*, respectively. Four images of the same exposure length were taken in each filter. Long sequence images, also four per filter, had 10 times the exposure length of the short set: 250s, 80s, 50s, 50s. Using both sequences together allows for photometry of the brightest and faintest stars within the cluster.

Three of the clusters have already been analyzed: M35 in Thompson et al. (2014), and M36 and M38 at TCU. For the TCU analysis, the four images in each filter were combined

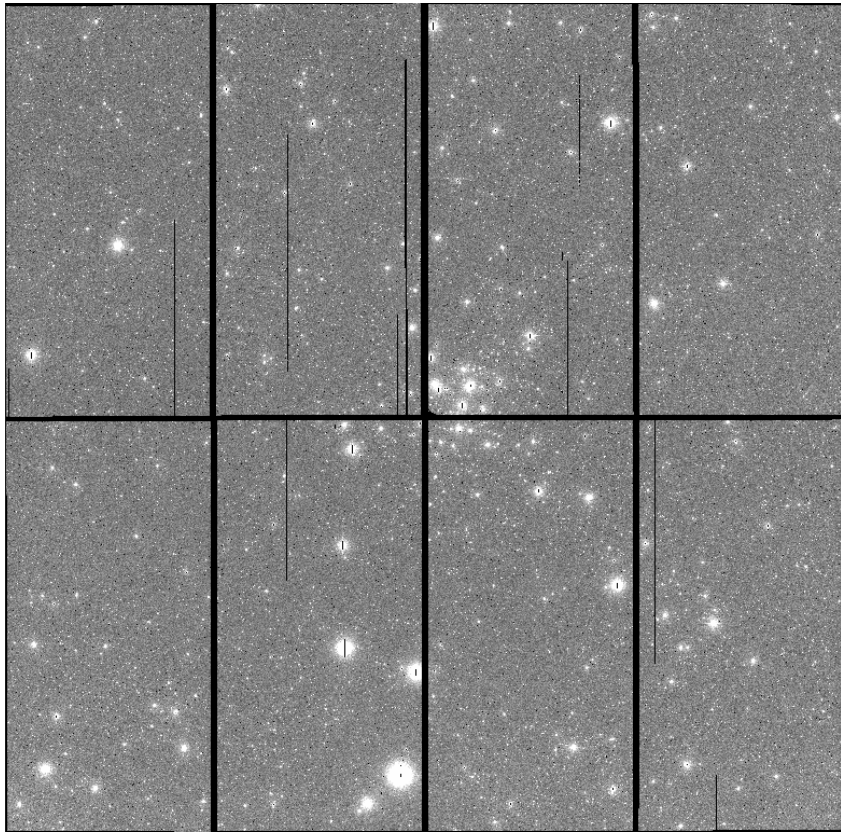


Figure 4.5: Reduced MOSAIC 50s *I*-band image for M36.

to form a higher signal-to-noise master image, and to provide a complete covering of the cluster. Note the wide gap between chips in the individual MOSAIC images, shown in figure 4.5. Each of the four images per filter were *dithered* (slightly offset) such that the combined image had no gaps in coverage.

These master images were then split into the 8 individual chips on the MOSAIC image. This splitting was done to accommodate the DAOPHOT PSF photometry package, which has limits on image size. The individual $2k \times 4k$ chips were the largest DAOPHOT could handle. In each chip (and for each master image), the process was the same. First, 400 candidate template stars were chosen to create a PSF. Next, the trimming process described in §4.1.4 was run, trimming the candidate list down to 250-300 template stars. Using this cleaned list, PSF parameters were determined, and then applied through ALLSTAR.

Photometric quality plots for the short and long sets are shown in figure 4.6. For reference, high quality photometry has uncertainties less than 0.05. The MOSAIC images provide this high quality data for $11 \leq V \leq 20$, covering nearly all of the stars within these clusters.

The ALLSTAR-derived magnitudes must be transformed to a standard system, in order to be comparable to other results. For calibration, photometry from the individual chips were re-combined to produce single photometry files for each master image, then matched to previously published “standard” photometry. For M36, the previously published *UBVI* photometry from Sharma et al. (2006) was used to transform the instrumental MOSAIC magnitudes to the standard system. The only published optical

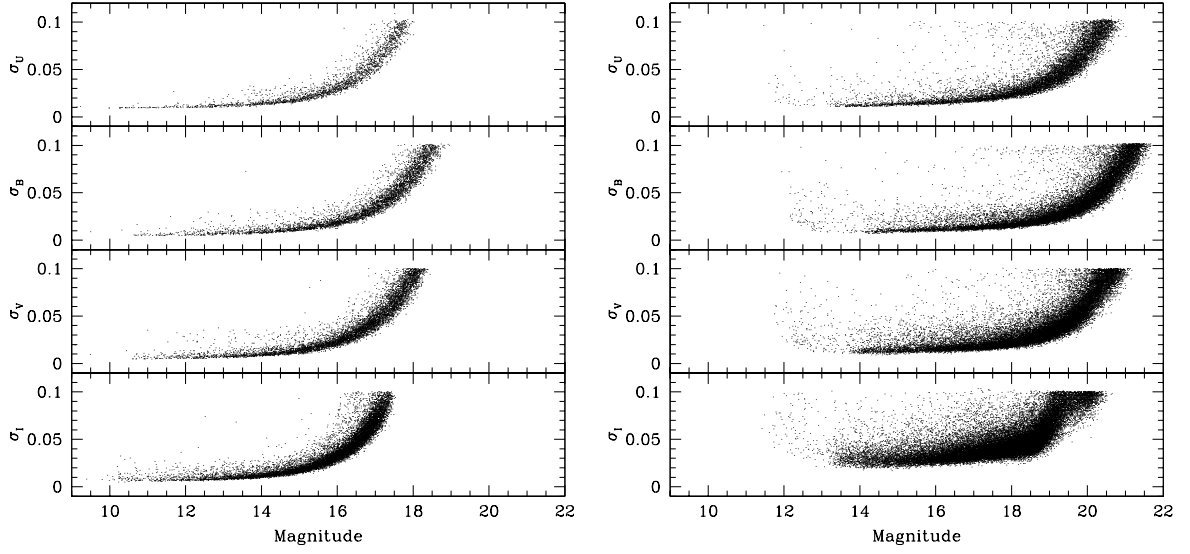


Figure 4.6: MOSAIC photometric quality plots for M36 in *UBVI*. *Left*: Short set of exposures. *Right*: Long set of exposures.

photometry on M38 is in Pandey et al. (2007), which only contains *BVI* photometry. *U* magnitude data was discarded for M38.

Sources detected in the MOSAIC images were matched to the published photometry for each cluster, producing between 500 – 600 matches for each filter. Using these common stars, the instrumental ALLSTAR magnitudes were transformed via the following equations:

$$u = U + a_U + b_U \times (U - B) \quad (4.1)$$

$$b = B + a_B + b_B \times (B - V) \quad (4.2)$$

$$v = V + a_V + b_V \times (B - V) \quad (4.3)$$

$$i = I + a_I + b_I \times (V - I) \quad (4.4)$$

Cluster	Filter	Length	a	b
M36	<i>U</i>	Short	1.843 ± 0.009	0.008 ± 0.011
		Long	-0.650 ± 0.010	-0.053 ± 0.008
	<i>B</i>	Short	1.191 ± 0.004	-0.105 ± 0.005
		Long	-1.305 ± 0.005	-0.127 ± 0.006
	<i>V</i>	Short	1.536 ± 0.003	0.048 ± 0.004
		Long	-0.928 ± 0.005	0.034 ± 0.006
	<i>I</i>	Short	1.993 ± 0.004	0.002 ± 0.004
		Long	-0.562 ± 0.011	-0.000 ± 0.011
M38	<i>B</i>	Short	1.390 ± 0.006	-0.245 ± 0.009
		Long	-0.976 ± 0.005	-0.254 ± 0.006
	<i>V</i>	Short	1.668 ± 0.005	-0.063 ± 0.006
		Long	-0.254 ± 0.005	-0.051 ± 0.005
	<i>I</i>	Short	2.061 ± 0.005	-0.120 ± 0.005
		Long	-0.392 ± 0.006	-0.083 ± 0.015

Table 4.2: Transformation coefficients for MOSAIC photometry.

Here, lowercase filter letters indicate instrumental (ALLSTAR-derived) magnitudes, while uppercase filters are those of the standard photometry. The transformation coefficients for each cluster and filter are located in table 4.2. Transformations were done separately for the short and long exposure sequences. Residuals for these transformations are shown in figure 4.7. Once the instrumental magnitude were calibrated to the standard system, all photometry was combined into a single master catalog.

4.3.2 Near-Infrared Data Sources [1.0 – 2.5 μm]

2-Micron All Sky Survey (2MASS): Similar to the goals of SDSS Legacy Survey, 2MASS aimed to observe the entire sky in the near-IR and catalog all detected stars and galaxies (Skrutskie et al. 2006). To image the entire sky, 2MASS utilized two different observatories: Mt. Hopkins in Arizona for the northern hemisphere, and Cerro Tololo Inter-American Observatory (CTIO) in Chile for the southern hemisphere. Beginning

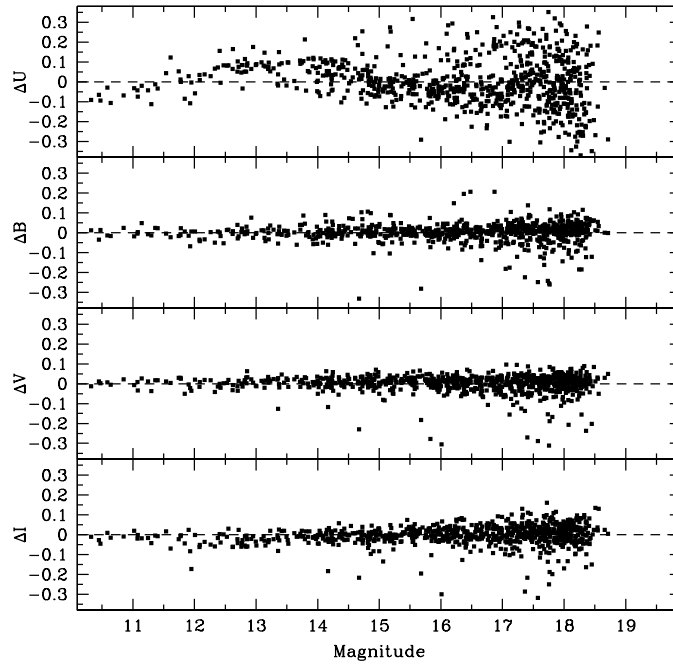


Figure 4.7: Residuals from transformation to standard system for M36 MOSAIC photometry.

operations in 1997, 2MASS achieved its goal by 2001; covering over 99% of the sky, and cataloging more than 300 million point sources.

Each 2MASS telescope utilized a custom camera in order to efficiently image the sky using all 3 near-IR filters (JHK_S). Instead of revisiting the same area of sky three times, the 2MASS instrument observed using all three filters in parallel. Incoming light is split using a dichroic for the J filter. Light below a certain wavelength is reflected to the J filter camera, while the rest of the light is transmitted. Another dichroic, this time for the H filter, splits the remaining light to the H and K_S filters. Each filter is coupled with a HgCdTe IR detector. Using this setup, shown in figure 4.8, each field can be observed in all filters under the same conditions.

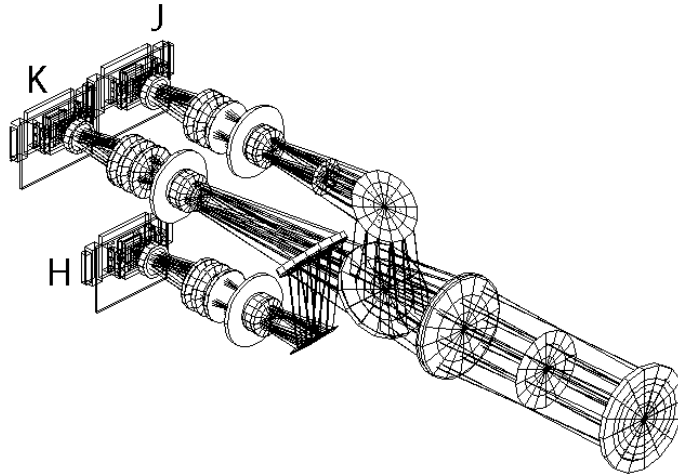


Figure 4.8: Diagram of 2MASS Camera. Each filter is labeled.

While 2MASS provides near-IR photometry for all of the clusters in our study, the data set is *shallow* — it only contains fairly bright stars — with limiting magnitudes in JHK_S of 16, 15, and 14.5, respectively. These magnitude cut-offs limit the effectiveness of 2MASS for low-mass stars within clusters, and for distant clusters. 2MASS photometry must be supplemented by other, deeper, near-IR data.

NOAO Extremely Wide Field Infrared Imager (NEWFIRM): NEWFIRM is a 1-2.4 μm IR camera, containing 2MASS JHK_S filters, and located on the Mayall 4-m telescope at KPNO (Probst et al. 2004). NEWFIRM consists of a grid of four 2048-by-2048 InSb detectors to create a 4096-by-4096 image, as shown in the left panel of figure 4.10. NEWFIRM’s field of view is a quarter of a square degree (half degree on each side), however this only covers a portion of some of the largest clusters within the sample. To cover the total spatial extent of the cluster, NEWFIRM images were taken in “4Q” mode, which takes four images of the cluster with the center of the cluster located in the

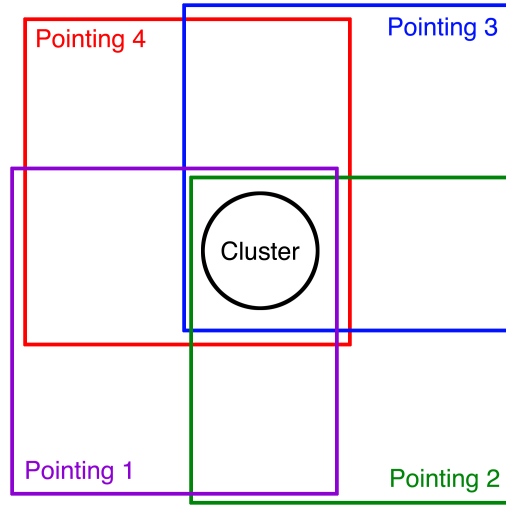


Figure 4.9: Diagram of NEWFIRM’s “4Q” mode. Cluster is centered in each of the four NEWFIRM chips for each image.

center of each chip. A diagram of the four pointings for “4Q” mode is shown in figure 4.9. “4Q” mode increases the imaged spatial extent to $43'$ on each side, enough to cover the large clusters in the sample.

Several clusters within the sample were observed with NEWFIRM by TCU over several different runs. An observing log is shown in table 4.3.

The NEWFIRM images were reduced at TCU using a similar approach to that of the MOSAIC data. First, all images on a cluster were combined to form three master images, one for each filter. A master stacked image of M37 J -band data is shown in the right-hand panel of figure 4.10. Each of the master images were run through DAOHPOT and ALLSTAR to produce magnitudes. Initially, 2000 candidate PSF stars were chosen for “4Q” mode images, and 1000 candidate PSF stars for non-“4Q” images. This list of candidates was trimmed using the procedure outlined in §4.1.4. After trimming, between

Date	Cluster	Filter	Exposure Time	Notes
26 Feb 2008	NGC 2682 (M67)	<i>J</i>	40×60s	“4Q” mode
		<i>H</i>	40×60s	“4Q” mode
		<i>K_S</i>	60×60s	“4Q” mode
27 Feb 2008	NGC 2099 (M37)	<i>J</i>	40×60s	“4Q” mode
		<i>H</i>	40×60s	“4Q” mode
		<i>K_S</i>	60×60s	“4Q” mode
	NGC 2168 (M35)	<i>J</i>	40×60s	“4Q” mode
		<i>H</i>	40×60s	“4Q” mode
		<i>K_S</i>	60×60s	“4Q” mode
2 Feb 2013	NGC 1960 (M36)	<i>J</i>	10×60s	
		<i>H</i>	10×60s	
		<i>K_S</i>	15×60s	
	NGC 2420	<i>J</i>	20×60s	
		<i>H</i>	20×60s	
		<i>K_S</i>	30×60s	
	NGC 1912 (M38)	<i>J</i>	10×60s	
		<i>H</i>	10×60s	
		<i>K_S</i>	15×60s	
25 Nov 2013	NGC 1817	<i>J</i>	20×60s	
		<i>H</i>	20×60s	
		<i>K_S</i>	30×60s	
	Berkeley 39	<i>J</i>	50×60s	
		<i>H</i>	30×60s	
		<i>K_S</i>	40×60s	
26 Nov 2013	NGC 188	<i>J</i>	20×60s	
		<i>H</i>	20×60s	
		<i>K_S</i>	30×60s	
	NGC 2158	<i>J</i>	15×60s	
		<i>H</i>	15×60s	
		<i>K_S</i>	15×60s	

Table 4.3: NEWFIRM observing logs for all runs. Original 2008 data taken in “4Q” mode, while all other clusters were small enough to fit into a single NEWFIRM field of view.

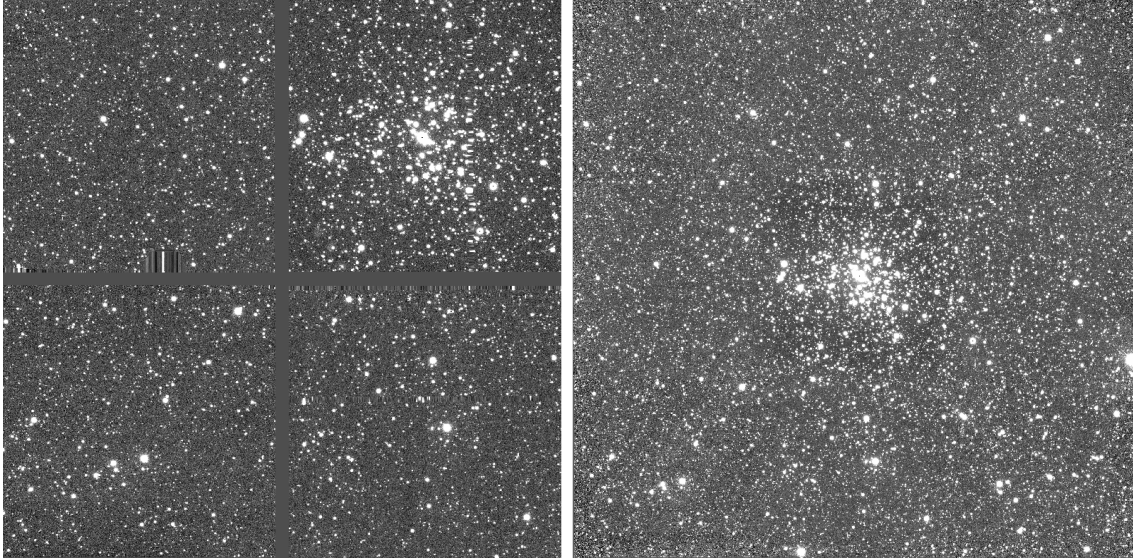


Figure 4.10: Examples of NEWFIRM images. *Left*: Single 60s J -band image of M37, covering a $27' \times 27'$ field of view. Note the large chip gaps, and the centering of M37 within a single NEWFIRM chip. *Right*: Master stacked image of M37 in J , covering a larger $44' \times 44'$ field of view.

700 and 1200 stars were left to determine a PSF. The PSF was then applied to all sources through ALLSTAR.

A plot of uncertainty as a function of stellar magnitude is shown in figure 4.11. For reference, high quality photometry is usually any source with a uncertainty under 0.05, and any source with an uncertainty under 0.1 is considered acceptable for use. 2MASS magnitudes end around $J \sim 15.5$, with high-quality NEWFIRM sources extending another 2.5 magnitudes deeper. The NEWFIRM photometry will allow probing of very low-mass stars in the near-IR.

NEWFIRM instrumental magnitudes were tied to the standard system using 2MASS photometry. The NEWFIRM sources were matched to ‘AAA’-quality 2MASS sources, meaning the magnitude measurement was deemed the best level possible in all 3 bands. The number of overlapping stars was significant for each of the reduced clusters, varying

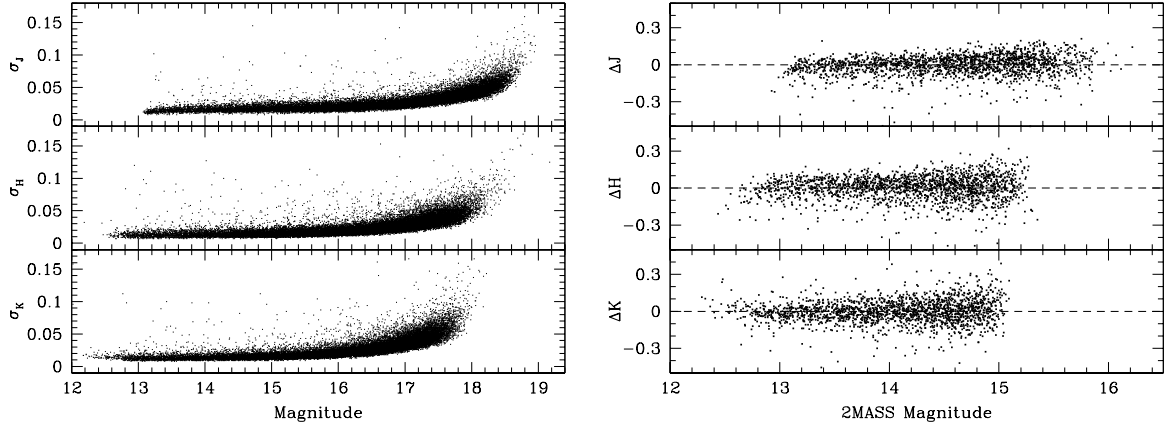


Figure 4.11: *Left:* Plot of NEWFIRM photometric quality for the cluster M37. *Right:* Plot of residuals in the transformation between ALLSTAR-derived magnitudes and 2MASS standards for M37.

between 700 and 2000 stars, depending on cluster density and imaging spatial coverage.

Using these overlapping stars, transformation equations were determined:

$$j = J + a_J + b_J \times (J - K_S) \quad (4.5)$$

$$h = H + a_H + b_H \times (H - K_S) \quad (4.6)$$

$$k_S = K_S + a_K + b_K \times (J - K_S) \quad (4.7)$$

Here, as with the MOSAIC photometry, lowercase letters correspond to NEWFIRM instrumental magnitudes, while uppercase corresponds to 2MASS standard magnitudes. Transformation coefficients for the clusters analyzed so far are shown in table 4.4. Residuals for the standard transformation in M37 are shown in figure 4.11. After transforming each filter's photometry to the standard system, JHK_S magnitudes were merged to create final photometry files for each cluster.

Cluster	J	H	K_S
NGC 2168 (M35)	$a_J = 2.397 \pm 0.003$ $b_J = -0.099 \pm 0.005$	$a_H = 2.297 \pm 0.002$ $b_H = -0.296 \pm 0.012$	$a_K = 3.030 \pm 0.005$ $b_K = 0.093 \pm 0.007$
NGC 1960 (M36)	$a_J = 2.441 \pm 0.004$ $b_J = -0.056 \pm 0.006$	$a_H = 2.620 \pm 0.003$ $b_H = -0.177 \pm 0.018$	$a_K = 3.063 \pm 0.004$ $b_K = 0.042 \pm 0.006$
NGC 2099 (M37)	$a_J = 2.434 \pm 0.004$ $b_J = -0.121 \pm 0.008$	$a_H = 2.318 \pm 0.003$ $b_H = -0.354 \pm 0.016$	$a_K = 3.020 \pm 0.005$ $b_K = 0.113 \pm 0.009$
NGC 1912 (M38)	$a_J = 3.004 \pm 0.004$ $b_J = -0.058 \pm 0.006$	$a_H = 2.973 \pm 0.003$ $b_H = -0.233 \pm 0.016$	$a_K = 3.547 \pm 0.004$ $b_K = 0.039 \pm 0.007$
NGC 2682 (M67)	$a_J = 2.445 \pm 0.007$ $b_J = -0.100 \pm 0.010$	$a_H = 2.277 \pm 0.004$ $b_H = -0.250 \pm 0.021$	$a_K = 2.956 \pm 0.010$ $b_K = 0.113 \pm 0.014$
NGC 2420	$a_J = 2.752 \pm 0.005$ $b_J = -0.036 \pm 0.008$	$a_H = 2.739 \pm 0.003$ $b_H = -0.234 \pm 0.020$	$a_K = 3.179 \pm 0.006$ $b_K = 0.130 \pm 0.011$

Table 4.4: Transformation coefficients for NEWFIRM photometry.

Due to the width of telescope (4m) and exposure time (60s), many of the very brightest stars are saturated in the NEWFIRM images. To recover data from these stars, the NEWFIRM photometry is merged with the ‘AAA’-quality 2MASS sources used for calibration. 2MASS provides photometry for bright members of the cluster, where NEWFIRM is saturated, and the NEWFIRM images extend the usable photometry several magnitudes below where 2MASS is useful.

Infrared Side Port Imager (ISPI): Dr. Frinchaboy, along with collaborator Karen Kinemuchi, obtained deep near-IR data of the clusters IC 4651 and Collinder 261 taken with ISPI on the Blanco 4-m telescope at CTIO. ISPI consists of a 2048-by-2048 HgCdTe IR detector with a 10 arcminute field of view. Due to the small field of view, images cover only the core of each cluster. Photometry has been completed (Kinemuchi, *private communication*), yielding magnitudes down to $J \sim 18$.

4.3.3 Mid-Infrared Data [2.5 – 10 μm]

Wide-Field Infrared Survey Explorer (WISE): Analogous to SDSS in the optical and 2MASS in the near-IR, WISE is an all-sky survey in the mid-IR, from 2 – 22 μm (Wright et al. 2010). Mentioned in §1.1.2, atmospheric absorption beyond 2.5 μm becomes too strong to attempt observations from the ground, so the WISE telescope is located in space. Throughout its main mission lifetime, from Jan 2010 to Aug 2010, WISE imaged the entire sky in each of its four mid-IR filters: [3.4][4.6][12.0][22.0].

To image the entire sky in such a short amount of time, the 0.4m WISE telescope had a large $47' \times 47'$ field of view. The WISE detector is a 1024×1024 SiAs detector, giving WISE a relatively large spatial resolution of $6''$ (or worse for higher wavelength filters). For accurate mappings of stars within dense environments, a high resolution data source is needed.

Infrared Array Camera (IRAC): Deep mid-IR data in this project were taken using the *Spitzer* Space Telescope’s IRAC instrument (Fazio et al. 2004), which operates with four filters: [3.6][4.5][5.8][8.0]. For the shorter wavelength IRAC filters, [3.6][4.5], an InSb IR detector is used. For longer wavelengths, InSb detectors do not work (band gap limiting wavelength of 5 μm); the two longer wavelength IRAC filters, [5.8][8.0], are fed to a SiAs detector instead.

IRAC observations were obtained of all 16 clusters in the dataset. The data were taken in High Dynamic Range (HDR) mode, which captures two images: a 1.2s image and a 30s image. The two images are then combined in order to “fix” saturation of

bright stars in the 30s image by using data from the 1.2s image. This approach provides photometry for both bright and faint cluster stars simultaneously.

The photometry was processed utilizing the Galactic Legacy Infrared Mid-Plane Survey Extraordinaire (GLIMPSE) data pipeline (Benjamin et al. 2003), which was modified to handle the HDR data. Average limiting magnitudes in each band are 18, 17, 15 and 14, respectively. The IRAC instrument provides much sharper detail than WISE, with spatial resolution of approximately $1.8''$ in all four bands. This allows for accurate separation of sources within cluster cores.

IRAC photometry exists only for a small area around each cluster, usually $20'$ in radius. To supplement IRAC across the entire spatial extent of the cluster, it would be ideal to combine the WISE and IRAC photometry into a uniform dataset. With fairly similar central wavelengths, the WISE [3.4] and [4.6] filters are candidates to be matched to [3.6] and [4.5] IRAC filters. IRAC and WISE photometry on the cluster M37 were matched to determine a transformation between the two systems. Residuals between IRAC and WISE for the 1400 matching stars are shown in figure 4.12.

For bright stars, the transformation is nearly constant, but diverges non-linearly for faint stars. For this reason, the transformation is limited to stars with $[3.4] < 14$ and $[4.6] < 13.5$. Within this region, [3.4] and [3.6] magnitudes are interchangeable, requiring no transformation parameters. [4.6] and [4.5] magnitudes are only slightly offset from one another, with $[4.5] = [4.6] - 0.05$. As seen in figure 4.12, there is no trend with color in the transformation. Using these simple transformation equations, the IRAC and WISE datasets can be merged into a master mid-IR catalog which covers the entirety of any cluster in our sample.

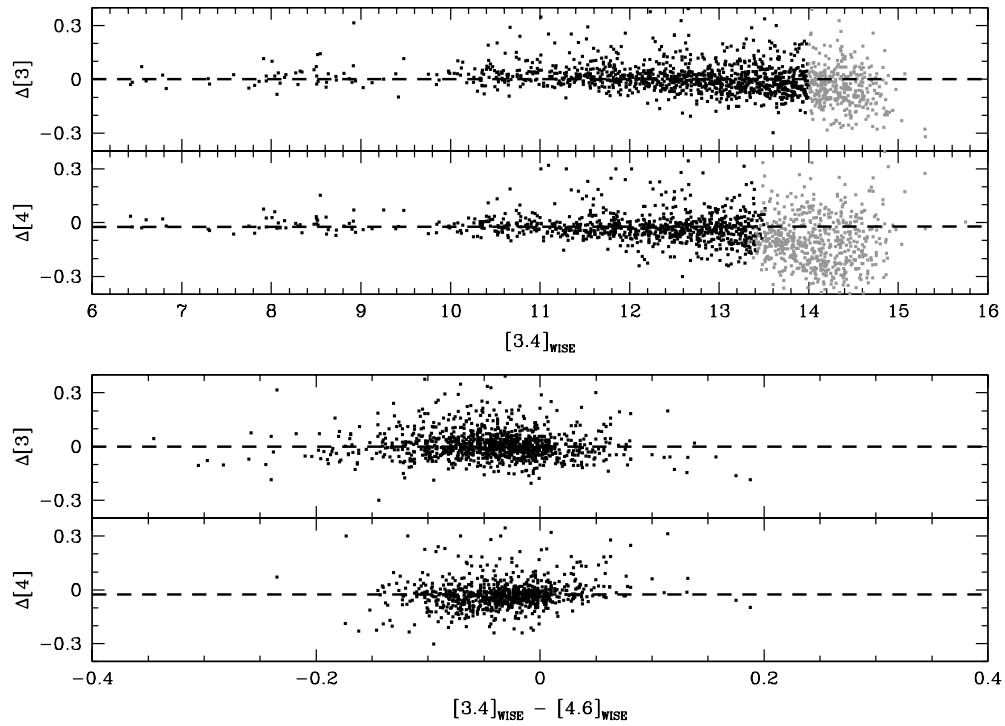


Figure 4.12: Residuals between IRAC [3.6][4.5] magnitudes and WISE [3.4][4.6]. $\Delta[3]$ indicates residuals between the 3 μm bands of each instrument, while $\Delta[4]$ indicates the difference in 4 μm magnitudes. Black dots indicate stars where the transformation is valid ($[3.4] < 14$ and $[4.6] < 13.5$), while grey dots indicate stars outside the transformation region.

4.3.4 Membership Data

When taking an image of a cluster, not all stars detected within the frame are *members* of that cluster. Stars that fall along the same line of sight, but are in front of or behind the cluster will be confused with cluster stars on a two-dimensional image. As the BINOCS analysis assumes all stars will have similar properties, removing these contaminants is beneficial to the final BINOCS results. There are two methods that can give estimates on “membership probability” for stars within the cluster area.

Radial Velocity (RV) Data: While RV surveys are not the most efficient method for detecting binary systems within a cluster (as described in §3.1.2), data from these studies can provide estimates of membership probability. Stars within the cluster are assumed to be moving at the same speed along the line of sight, with only a small dispersion due to their motion within the cluster. After measuring the average RVs for a large number of stars within the cluster, an estimate on the average cluster RV and cluster dispersion can be determined. Any stars outside of this range are denoted as non-members.

RV studies are also useful as tests on the BINOCS results. RV surveys, by determining the variance in a star’s RV over time, can flag binary and single stars within a cluster. By comparing the RV multiplicity determination to that from the BINOCS routine, the accuracy of the new method can be established. Additionally, accurate mass ratios can be determined for double-lined binary systems, of which there are several within our cluster sample. BINOCS mass determinations can be compared to that of the RV method.

Proper Motion (PM) Data: While RV surveys measure a star’s motion along the line of sight, proper motion studies compute stellar motion along the other two axes. Proper motion studies take images of a cluster (or other region of interest) over a long time baseline — usually years, if not decades — and correlate star positions through time. This is most often done by matching the positions of galaxies in each of the images and assuming they have not moved; a safe assumption considering the vast distance other galaxies are from Earth. Once galaxies have been matched, shifts in star position between the two images are calculated. Proper motion velocities are then reported in arcsec/yr. Because no distances can be assumed, the angular velocity (arcsec/yr) cannot be converted into linear velocities (km/yr, pc/yr, etc.).

Just as all cluster stars are assumed to have the same RV, all stars should have the same PM (within an intrinsic dispersion due to intra-cluster motion). Once the PM of all stars are determined, the average PM in x and y are determined, along with an estimated scatter for the cluster. Stars outside of this two-dimensional cut are marked as non-members.

Because PM studies rely on imaging, not spectroscopy, and because they rely upon including galaxy sources within the frames, PM data is *deep*. Often, PM determinations will extend to stars with $V \sim 25$. Quality proper motion studies will allow cleaning of the entire dataset before being fed to the BINOCs routine, removing much of the possible contamination. The BINOCs code can also make determinations about cluster membership, and proper motion data will allow testing of that feature as a function of magnitude.

Cluster	Visual Data	Near-IR Data	Membership Data
Berkeley 39		<i>NEWFIRM</i>	
Collinder 261	Gozzoli et al. (1996)	ISPI	
IC 4651		ISPI	
Melotte 66		ISPI	
NGC 188	von Hippel & Sarajedini (1998) Stetson et al. (2004)	<i>NEWFIRM</i>	Geller et al. (2008) Platais et al. (2003)
NGC 1039 (M34)	Jones & Prosser (1996)		Jones & Prosser (1996)
NGC 1817		<i>NEWFIRM</i>	Balaguer-Núñez et al. (2004)
NGC 1912 (M38)	MOSAIC	NEWFIRM	
NGC 1960 (M36)	MOSAIC	NEWFIRM	Sanner et al. (2000)
NGC 2099 (M37)	Hartman et al. (2008)	NEWFIRM	
NGC 2158	MOSAIC	<i>NEWFIRM</i>	
NGC 2168 (M35)	MOSAIC	NEWFIRM	Geller et al. (2010)
NGC 2420	An et al. (2009)	NEWFIRM	
NGC 2682 (M67)	An et al. (2009) Yadav et al. (2008)	NEWFIRM	Mathieu et al. (1997) Yadav et al. (2008)
NGC 6791	An et al. (2009)	Carney et al. (2005)	
NGC 6819	Hole et al. (2009)		Hole et al. (2009)

Table 4.5: Available data for all clusters in this project. Names in italics represent observed data that has not yet been reduced.

4.3.5 Data Overview

Table 4.5 summarizes the available data for use in this project, from the sources listed above, as well as from literature. 2MASS, WISE, and IRAC data are available for all clusters and are therefore not listed in table 4.5. Data sources in italics are not yet reduced, and not currently available for analysis.

Each of the cluster datasets in table 4.5 have different levels of completeness, which will dictate which analysis projects the cluster can be included in. Clusters with complete photometry, although some may only have shallow 2MASS near-IR magnitudes, can have bulk binary population parameters determined, while complete deep photometry is necessary for the more detailed radial distribution analysis. 16 clusters were targeted for this project, but only 8 have the full wavelength coverage necessary for global binary population statistics. Clusters such as Collinder 261 and M34 have data sets in all wavelength ranges, but some photometry is too shallow, or too sparse to be useful for analysis. Of the 8 clusters with complete photometry, 4 have wide-field, *deep* data sets

Cluster	Complete Photometry	Bulk Binaries	Detailed Analysis
Berkeley 39			
Collinder 261	X		
IC 4651			
Melotte 66			
NGC 188	X	X	
NGC 1039 (M34)	X		
NGC 1817			
NGC 1912 (M38)	X		
NGC 1960 (M36)	X	X	X
NGC 2099 (M37)	X	X	X
NGC 2158	X	X	
NGC 2168 (M35)	X	X	X
NGC 2420	X	X	
NGC 2682 (M67)	X	X	X
NGC 6791	X	X	
NGC 6819	X		

Table 4.6: Possible analysis avenues for each cluster in targeted sample. Bulk binary parameters will be discussed in §7, while detailed binary analysis will be explored in §8.

available, which are needed for detailed analysis of the binary populations themselves. A list of clusters, and the analysis possible for each, is shown in table 4.6.

While this project’s main focus is on the BINOCS routine and binary detection, its contribution to open cluster photometry should not be understated. Despite being very important astronomical objects, there is a dearth of published photometric data on open clusters. While many of these clusters have been observed dozens of times in the optical, the only IR photometry available is from 2MASS and WISE, which barely reaches below the turn-off. Providing deep, wide-field photometry, especially in the IR, for these standard open clusters will aid many avenues of research in the astronomical community.

Chapter 5

Isochrone Systems

An isochrone is a set of model stars, varying in mass, with the same age and metallicity — a synthetic cluster. When plotted on a CMD, an isochrone should trace out the location of every single star in the cluster, except for those already evolved beyond the AGB. As described in §3, these single models are then combined to form the full binary library that are compared against observation. The BINOCs results are only as good as the underlying models themselves, and despite years of refinement, stellar structure models have not yet been perfected. Competing isochrone systems, which adopt different physical inputs than one another, show significant differences along the main sequence, which is perhaps the most well-understood phase of stellar evolution. We test several competing stellar structure models against our observed data to determine which system is most consistent with the observed data.

5.1 Isochrone Physics

Stellar structure models compute stellar parameters through two phases of modeling. First, a *stellar core* is computed by building the star layer-by-layer. Using the mass and age of the star, stellar core models return two values: the star’s temperature and surface gravity. These two values uniquely determine a star’s position on the H-R diagram, with surface gravity becoming an analogue to luminosity. Using Newtonian gravity ($g = GM/R^2$), the radius of the star can also be inferred. On first approximation, the energy output of a star is a near-blackbody, governed by the temperature derived for the core model. In reality, the spectrum also has absorption lines from elements in the star’s atmosphere. A *stellar atmosphere* is generated using the temperature and surface gravity from the core model, as well as individual elemental abundances. Atomic and molecular absorption lines are overlaid on the blackbody spectrum and the synthetic flux is output.

Competing isochrone systems incorporate different physical assumptions, such as the equation of state (EOS) model, or the conductive and radiative opacity values, which govern energy transport within the stellar core. Some models use a very basic ideal-gas EOS, while others use a complex, computationally-intensive EOS that accounts for ionization, degeneracy pressure, and relativistic electron gas. Different models also differ on physical processes, specifying different mixing lengths for convection, and using alternate atmosphere models. Even basic physical parameters, such as the fraction of Helium within stars, the heavy-element mixture of the Sun, or solar metallicity, are not constant between systems.

System	Opacities	Equation of State
Dartmouth	$\log T > 4.5$: OPAL96 ⁴ $\log T < 4.3$: Ferguson et al. (2005)	$M > 0.8M_{\odot}$: Ideal Gas + Coulomb $M < 0.7M_{\odot}$: FreeEOS ⁷
Y ²	$\log T > 4.1$: OPAL96 ⁴ $\log T < 3.8$: AF94 ⁵	Rogers et al. (1996)
Padova	$\log T > 4.1$: OPAL93 ⁶ $\log T < 4.0$: AF94 ⁵	$\log T > 7.0$: Kippenhahn et al. (1965) $\log T < 7.0$: Mihalas et al. (1990)
PARSEC	$\log T > 4.2$: OPAL96 ⁴ $\log T < 4.1$: Marigo & Aringer (2009)	FreeEOS ⁷

	He Fraction	Z_{\odot}	Solar Composition	Atmosphere Model
Dartmouth	$0.245 + 1.54Z$	0.019	Grevesse & Sauval (1998)	PHOENIX ⁸
Y ²	$0.23 + 2.00Z$	0.018	Grevesse & Noels (1993)	Lejeune et al. (1998)
Padova	$0.23 + 2.25Z$	0.019	Grevesse & Noels (1993)	ATLAS9 ⁹
PARSEC	$0.2485 + 1.78Z$	0.015	Caffau et al. (2011)	ATLAS9 ⁹ (modified)

Table 5.1: Values for basic input physics for the four systems studied in this work.

⁴Iglesias & Rogers (1996)

⁵Alexander & Ferguson (1994)

⁶Iglesias & Rogers (1993)

⁷Irwin (2004)

⁸Ferguson et al. (2005)

⁹Castelli & Kurucz (2003)

In this work, we consider four well-known isochrone systems: Dartmouth (Dotter et al. 2007), Y² (Yi et al. 2001), Padova (Girardi et al. 2002), and PARSEC (Bressan et al. 2012). Values for many aspects of the input physics within these models are shown in table 5.1.

5.2 Comparison to CMDs

Isochrones are often fit to CMDs in order to assess their quality. The four isochrone systems studied in this work are compared to three CMDs of the cluster M37 in figure 5.1.

It is apparent from figure 5.1 that all isochrone systems fit well (and similarly) above $g \sim 19$, and diverge lower on the main sequence, to varying degrees. The BINOCs routine

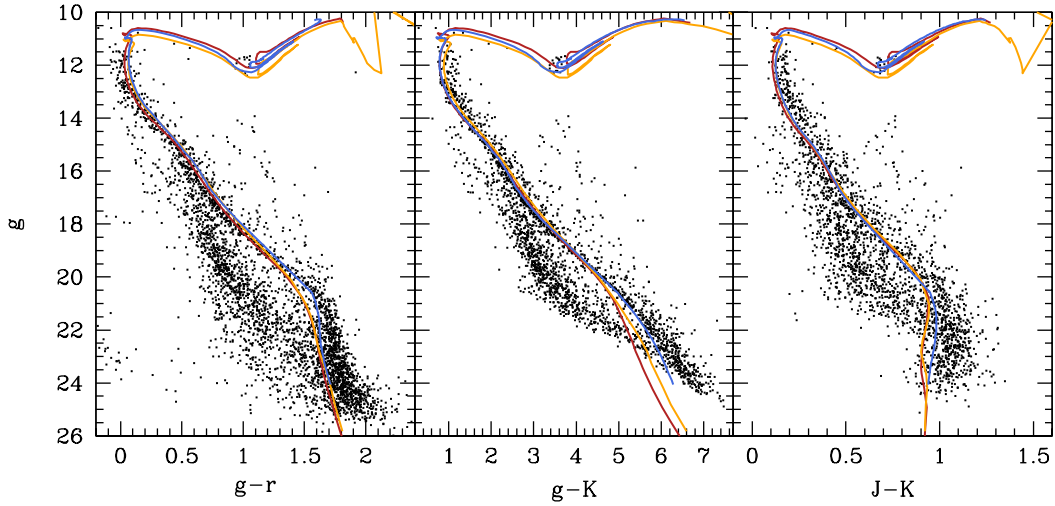


Figure 5.1: Comparison of isochrone systems to various CMDs of M37. *Red*: PARSEC; *Orange*: Padova; *Blue*: Dartmouth. All isochrones are 350 Myr, with $[\text{Fe}/\text{H}] = +0.08$, $E(B - V) = 0.30$, at a distance of 1386 pc.

builds synthetic binary stars using every possible combination of single stars within an isochrone model; deviations between observation and theory for low-mass stars will throw off fits to binary systems across the entire mass range. The isochrone models must be improved before they can be used to predict accurate masses of cluster stars.

An isochrone fit to several CMDs of one cluster, as seen in figure 5.1, can show that the isochrone systems diverge from observation at low mass, but does not provide information on *why* this occurs. Ideally, one would like to determine which of the physical inputs described in §5.1 improve an isochrone fit, and which ones detract. To do this, isochrones must be compared to a range of clusters with different ages and metallicities. Using the clusters in our dataset for which we have complete photometric data, this procedure can be accomplished.

5.3 Isochrone Preparation

There are a large number of variables that differ between isochrone systems, even beyond those listed in table 5.1. If a comparison of models is to produce any useful insights, some of these variables must be removed from consideration. This can be done by standardizing some aspects of the isochrones.

5.3.1 Metallicity

The metallicity of an isochrone has a large affect on its shape. To compare isochrones of various systems to one another, each must have a common $[\text{Fe}/\text{H}]$. Y^2 isochrones can be interpolated to any required $[\text{Fe}/\text{H}]$ by an included FORTRAN routine. Padova and PARSEC isochrones are available for any metallicity from their online source, the interactive CMD 2.5 interface⁷. Dartmouth isochrones are also available with any metallicity from an online source⁸, but are only available for cluster ages > 1 Gyr. A “base grid” of Dartmouth isochrones are available, for any age, with $[\text{Fe}/\text{H}] = -1.0, -0.5, +0.07, +0.21, +0.36, +0.56$.

For each cluster, isochrones are generated with the metallicity denoted in table 4.1. For young clusters (< 1 Gyr), Dartmouth models will only be used if the cluster $[\text{Fe}/\text{H}]$ is within 0.01 dex of a “base grid” metallicity.

⁷<http://stev.oapd.inaf.it/cgi-bin/cmd>

⁸<http://stellar.dartmouth.edu/%7Emodels/webtools.html>

5.3.2 Age

Not all isochrone systems have a common age grid. Padova and PARSEC isochrones exist for constant steps of 0.05 in $\log(\text{Age})$, from 6.6 (4 Myr) to 10.1 (12.6 Gyr). Y² and Dartmouth isochrones, instead, exist in steps in linear Age. Y² spans the ages of 100 Myr to 13.5 Gyr, while Dartmouth covers the 250 Myr to 15 Gyr range. Due to the difference in age ranges between systems, and the $\log(\text{Age})$ vs linear Age steps, not all isochrone systems will have the exact age of a specific cluster.

For most clusters, the closest age may vary up to as much as 100 Myr between systems. As we are most interested in how isochrones model the main sequence, where BINOCS is most effective, this age difference will not cause any problems. Main sequence lifetimes are often in the Gyr timescale, with little change in properties; the 100 Myr difference between isochrone systems will not affect the results for main sequence stars.

5.3.3 Atmospheres

As seen in table 5.1, all isochrone systems use different atmosphere models, which poses a problem for understanding what physical processes improve isochrone fits. Stars with similar internal parameters (surface gravity, temperature), but different atmosphere models, may look high discrepant on a CMD. Any differences between isochrone systems in the stellar core phase may be overshadowed by differences in the atmosphere color-temperature relations.

To avoid this confusion, atmosphere models will be standardized across all isochrone systems, allowing for direct comparison of internal structure physics to observed data.

[Fe/H]	$\log g$	T	BC_V	$U - V$	$B - V$	$V - R$	$V - I$
+0.00	4.00	2000	-6.8210	7.9860	3.2970	4.1080	7.4740
-0.50	4.00	2000	-6.8210	6.8060	2.6950	3.7190	6.8120
+0.50	4.00	2000	-6.8210	7.2550	3.1260	3.5610	6.5120
-1.50	4.00	2000	-6.8210	7.7290	2.4500	4.3580	7.1940
-2.00	4.00	2000	-6.8210	8.6660	2.4300	4.1580	6.6450
-2.50	4.00	2000	-6.8210	9.8650	2.5310	3.7760	5.9720
-3.00	4.00	2000	-6.8210	9.5850	2.6400	3.0880	4.8850
-3.50	4.00	2000	-6.8210	9.5410	2.8980	2.5800	3.9990
-4.00	4.00	2000	-6.8210	8.7580	2.6850	2.1920	3.4510

Table 5.2: Sample of the first few lines and columns of the BT-Settl pre-computed color-temperature grid.

As we also wish to test the accuracy of the atmosphere models themselves, two alternate models will be applied to each isochrone: ATLAS9 (Castelli & Kurucz 2003), and BT-Settl (Allard et al. 2012).

ATLAS9⁹ and BT-Settl¹⁰ color-temperature relations were available from pre-computed grids online. The first few lines of the BT-Settl grid is shown in table 5.2. The star’s intrinsic parameters are taken as an input into the grid: [Fe/H], surface gravity ($\log g$), temperature, and *bolometric magnitude* — the magnitude determined from the full luminosity of the star. Using the full grid, the output columns are interpolated to the exact parameters of the star.

Output from the grid is the *bolometric correction* to V , BC_V . This is the difference between the star’s bolometric magnitude and its magnitude in the V filter: $V = M_{bol} - BC_V$. Also output are the colors of the star, all using the V filter (as seen in table 5.2). Using only the four input values, all magnitudes can be determined for the star. While table 5.2 only shown color terms for the Johnson-Cousins filter system, more filters are

⁹<http://wwwuser.oat.ts.astro.it/castelli/colors.html>

¹⁰<http://phoenix.ens-lyon.fr/Grids/BT-Settl/>

available in the atmosphere grids. BT-Settl grids contain color terms for all 17 filters used in the BINOCS routine: $UBVRIugrizJHK_S[3.6][4.5][5.8][8.0]$. ATLAS9 grids contain all filters but the IRAC mid-IR bands.

In the following analysis, observed data will be compared to 11 different isochrones. The original Padova, PARSEC, and Dartmouth isochrones will be compared to the observational data. The atmosphere model included with the Y² isochrones does not contain SDSS *ugriz* magnitudes, and will therefore not be compared to clusters with *ugriz* optical photometry. Using the original isochrone $\log g$ and T_{eff} values, new magnitudes are computed for ATLAS9 and BT-Settl atmospheres. The online ATLAS9 color transformation does not include mid-IR magnitudes, so no systems will be compared in those bands when using grid-derived ATLAS9 atmospheres. Additionally, ATLAS9 atmospheres are only available for stars with temperatures greater than 3500K. Stars in the Dartmouth and Y² systems with temperatures below this were removed in the ATLAS9 isochrones.

5.4 Empirical Ridgelines

Comparison of observed photometry to 11 different isochrones in up to 9 colors, for several clusters, will become unwieldy if CMDs are to be used. To simplify plotting and allow deeper understanding of the isochrone deviations, *empirical ridgelines* are used instead. Empirical ridgelines are hand-drawn traces of the observed single-star main sequence, as seen in figure 5.2. Instead of showing isochrones overplotted on a CMD to assess their fit, residuals between isochrone-predicted colors and empirical ridgeline colors can be shown

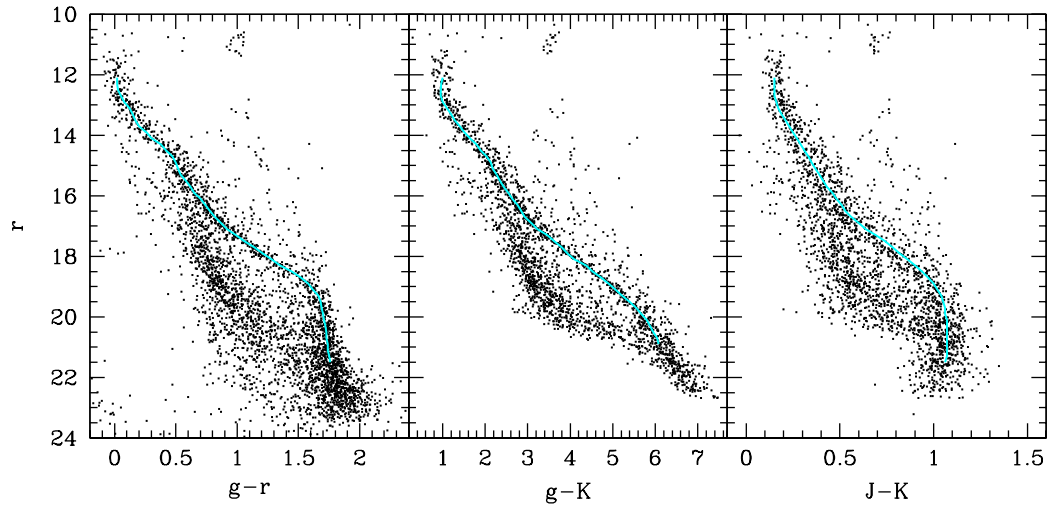


Figure 5.2: Empirical ridgelines for several CMDs of M37.

to illustrate the same concept. Small residuals in predicted vs observed colors will mean a good fit.

Empirical ridgelines have been determined for several clusters: M35, M36, M37, M67 and NGC 2420. These ridgelines were created by visual inspection of various cluster CMDs, and tracing the main sequence. Values for these ridgelines are located in appendix A.

5.5 Comparison

Clusters for which ridgelines exist were compared to isochrone systems. Residuals were computed for all 9 available CMDs, and are shown for select clusters in subsections below.

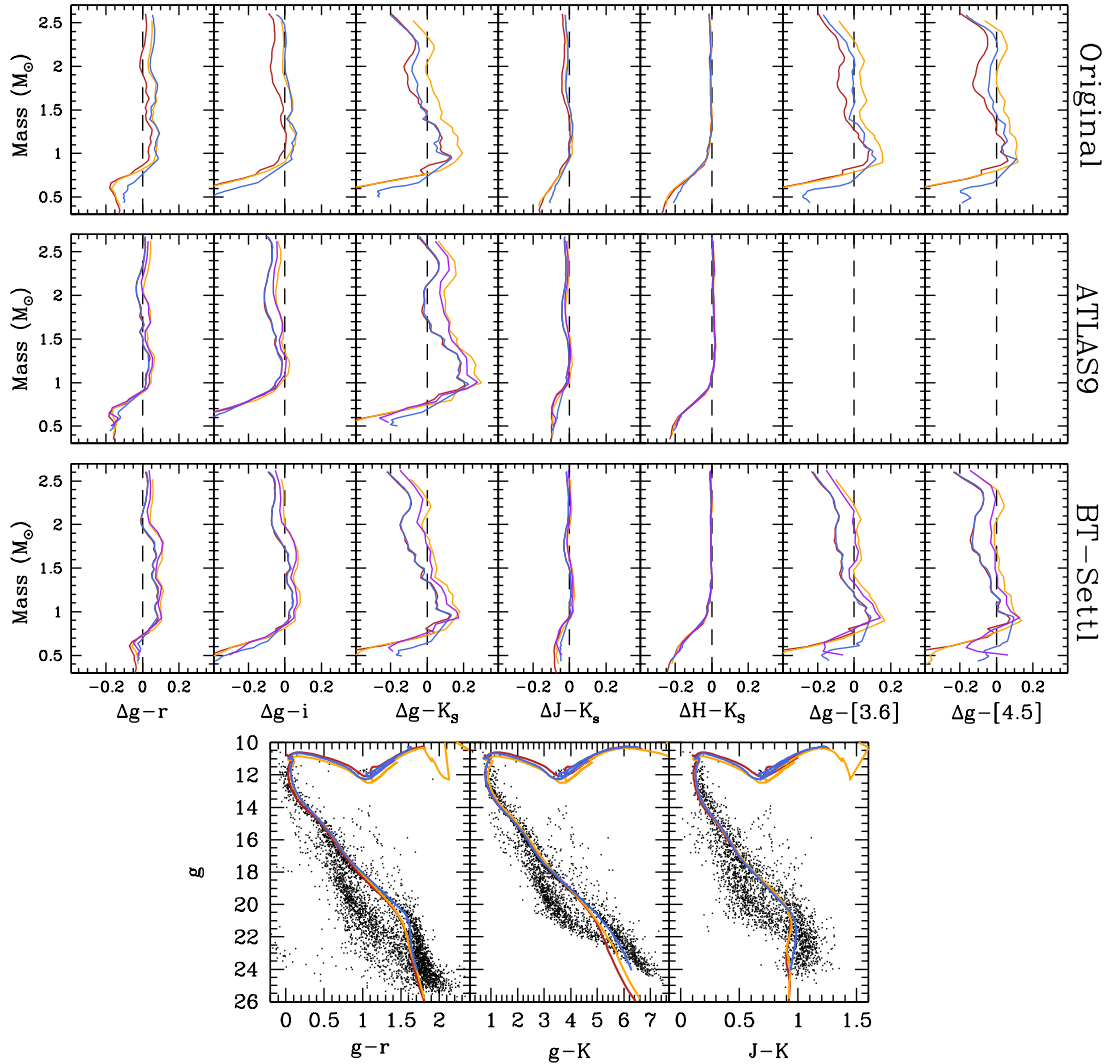


Figure 5.3: Comparison of isochrone systems to empirical ridgeline for M37 in 7 CMDs. *Top*: Residuals between empirical ridgeline and isochrones. *Bottom*: Comparison of isochrones to cluster CMD, using original atmosphere models. All isochrones are 350 Myr, with $[\text{Fe}/\text{H}] = +0.08$, $E(B - V) = 0.30$, at a distance of 1387 pc. *Red*: PARSEC; *Orange*: Padova; *Blue*: Dartmouth; *Purple*: Y². Y² isochrones do not contain Sloan colors, and are therefore not available in the original atmosphere plots.

5.5.1 M37

A plot of isochrone ridgeline residuals are shown for M37 in figure 5.3. For a majority of the mass range, from 0.9 to 2.5 M_{\odot} , all isochrone systems not only match each other closely, but also deviate very little from the empirical ridgeline. This is interesting, considering each system employs vastly different physical assumptions for high mass stars. For example, Dartmouth’s equation of state is a simple ideal gas, with a correction for coulomb interaction, while FreeEOS (used by PARSEC) handles ionization, degeneracy pressure and relativistic electron gas, yet the results end up nearly identical. The lack of difference is due to the fact that higher mass stars ($M > 0.9 M_{\odot}$) have sufficiently low density that the addition of non-ideal effects in the equation of state does not produce appreciable shifts in the stellar model. It appears that main sequence stellar parameters are insensitive to nearly all input physics for stars with masses between 0.9 and 2.5 M_{\odot} .

For stars less massive than 0.9 M_{\odot} , isochrone models begin to deviate from each other, and the observed data. Dartmouth and Y² isochrones fit observed colors to within 0.25 for nearly all CMDs and masses, while Padova and PARSEC isochrones deviate greatly for the $g - K_S$, $g - [3.6]$ and $g - [4.5]$ colors. Ideally, these deviations should be correlated with differences in input physics within the models.

Comparing Y² and Padova isochrone input physics in table 5.1, there are many similarities for low mass stars: the same opacity code, the same solar composition, and very similar He fractions and Z_{\odot} , yet the resulting ridgelines are highly discrepant. The only significant difference in physics for low mass stars in Y² and Padova isochrones are the equation of state code. Padova isochrones’ discrepant fits are not surprising, as the Mi-

halas et al. (1990) equation of state has been shown to produce inaccurate results even in the Sun (Dziembowski et al. 1992). All Padova isochrones will be affected by this inaccurate equation of state code.

While Padova’s deviation from observation is easily tied to the failure of the underlying equation of state, their successor, the PARSEC system, predicts even bluer colors than those from Padova. There are many differences between PARSEC and the other systems considered, with PARSEC being the only system with a difference value for Z_{\odot} . With only a single cluster being considered, it is hard to determine which of the varied parameters contribute to the bluer colors computed.

5.5.2 NGC 2420

A plot of isochrone ridgelines residuals for NGC 2420 are shown in figure 5.4. Similar to the results from M37, all isochrone systems match closely to the observed data for stars more massive than $0.9 M_{\odot}$. Also as before, the Padova and PARSEC isochrones deviate greatly from the empirical ridgeline, predicting far bluer colors than observed, while the Dartmouth and Y² isochrones match much more closely.

Dartmouth isochrones are useful in looking at atmosphere model effects, due to the poor fitting of Padova and PARSEC, and the non-existence of Sloan colors for Y² isochrones. ATLAS9 atmospheres appear to improve some colors ($g - K_S$, $g - [3.6]$, $g - [4.5]$), while making other residuals worse ($g - r$, $g - i$, $g - z$). BT-Settl atmospheres, on the other hand, improve every color residual for NGC 2420 with respect to the ATLAS9 and original atmosphere model isochrones. The BT-Settl atmosphere code

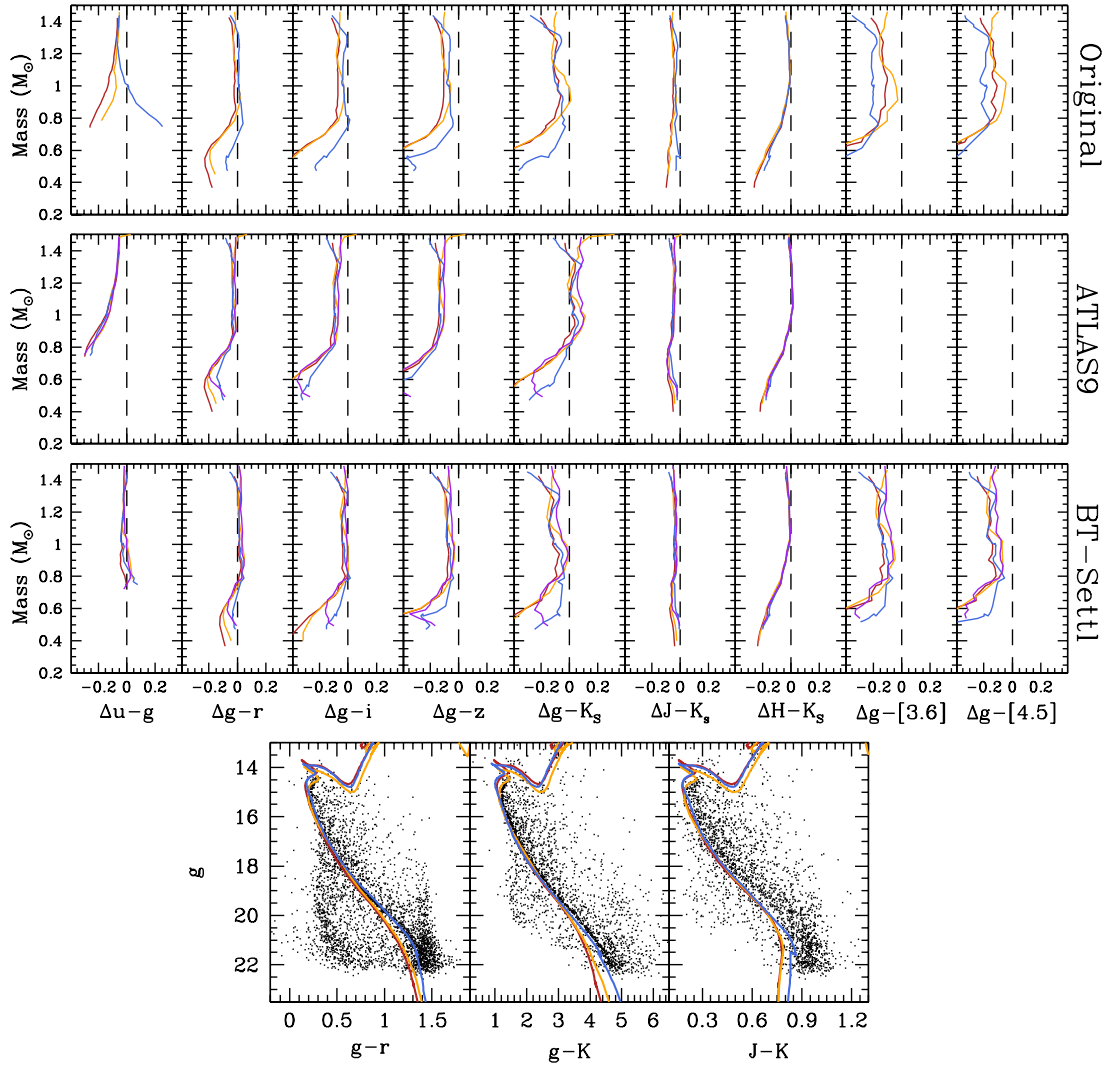


Figure 5.4: Same as figure 5.3, but for NGC 2420. All isochrones are 2.0 Gyr, with $[\text{Fe}/\text{H}] = -0.23$, $E(B - V) = 0.03$, at a distance of 2512 pc.

carefully handles molecular absorption lines in the stellar spectra, while ATLAS9 does not. It appears that these molecular absorptions may be important in predicting accurate colors, especially in the optical.

5.5.3 M67

Most of the isochrone behaviors noted for M37 and NGC 2420 also appear for M67, shown in figure 5.5. A notable difference from the previous two clusters is the erratic behavior of the Y^2 isochrones for low mass stars. Y^2 isochrones predict slightly bluer colors than observed for most low mass stars, similar to the other isochrone systems, but then quickly shift to predicting far *redder* colors than observed for stars $< 0.5 M_{\odot}$. While this behavior is most apparent for isochrones with the BT-Settl atmosphere, a similar behavior is observed in ATLAS9 isochrones as well. The ATLAS9 color grid does not exist for stars with temperatures less than 3500K, truncating ATLAS9 Y^2 isochrones just above $0.5 M_{\odot}$. Referring back to figures 5.3 and 5.4, similar behavior can be noted.

Y^2 isochrones are calibrated to low-mass stars in the open clusters Melotte 22 (Pleiades) and IC 2391, with well-matching colors. In the comparisons to observation above, the Y^2 isochrones are paired with an alternate atmosphere model. While low-mass Y^2 isochrones may match low-mass stars when paired with the original color-temperature relation, they may not with other atmosphere models. This point illustrates the need to divorce the underlying stellar structure model with the atmosphere, such that interplays between the two will not mask model deficiencies. There does not appear to be any underlying

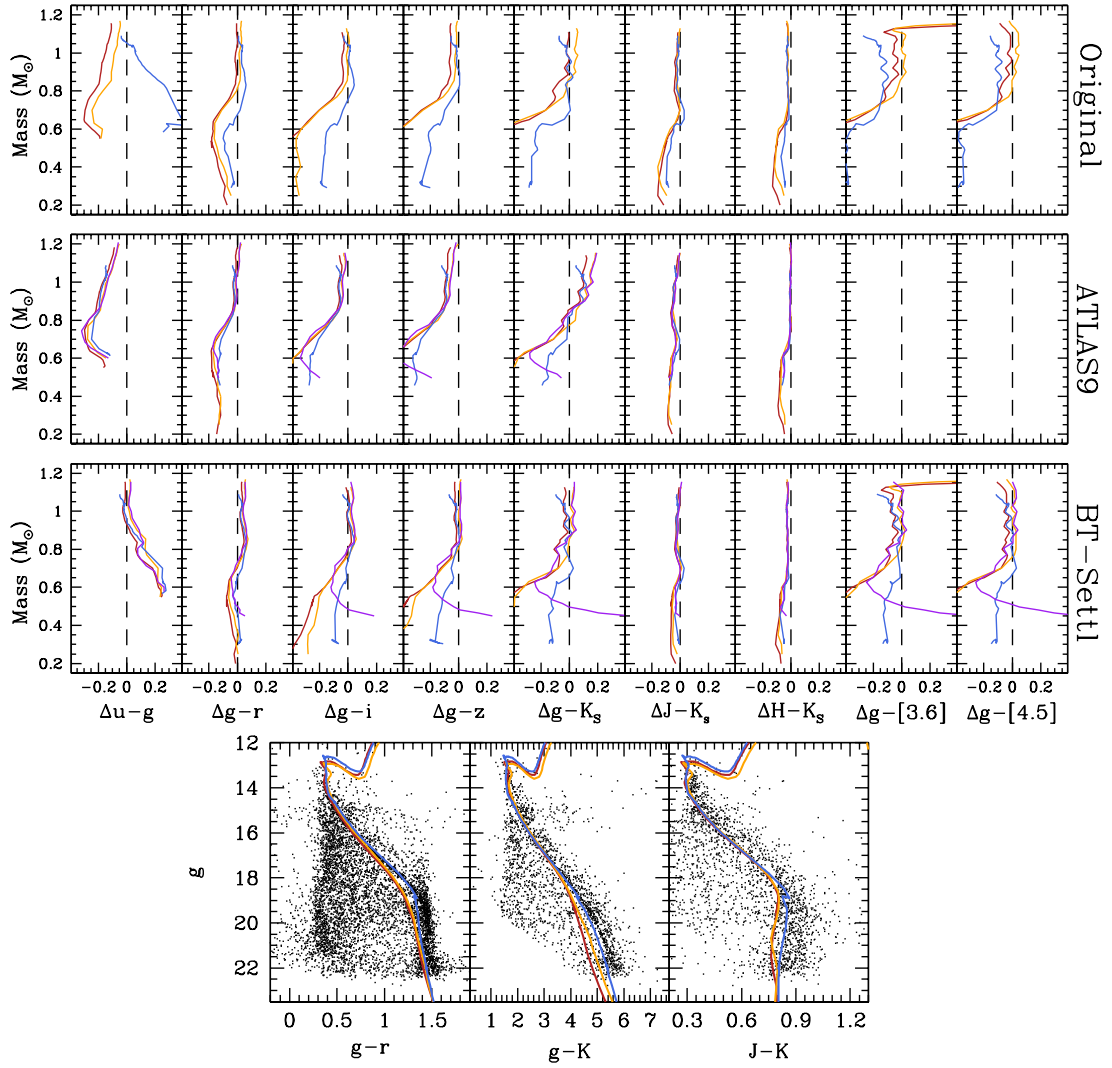


Figure 5.5: Same as figure 5.3, but for M67. All isochrones are 3.5 Gyr, with $[\text{Fe}/\text{H}] = +0.01$, $E(B - V) = 0.04$, at a distance of 855 pc.

physics or code changes around $0.5 - 0.7 M_{\odot}$, but the Y^2 stellar structure model seems to create stellar cores that have higher temperatures than observed.

5.6 Isochrone Adjustment

§5.5.1 - 5.5.3 highlighted some of the problems with popular isochrone systems, found very few underlying parameters than increase fit quality. Overall, the Dartmouth stellar structure model and the BT-Settl atmosphere code fit most closely to the open clusters in the analysis set. Even this configuration deviates from the observed empirical ridgeline by 0.1 or more, in color. While BINOCS improves upon current binary-detection techniques by lowering dependence on inclination, orbital period, and observational uncertainty, these improvements are traded for complete dependence upon the underlying isochrone model, as well as intrinsic cluster parameters such as distance and reddening. Even a 0.1 shift in color between observation and model will throw off any accurate mass determination.

Because no isochrone model accurately fits observation, the underlying models are adjusted to match by introducing a custom color-temperature relation. Before the isochrone is read into the BINOCS code, the bolometric-correction to r , and hence the r magnitude, is assumed to be “correct,” and all other colors are adjusted to those in the previously-determined empirical ridgeline. For stars not on the main sequence, where the empirical ridgeline does not exist, colors are shifted in order to keep the isochrone ridgeline continuous.

By manually adjusting the colors of the underlying isochrones, the BINOCS code is freed from much of the dependence on the underlying physics of the isochrone models. All future analysis will use the PARSEC isochrone system due to the fact that the lowest mass model in the isochrone is $0.13 M_{\odot}$, the lowest of all systems considered. While PARSEC is the worst-fitting isochrone system, all deviations are removed in the adjustment to the empirical color values.

Chapter 6

BINOCS Testing

When the BINOCS code was introduced in §3.3, several parameters were assumed: the number of iterations of the fitting, the the threshold to consider a magnitude “close,” and the required number of “close” filters. Each of these parameters were tested, and the results are shown below.

6.1 Number of Iterations

Monte Carlo methods are computational algorithms that use repeated random sampling to get estimates of quantities that are difficult (or impossible) to obtain analytically. In the case of BINOCS , there are associated uncertainties with magnitude measurements, but there is no straightforward way to propagate those errors into the derived mass estimates. Instead, a Monte Carlo approach is taken: the input magnitudes are randomly shifted by small amounts, and the process is iterated a number of times. At the end, uncertainties

in the mass estimates can be generated by computing at the standard deviation of all best-fit masses.

Because the Monte Carlo approach has random elements, it will not necessarily produce the same result every time. However, if there are enough iterations, the final result, which is the median of all iteration best-fits, will not vary greatly. Running excess iterations beyond this will use more computing time, but not enhance the results in any meaningful way. We wish to determine the optimal number of iterations in order to limit the variation between runs, but not waste computational power.

In this test, the *true* mass of each star is not important, only the variation between runs, and therefore observational data is used. The BINOCs code was run on this observed data with varying numbers of iterations: 3, 10, 30, 90, 150, 200, 300, 400, 500, 600, 700, and 1200. For each number of iterations, the BINOCs code was run five times. Using these five runs, a “% uncertainty”, Σ , was computed for each star. Σ is defined as the standard deviation of all five resulting masses divided by the average of the resulting masses for which the star is classified as a member. Σ ’s for primary and secondary mass determinations are computed independently. Stars that were classified as non-member stars in all five runs (and hence not given any best-fit masses) were removed from the set.

The M67 and M37 datasets were run through the test, and median and 95th percentile σ ’s were computed for each number of iterations. Results are plotted in figure 6.1. For primary star masses, there is very little shift between runs ($< 3\%$), regardless of the number of iterations completed. For secondary star mass determinations, the median Σ is also quite small, staying below 5% for all iteration values.

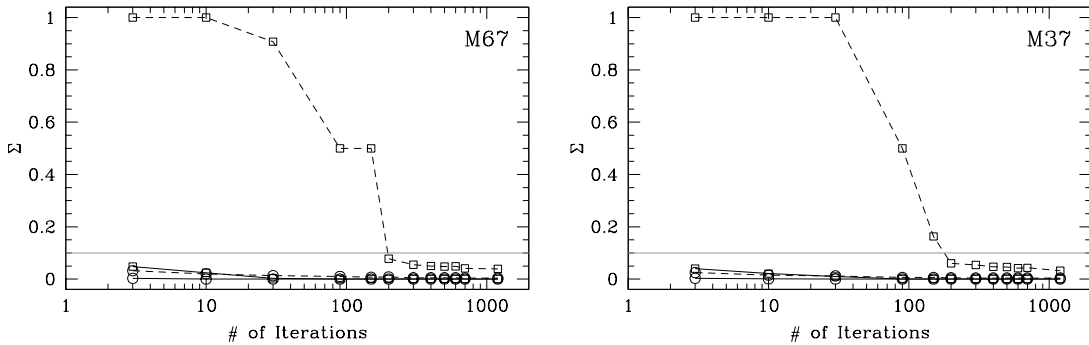


Figure 6.1: Results of the number of iterations test on M67 and M37. Circles correspond to Σ 's for primary masses, while squares correspond to secondary mass Σ 's. Solid lines show median Σ , dashed lines show 95th percentile. Grey line denotes average 10% uncertainty between runs.

In order to ensure that a majority of stellar mass determinations are roughly constant between runs, we require the 95th percentile Σ to be less than 0.1: on average, there will be a less than a 10% difference in derived stellar masses between runs for 95% of stars in the dataset. Using 200 iterations of the BINOCS fitting will satisfy this requirement (as seen in figure 6.1), and is chosen as the ideal number of iterations in the final computations.

6.2 Close Filter Threshold

When a cluster is imaged, the data will also contain non-member stars in front of, and behind, the cluster. The BINOCS technique is able to remove much of this contamination by determining whether stars have the required number of “close”¹ filters for *any* model. Therefore, the threshold which defines whether a filter is “close” will adjust the level of field star contamination within the sample. The smaller the threshold, the less contamination from true non-member stars. Conversely, if the threshold is too stringent, many

¹“close” means the sum element in (3.5) is greater than 7.

legitimate member stars may be discarded from the sample, due to intrinsic observational uncertainties.

Unlike the iterations test, this test relies on knowing the *true* membership of a data point. To test for the optimal threshold level, the synthetic model library generated by the BINOCS code was used as input. To simulate real observation, the model stars in the input library were given observational uncertainties derived from a specified cluster’s photometry. For each available filter in the cluster’s photometric catalog, average magnitude uncertainties were calculated in bins of width 0.5 mag. Stars in the input library were then assigned magnitude errors equal to $2 \times$ the uncertainty in the corresponding magnitude bin. The model stars’ magnitudes were also randomly shifted using a gaussian error distribution with $\sigma =$ the magnitude’s uncertainty. Only the *griJHK_S*[3.6][4.5] filters were kept in this observationally shifted catalog, to approximate the wavelength coverage in most cluster datasets.

The catalog was then copied three times: one as an exact copy, one where all magnitudes were shifted down by 0.8 mags, and one where all magnitudes were shifted up by 0.8 mags. The exact copy represents the cluster stars, while the shifted copies symbolize field contamination in front of and behind the cluster (refer to (1.8) in §1.1); shifting magnitudes down move stars closer, while shifting magnitudes up move stars further away. The magnitude difference between the single-star main sequence and equal-mass binary sequence is 0.753 (from (3.1)), so there should be no natural degeneracies between the three copies of the input library, though the shifts due to the simulated observational uncertainties will likely scatter some stars across these boundaries. The best threshold value will be chosen to optimally separate these copied datasets.

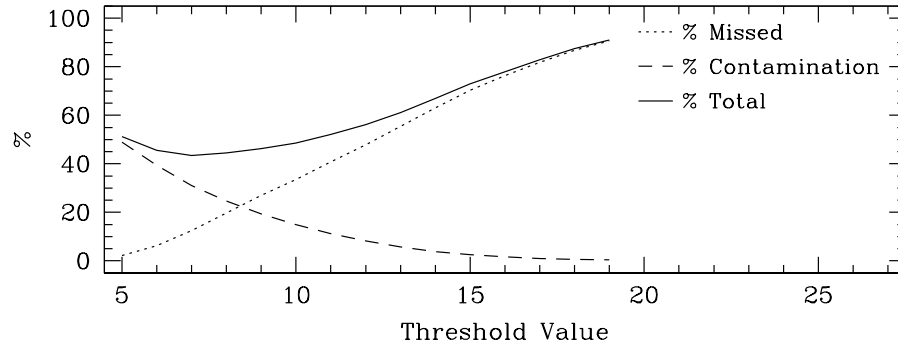


Figure 6.2: % contamination and % of stars missed in M67 synthetic dataset, for various threshold levels.

The BINOCS code was run on this input for various values of the threshold. After the run was complete, two numbers were computed: the percentage of member stars (from the copy of the library at the cluster’s distance) that were classified as non-members, and the percentage of non-member stars (from the other two copies of the library) that were classified as members. The best-fit threshold value is chosen such that the sum of these two values is at a minimum.

The test was run using the M67 synthetic dataset. Results are shown in figure 6.2. The threshold with the minimum total error is 7, which is chosen to be the optimal threshold for science runs.

6.3 Number of Required Filters

While a comprehensive sampling of the SED over all 12 filters (*UBVRI* or *ugriz*, $J-[8.0]$) is ideal, it is often impractical to obtain quality photometry in this number of bands for every cluster we wish to study. In practice, the BINOCS code will have to produce accurate results using a less-than-ideal number of filters. Requiring fewer filters to be “close” will

Filter Combinations	NGC 2682 (M67)			NGC 2099 (M37)			NGC 1960 (M36)		
	# Stars	% Error		# Stars	% Error		# Stars	% Error	
		M_{pri}	M_{sec}		M_{pri}	M_{sec}		M_{pri}	M_{sec}
101: <i>.g.....[3.6]...</i>	2218	1.5	16.1	7018	2.0	21.2	8047	1.6	38.9
111: <i>.g...J..[3.6]...</i>	1319	1.3	13.7	6253	1.7	16.6	8016	1.4	31.2
202: <i>.gr.....[3.6][4.5]..</i>	2005	1.2	12.3	3434	1.6	16.3	7064	1.9	26.4
211: <i>.gr..J..[3.6]...</i>	1294	1.1	12.0	6253	1.5	15.2	8016	1.5	26.8
222: <i>.gr..J.K_S[3.6][4.5]..</i>	1175	1.0	9.5	3373	1.3	13.5	7012	2.1	17.8
322: <i>.gri.J.K_S[3.6][4.5]..</i>	1123	1.0	8.5	3369	1.3	13.0	6976	2.2	16.2
332: <i>.gri.JHK_S[3.6][4.5]..</i>	1119	0.9	8.1	3368	1.2	12.4	6912	2.3	15.2
532: <i>ugrizJHK_S[3.6][4.5]..</i>	730	0.7	6.1	774	1.4	7.3

Table 6.1: Number of filters test results. For various filter combinations and clusters, the number of stars in the dataset with the necessary photometry are shown, as well as percent errors in derived primary and secondary masses. The ‘532’ filter combination is not possible for M37, as only *gri* optical photometry is available.

reduce the mass accuracy of the BINOCS code. For example, stars being matched to a model using all 12 possible filters should have better accuracy than a model that is only matched using 2 filters. While BINOCS mass uncertainty should go down as more filters are required, the number of stars with the required photometry will also drop, limiting the usefulness of the analysis. A balance must be struck between the number of available stars, and the average uncertainty in mass.

To test the accuracy of BINOCS mass determination, an input catalog similar to that created in §6.2 was used. By overestimating the observational uncertainties in the input catalog, the error in mass estimates will be similarly enhanced, providing generous upper bounds on the mass uncertainty of the observed data. Various filter combinations were tested, and the results are shown in table 6.1 for several clusters in the sample. The number of stars in each cluster with the required photometry are also shown in table 6.1.

Table 6.1 matches the assumed situation: full SED sampling, while producing the lowest mass uncertainties, is not practical given the data available for our clusters. The ‘532’ filter combination has vastly reduced star counts in M67 and M36, and would com-

plete exclude M37 from the analysis, as only *gri* optical photometry is available. For less-than-complete filter combinations, there is little difference in the number of stars available for the ‘332’, ‘322’, and ‘222’ filter combinations. The next jump in number of available stars occurs when the number of required near-IR filters drops below two. Along with the increase in the number of available stars for the ‘211’ filter combination, secondary mass uncertainties have risen by 25-75% above those for the ‘332’ filter combination.

The vast increase in secondary mass uncertainty eliminates the ‘211’ filter combination, and those with less filters. Since there is no appreciable change in the number of stars available between ‘222’ and ‘332’, the filter combination with the lowest mass uncertainty is selected as the best option. It is therefore required that 3 of 5 optical filters, all 3 near-IR filters, and 2 of the 4 mid-IR filters be matched between an observed star and a model.

6.4 Minimum Mass Ratio

It is often impossible to tell the difference between a single star and a low mass-ratio binary, due to the small fractional difference in flux. In order to not overestimate the binary fraction of a cluster, a *minimum mass ratio* is defined, as a function of primary mass. The minimum mass ratio is defined by the maximum of three criteria:

- **Lowest mass-ratio model:** For the PARSEC isochrones being used, the isochrone models have a minimum mass of $0.13 M_{\odot}$. This sets the minimum *possible* mass

ratio, which varies inversely with primary mass. For example, for half solar mass stars, the lowest mass ratio is $0.13/0.5 = 0.26$.

- **Synthetic best-fit mass ratio:** After each run of the BINOCS code on the cluster dataset, a fit against the full synthetic library is run, similar to that in §6.3. At the end of this run, some *known* binaries may be classified as single stars. Using the known mass ratios and primary masses of these incorrectly-classified systems, another condition on the minimum mass ratio can be defined. If the BINOCS code has trouble correctly classifying systems of a certain mass ratio, observational data with derived mass ratios below that value cannot be trusted.
- **Constant threshold:** Upon comparison to published RV studies, BINOCS results prove unreliable for stars with mass ratios < 0.3 (see §6.5). Even if the synthetic tests estimate a value less than this, the minimum threshold is set to 0.3.

Stars which are determined to be binaries with a mass ratio less than this minimum are reclassified as best-fit by a single model. In this case, the best-fit masses from the single-models-only fit (described in §3.3) are used.

Minimum mass ratios for M37 and M67 are shown in figures 6.3 and 6.4. For low primary mass, the minimum mass ratio tracks closely to the lowest mass ratio model, while the high mass region ($1.2 M_{\odot}$ for M67 and $2.5 M_{\odot}$ for M37) are dominated by degeneracies near the turn-off of the cluster. In between these regions, the minimum mass ratio hovers close to the floor of 0.3.

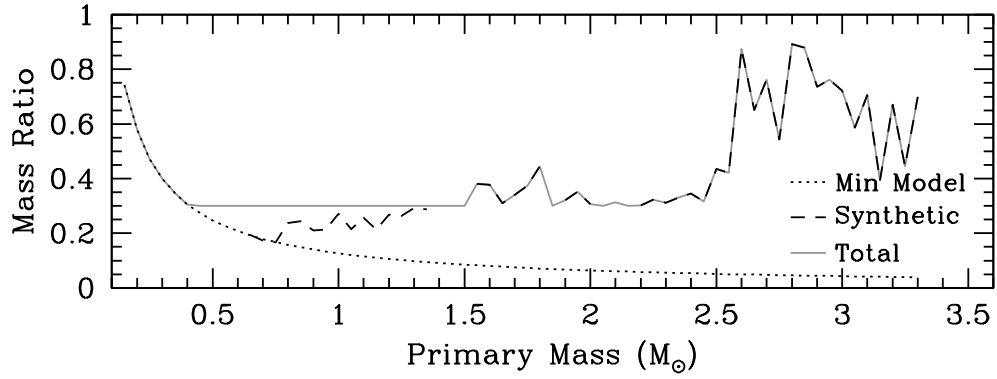


Figure 6.3: Minimum mass ratio as a function of primary mass for M37.

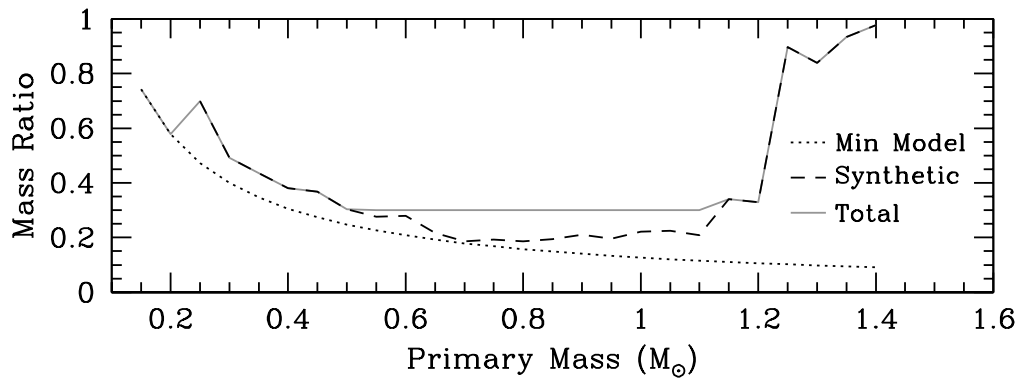


Figure 6.4: Minimum mass ratio as a function of primary mass for M67.

RV	BINOCS		
	Single	Binary	Non-Member
Single	113 (45%)	98 (39%)	40 (16%)
Binary	8 (18%)	31 (69%)	6 (13%)

Table 6.2: Confusion matrix between RV and BINOCS results for M35, as shown in figure 6.5.

RV	BINOCS		
	Single	Binary	Non-Member
Single	88 (59%)	36 (24%)	25 (17%)
Binary	6 (13%)	28 (58%)	14 (29%)

Table 6.3: Same as table 6.2, but for M67.

6.5 Comparison to RV

While internal checks of the BINOCS code have been completed, the results must be compared to an outside source for verification. As mentioned in §3.1.2, RV studies are the most detailed way to study binary systems in clusters, and the BINOCS code should produce compatible results. A comparison between these RV studies and the clusters’ BINOCS results are explored in the subsections below.

6.5.1 Binary Classification

Two clusters in the analysis set, M67 and M35, have published multi-epoch RV data: Mathieu et al. (1997) and Geller et al. (2010), respectively. A comparison of binary / single classifications between these RV studies and the BINOCS results is shown in figures 6.5 and 6.6, and summarized in tables 6.2 and 6.3.

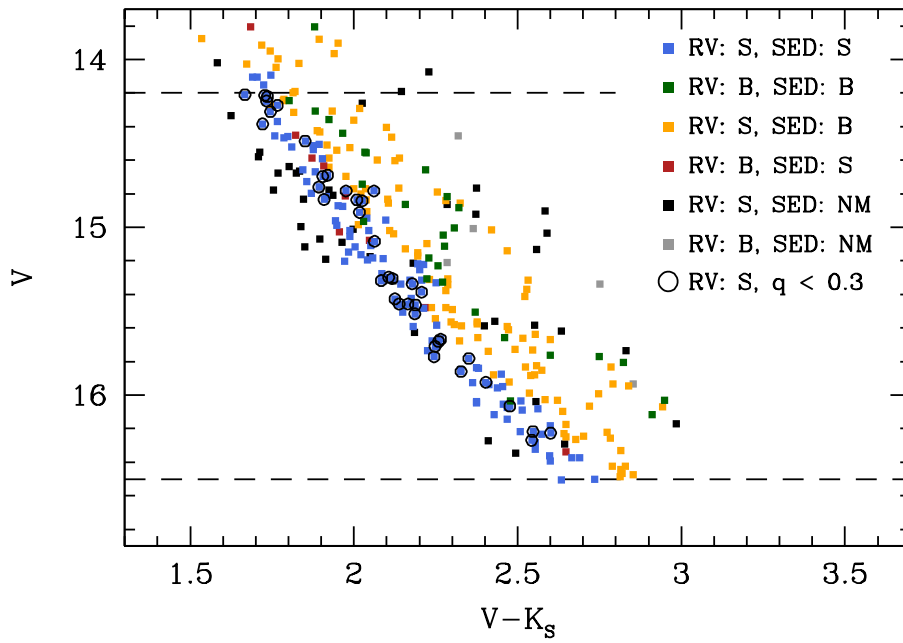


Figure 6.5: CMD comparison of RV and BINOCS SED-fitting results for M35. Stars considered in comparison are those within dashed line limits. Color of dot indicates which cell of table 6.2 star belongs to. Black circles indicate RV singles which were classified as BINOCS best-fit binaries with mass ratios < 0.3 .

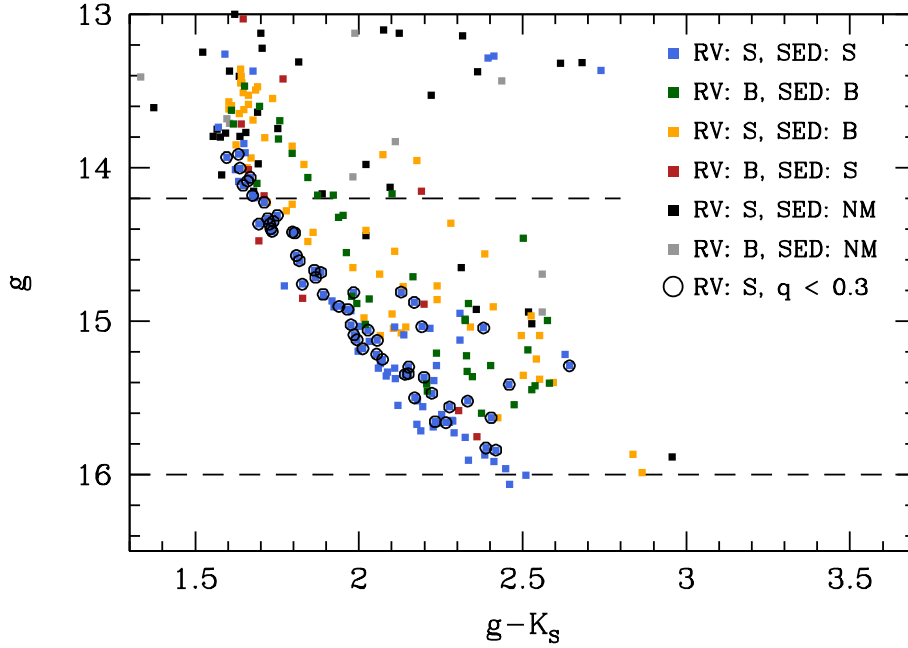


Figure 6.6: Same as figure 6.5, but for M67.

To avoid complications from the turn-off, and poor faint data in the RV studies, the comparison is limited to a specific magnitude range. For M35, stars with $14.2 \leq V \leq 16.5$ are considered, while stars with $14.2 \leq g \leq 16.0$ are considered for M67.

For stars classified as binaries by BINOCS, many are also classified as binaries by RV detection methods, with 58% overlap in M67, and 69% overlap in M35. The BINOCS code shows a lower match when classifying RV singles², with only 45% and 59% of RV singles being classified as singles by BINOCS in M35 and M67, respectively. The fact there is some mismatch between methods (and more mismatch for RV singles) is, in fact, expected:

- **Inclination:** Binary systems can form with any inclination with respect to Earth.

For binary systems with a high inclination angle, RV studies will not detect any

²The term “RV singles” is used to denote a system which does not show an appreciable velocity shift.

significant shifts in RV, and therefore classify the system as a single. BINOCS, on the other hand will have no trouble classifying these types of systems, as the flux increase can be detected regardless of inclination.

This is the most likely factor in the mismatch between RV and BINOCS classifications for RV singles. Many of these systems may be binary systems with high inclination, and cannot be expected to be detected using radial velocities.

- **Period Length:** Wide binary systems, with their long orbital periods, may not produce enough velocity shift over the lifetime of an RV study, and will therefore be classified as a single. Similar to inclination, this effect does not block the excess flux from the secondary star, and therefore the BINOCS code is insensitive.
- **Small Secondaries:** The BINOCS code requires that there is a significant flux difference between a single and binary system, necessitating the use of minimum mass ratios described above. For binaries with a low mass ratio, the flux addition from the secondary star may not be great enough to be picked up by the code. However, depending on inclination and orbital period, even small secondaries can produce appreciable velocity shifts, and be detected by RV surveys.

This scenario is the converse to the previous two points, and can account for the fact that the BINOCS code does not correctly classify binaries that can be classified by RV-based studies.

RV studies and the BINOCS code are complementary techniques, and show a significant amount of agreement between results. This agreement is improved greatly by capping

the minimum mass ratio at 0.3. For M67, 48 RV single stars were initially classified as binaries with $0.2 \leq q \leq 0.3$, which is between the synthetic minimum mass ratio and the hard floor that was introduced. Without this minimum mass ratio floor, BINOCS would only correctly classify 27% of RV singles in M67.

6.5.2 Mass Determination

While not a part of the analysis set due to the lack of deep near-IR photometry, the clusters NGC 188 and NGC 6819 have also been the subject of detailed RV studies (Geller et al. 2008, Hole et al. 2009, respectively). A comparison to the RV studies can be completed in the region where 2MASS photometry is available.

Of the 1046 stars studied in NGC 188, 13 were *double-lined* binaries. Further follow-up on these stars, published in Geller et al. (2009), characterized the orbits of these double-lined binaries, and produced accurate binary mass ratios (see §1.1.7.3 and (1.24)). Similarly, NGC 6819 stars were followed up in Milliman et al. (2014), and 15 double-lined binaries were detected. The RV-determined mass ratios are compared to those from BINOCS in figures 6.7 and 6.8.

There are several highly discrepant mass ratio determinations in NGC 188 and NGC 6819. Many of these double-lined systems lie near the turn-off of each cluster, where the single star main sequence and equal mass binary sequence overlap (as seen in the left hand panels of figures 6.7 and 6.8). In these regions, there are natural degeneracies, and the BINOCS code cannot accurately determine parameters. Stars marked by red circles

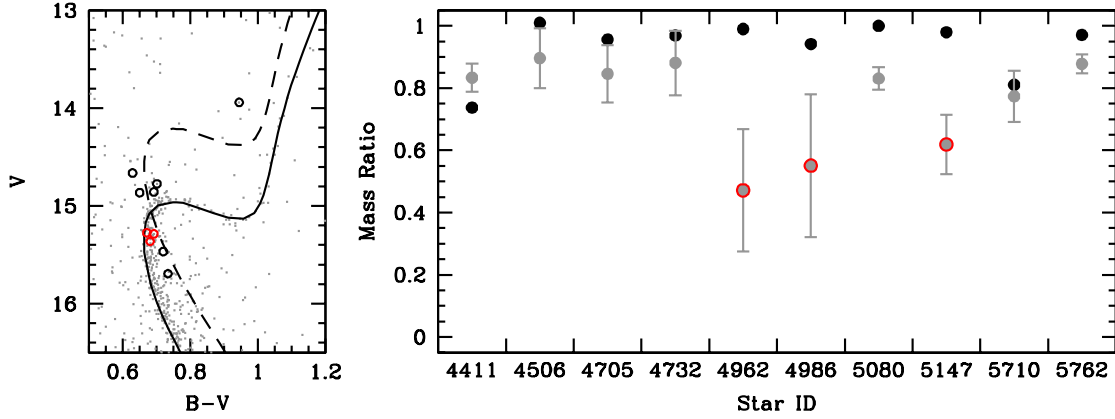


Figure 6.7: *Left*: NGC 188 CMD in $B - V$. Solid line is isochrone used to generate models for BINOCS fitting. Dashed line is equal-mass binary sequence. Black circles are double-lined binaries. *Right*: Comparison of RV mass ratios (black) from Geller et al. (2009) to BINOCS (grey) for NGC 188 double-lined binaries. Stars outlined in red are those complicated by degeneracies close to the turn-off.

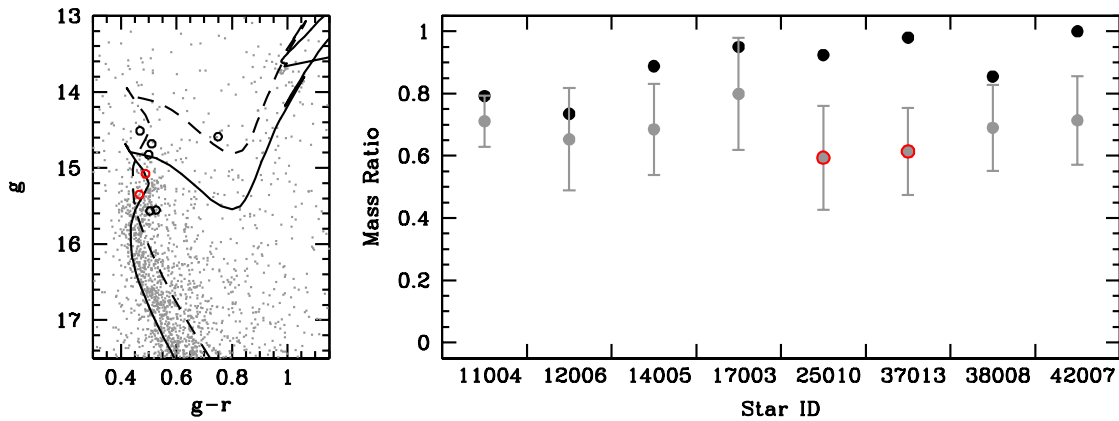


Figure 6.8: Same as figure 6.7 for NGC 6819. RV data from Milliman et al. (2014)

in figures 6.7 and 6.8 lie extremely close to these degeneracies and therefore exhibit large errors with respect to the RV results.

Ignoring those stars very close to the crossing of single star main sequence and equal mass binary sequence, there is close agreement between RV and BINOCS mass ratios. Including the quoted uncertainties in mass from BINOCS (uncertainties from the RV surveys are negligible), mass ratios largely agree to within 10%.

Combining this 10% mass ratio accuracy with the previous conclusion that BINOCS results are largely agreeing with RV multiplicity determinations, it is clear that the BINOCS code is producing accurate results that can be extrapolated to lower-mass stars.

Chapter 7

BINOCS Results

After validating the BINOCS code, it can begin to be applied to the clusters in the analysis set with the requisite photometry. The BINOCS code was run on each of the 8 clusters available for this analysis (see table 4.6), and the overall binary fraction was recorded. A table of clusters, their parameters, and the associated overall binary percentage is shown in table 7.1.

Cluster	Binary Fraction	Age (Gyr)	[Fe/H]	R_{gc} (kpc)	Number of Members	Mass Range (M_{\odot})
NGC 188	0.44	6.3	-0.02	9.54	405	0.80 - 1.14
NGC 1960 (M36)	0.66	0.03	...	9.81	941	0.65 - 6.46
NGC 2099 (M37)	0.48	0.35	+0.08	9.88	1632	0.32 - 3.21
NGC 2158	0.49	1.1	-0.23	13.56	266	1.00 - 1.98
NGC 2168 (M35)	0.61	0.13	-0.21	9.37	2258	0.55 - 3.19
NGC 2420	0.41	2.0	-0.23	10.81	748	0.35 - 1.63
NGC 2682 (M67)	0.44	3.5	+0.01	9.11	642	0.19 - 1.40
NGC 6791	0.39	8.0	+0.38	8.11	524	0.89 - 1.16

Table 7.1: Overall binary fractions for the 8 clusters considered in this analysis.

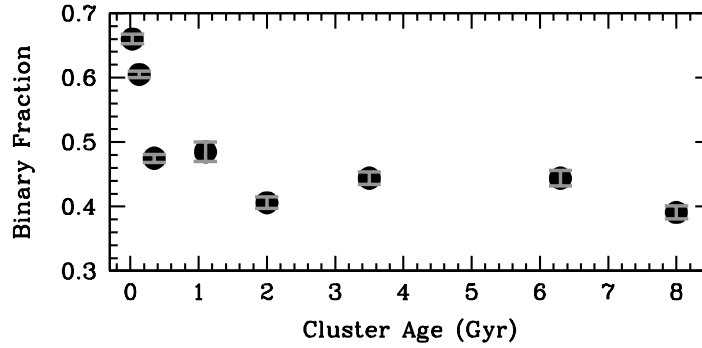


Figure 7.1: Overall cluster binary fraction, as a function of cluster age. Uncertainties are from Poisson counting statistics.

7.1 Binary Fraction Versus Age

One of the main science questions of this work is how the binary population of a cluster evolves over time. The trend of overall binary fraction with cluster age is shown in figure 7.1. Overall, there seems to be a decreasing trend with age. Gravitational interactions between stars can easily disrupt some binary systems, while creating binaries from two single stars is much less common. It appears the majority of binary disruption occurs quickly during the first 200 Myr of a cluster’s lifetime, after which the binary fraction becomes fairly constant.

After about 200 Myr, the binary fraction stabilizes to around 0.42, which is slightly higher than the measured binary percentage of 0.33 for field stars (Raghavan & McAlister 2009). This small difference may be attributable to the fact that during the strong gravitational interaction which could eject a cluster binary system into the field population, the binary system may also be disrupted. Without a better understanding of the ejection processes of binary systems, the overall binary fraction of cluster and field stars cannot be easily compared.

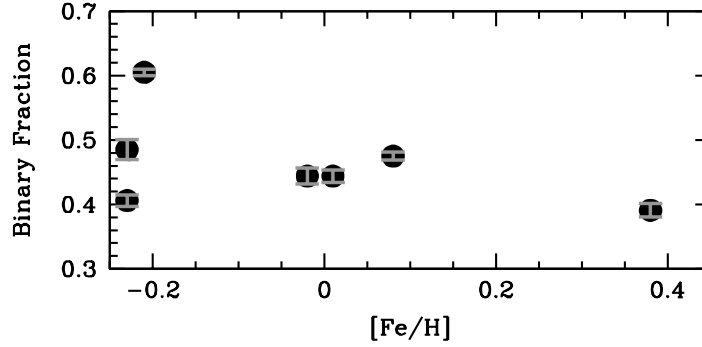


Figure 7.2: Overall cluster binary fraction, as a function of cluster $[\text{Fe}/\text{H}]$. Uncertainties are from Poisson counting statistics.

Completing an analysis such as the one in figure 7.1 using only RV surveys could take centuries to build up enough analysis clusters to produce any useful insights. Two-band analysis, though fast, is dominated by degeneracies, and is limited to small magnitude ranges across the main sequence. With new, deep photometric surveys becoming available (UKIDSS, LSST), more clusters could be added to the list with minimal effort using the BINOCS code. Generating the plot in figure 7.1 using hundreds of open clusters would yield significant insights into the true distribution of binary fractions.

7.2 Binary Fraction Versus Metallicity

It is not well-understood how differences in metallicity of a pre-cluster cloud may affect the formation of binary systems. The distribution of binary fractions as a function of metallicity is shown in figure 7.2. There are only 7 clusters shown in figure 7.2 due to the fact that M36 does not have a published metallicity value.

It is clear from figure 7.2 that any observed trend will be dominated by the contribution from NGC 6791, at $[\text{Fe}/\text{H}] = +0.38$. Without this metallicity outlier, there

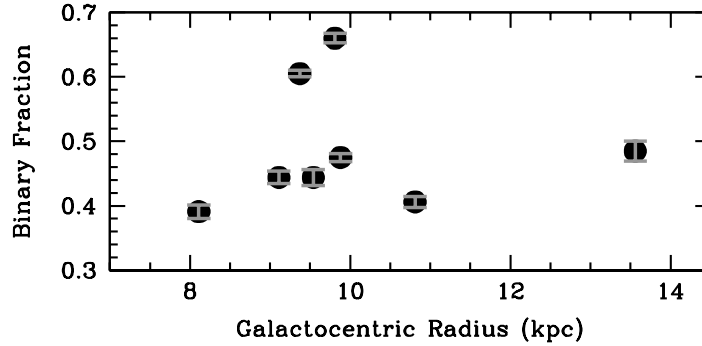


Figure 7.3: Overall cluster binary fraction, as a function of cluster R_{gc} . Uncertainties are from Poisson counting statistics.

is hardly any trend in binary fraction. The absence of a trend is still significant: the metallicity of a primordial cluster may have no effect on the binary population, at least on the aggregate level. This insight could be important for initial conditions of numerical simulations.

Similarly to the distribution with age, more data points can be added to this plot with minimal effort when new deep photometry becomes available. Filling in the remainder of the metallicity range will give more insight into whether a trend exists or not. Additionally, with a much larger number of clusters, binary fraction can be modeled as a function of both metallicity *and* age.

7.3 Binary Fraction Versus Galactocentric Radius

The above two comparisons have linked binary fraction to intrinsic cluster parameters, but clusters are not isolated systems, and the galactic environment plays a large part in cluster evolution. Clusters that are born near the center of the Galaxy experience a higher rate of tidal stripping events and other interactions which may alter the binary

population. Figure 7.3 shows the overall binary fraction of clusters as a function of galactocentric radius (R_{gc} ; the distance the cluster is from the center of the galaxy).

In figure 7.3, any observed trend is dominated by the two very young clusters, and thus high binary fraction, in the sample. Removing these two data points, a slight increasing trend with radius is observed. This would indicate that the gravitational shocking experienced at lower Galactic radii cause more binaries to be destroyed or ejected. However, NGC 2158, with a R_{gc} of 13.5, is a high leverage point; its removal would result in there being no trend in R_{gc} . Additionally, the most central cluster is NGC 6791, with an age of 8 Gyr, while NGC 2158 has an age of 1.1 Gyr, an age difference which may explain the trend without R_{gc} .

As with the metallicity comparison, more clusters are needed to fill in the gaps in R_{gc} , disentangle correlations with age, and determine whether a trend truly exists. A more complete figure 7.3 would allow the exploration of cluster-environment interactions, and would inform cluster simulations on the correct treatment of tidal stripping events and other gravitational collisions.

Now that the global trends in open cluster binary populations have been quantified, more detailed problems can be undertaken. Using the BINOCS results for 4 of the clusters with complete, deep photometry, a conflict in the understanding of internal cluster dynamics can be reconciled.

Chapter 8

Radial Migration of Binary Systems

8.1 Mass Segregation

When an interstellar gas cloud is shocked, and begins to collapse into an open cluster, there is no physical process which causes different regions to produce different types of stars. This means that there should be a uniform *number density* of a certain mass range of star throughout the primordial cluster. Star clusters are *pressure supported*, meaning that the further out the star is formed, the higher its total energy. As stars are randomly distributed without the cluster, this means that all ranges of stellar masses have the same velocity distribution.

Within the cluster, stars interact gravitationally, and energy is transferred. In any such gravitational “collision,” the total energy of the two-body system must be the same before and after the collision:

$$\frac{1}{2}m_1v_{1i}^2 + \frac{1}{2}m_2v_{2i}^2 = \frac{1}{2}m_1v_{1f}^2 + \frac{1}{2}m_2v_{2f}^2 \quad (8.1)$$

Here, the number subscripts refer to star 1 or star 2 in the collision, and subscripts i and f refer to initial and final states, respectively. Simplifying gives:

$$(v_{2f}^2 - v_{2i}^2) = -\frac{m_1}{m_2}(v_{1f}^2 - v_{1i}^2) \quad (8.2)$$

The increase in the square of the velocity of one star is proportional to the *decrease* in the square of the velocity for the other star, as energy is transferred between them. Additionally, the magnitude of the transfer is dependent upon the ratio of the masses of the two stars. The more massive star will always get less of a boost than a smaller star.

Over time, these preferential transfers lead to an equipartition of energy within the cluster. When the kinetic energy of all stars are uniform:

$$KE = \kappa = \frac{1}{2}mv^2 \rightarrow v = \sqrt{2\kappa/m} \quad (8.3)$$

Less massive stars will have higher velocities than more massive ones. Due to the pressure supported nature of the cluster, stars with lower velocities will be not be able to reach further radii from the cluster center, and will appear more centrally concentrated. This phenomenon, known as *mass segregation*, has been observed in many open clusters.

8.2 Binary Segregation

Binary systems are more massive, on average, than a single star, and should therefore experience mass segregation as well. This has been observationally confirmed for several globular and open clusters (e.g., Geller & Mathieu 2012, Milone et al. 2012). Similar

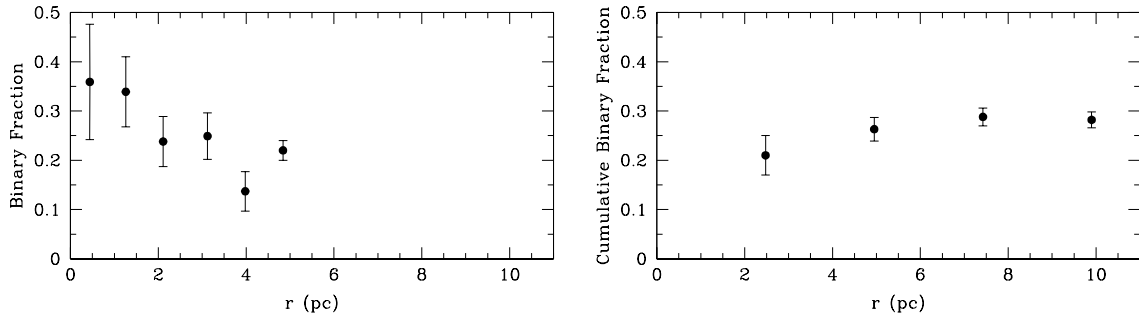


Figure 8.1: *Left:* Adaptation of figure 4 in Elson et al. (1998), which shows mass segregation within the cluster. *Right:* Adaptation of figure 3 in de Grijs et al. (2013), showing the inverse trend. Note that de Grijs et al.’s results are cumulative binary fractions.

analyses, using the two-band detection method (§3.1.1), have been conducted on the young (15 – 30 Myr), massive cluster NGC 1818, located in the Large Magellanic Cloud (LMC), producing conflicting results.

The first analysis of NGC 1818 binaries, published in Elson et al. (1998), showed a binary fraction that decreases with radius, consistent with the cluster undergoing mass segregation even within its short lifespan. Later, however, in de Grijs et al. (2013) (and improved upon in Li et al. (2013)), detected binaries produced a completely opposite results: a binary fraction that *increased* with radius; the opposite of mass segregation. Reproduced plots from both papers are shown in figure 8.1.

Following the release of these conflicting observations, N-Body simulations of a young, massive cluster were published in Geller et al. (2013). Geller et al. found that the radial binary distributions of clusters are not always mass segregated, but instead evolve through a series of qualitatively different phases, best illustrated by figure 2 of their paper, reproduced here in figure 8.2.

Two of the three “axes” of figure 8.2, radius and time, are quoted as multiples of intrinsic cluster parameters: the half mass relaxation time ($t_{rh}(0)$), and initial half-mass

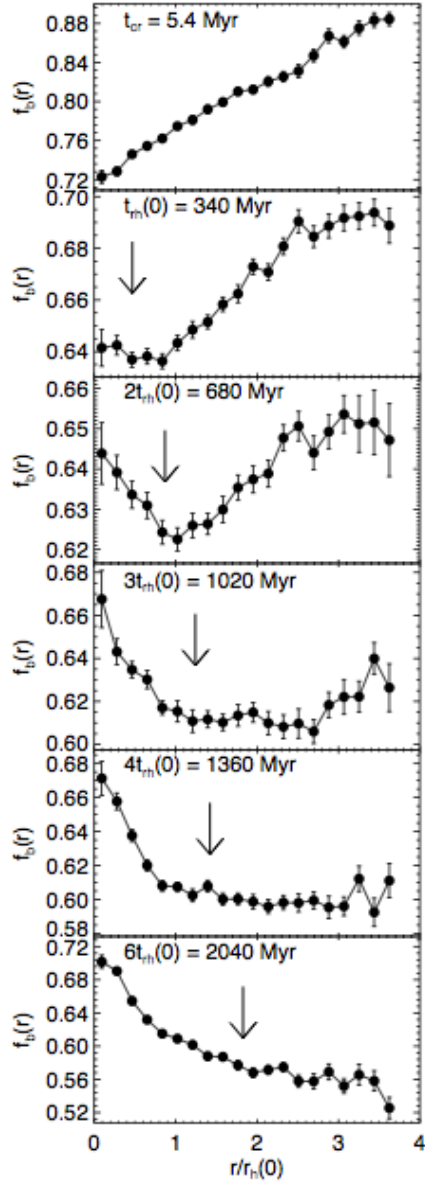


Figure 8.2: Reproduction of figure 2 in Geller et al. (2013), showing binary fraction (f_b) as a function of radius for various cluster ages. $t_{rh}(0)$ is the initial half mass relaxation time of the cluster, and $r_h(0)$ is the initial half-mass radius.

radius $r_h(0)$. The relaxation time of a cluster is the time it takes for a single star in the cluster to be significantly perturbed by the other stars in the cluster, most often being defined by a significant change in the star's initial velocity. The half-mass radius is more straightforward: it is the radius within which half the cluster's mass is contained.

$t_{rh}(0)$ and $r_h(0)$ are non-observable quantities, and therefore results from the open clusters in the analysis set cannot be translated onto the same scale. The cluster ages shown in figure 8.2 are valid only for a cluster of NGC 1818's mass; less massive clusters will have different relaxation timescales. However, each panel of figure 8.2 represents a qualitatively different binary distribution, and illustrates the dynamical processes happening within the evolving cluster:

- Initially the cluster binary fraction is isotropic, as there is no physical reason to create a higher density of binaries in a particular area of the cluster.
- There are two “dynamical” types of binaries: hard and soft. Hard binaries are systems where the internal energy of the binary orbit is much greater than the kinetic energy of the system through the cluster; in other words, they have a close orbit. Soft binaries are the opposite: with large orbits, the internal energy of the system is much less than the motion of the system through the cluster. Hard and soft binaries react very differently to interactions: hard binaries tighten their orbits and become “harder,” while soft binaries lose internal energy and become “softer” (Heggie 1975).

Due to the higher density within the core of the cluster, there is a higher frequency of interactions. Within a short amount of time (5.4 Myr in the simulations), nearly

all the soft binaries within the core of the cluster have been disrupted, while those on the edges of the cluster may still be intact. This forms the “reverse mass segregation” distribution that was observed by de Grijs et al..

- This same distribution persists until around $1t_{rh}(0)$, when enough interactions have happened in the core of the cluster to begin the mass segregation process. The large arrow in the panels of figure 8.2 indicates the interface between regions within, which have undergone mass segregation, and those which are still unsegregated.
- Around $6t_{rh}(0)$, the entire cluster has become mass segregated, and the familiar binary ratio distribution is revealed.

The de Grijs et al. (2013) results indicate a cluster whose age is $< 1t_{th}(0)$, which is supported by the cluster’s 15 – 30 Myr age and Geller et al.’s N-Body simulation results. The question still remains: how did two independent studies arrive to different results about the same cluster? We will use BINOCS results from our open cluster analysis set to produce similar binary radial profiles for a range of cluster ages. Using an age range of 30 Myr to 3.5 Gyr, the discrepancy between NGC 1818 studies can be reconciled.

8.3 BINOCS Radial Profiles

The BINOCS code was run on the 4 clusters (M36, M35, M37, and M67) which have complete wide-field, deep photometry, and the resulting binary / single classifications were used to create binary radial distributions of each open cluster. To do this, stars were first sorted according to their distance from the cluster center. Then, stars were

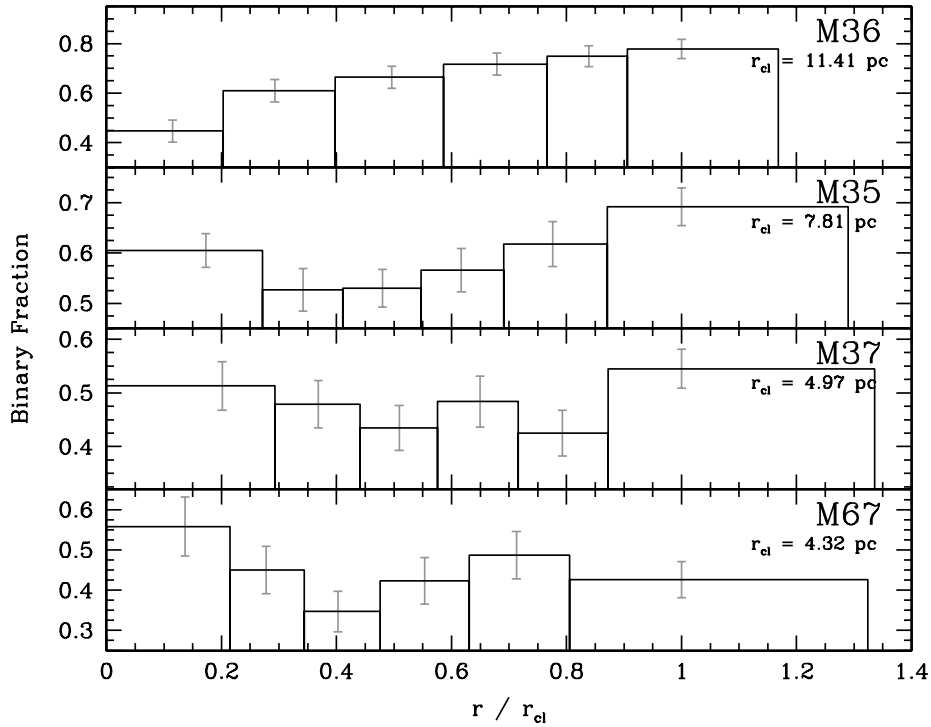


Figure 8.3: Binary radial distributions for all clusters in the analysis set. Radii have been normalized by the r_{cl} values listed in each plot.

separated into six bins, and the binary fraction and average radius from the cluster center for this bin were calculated.

To account for uncertainties in multiplicity determinations, the BINOCS code was run 10 times for each cluster, and an average binary fraction for each bin was determined using all 10 runs. An uncertainty on the binary fraction was computed using the standard deviation between the results of all 10 runs, and was added to the baseline uncertainty due to poisson error. The uncertainties in the BINOCS radial profiles are mostly set by the relatively small number of stars in each bin, as opposed to the simulation profiles in figure 8.2, which involved tens of thousands of sources.

Spectral Class	Mass Range (M_{\odot})	M_V Range
A	1.6 - 2.5	1 - 4
F	1.1 - 1.6	4 - 5
G	0.8 - 1.1	5 - 6
K	0.2 - 0.8	6 - 8

Table 8.1: Spectral class mass ranges considered in this work.

Radial profiles for the 4 clusters in this analysis are shown in figure 8.3. To account for the variation in cluster size and mass, radii are normalized to put all clusters on a common system. The progression of radial distributions with cluster age in figure 8.3 follows qualitatively with the results of the N-Body simulation in figure 8.2. Young clusters, such as M36 and M35, have mostly increasing binary fraction with radius, while the old cluster M67 has a general decreasing binary fraction with radius.

Both Elson et al. (1998) and de Grijs et al. (2013) employed two-band detection, which is only effective within a small mass window in NGC 1818. In their paper, de Grijs et al. admit that outside of this small mass region “...the CMD is too steep to easily disentangle single from binary stars and blends. In addition, toward fainter magnitudes, photometric errors start to dominate any potential physical differences...” With BINOCs, nearly the entire mass range of the cluster can be explored, which can lead to useful insights. For each cluster, binary radial distributions were computed for each of the classical *stellar spectral classes*. Mass ranges for each of the spectral classes considered are shown in table 8.1.

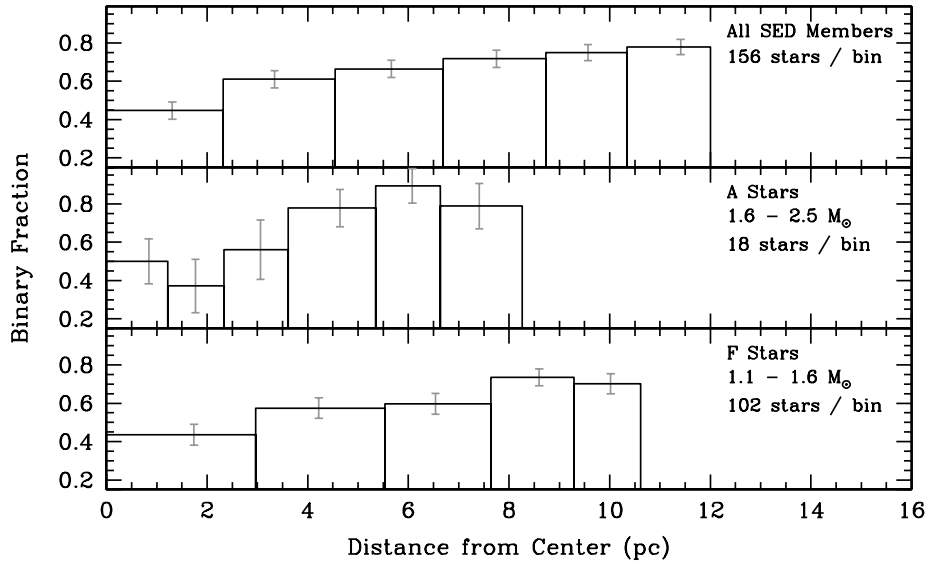


Figure 8.4: Binary radial distributions for various spectral classes in M36.

8.3.1 NGC 1960 (M36)

Binary radial distributions for young open cluster M36 (30 Myr), as well as for individual spectral classes within the cluster, are shown in figure 8.4. The overall binary distribution of M36, as well as that for A- and F-class stars, matches closely to that of a young, un-segregated cluster. Except for the most centrally located bin, binary percentage slowly increases with radius. Overall, M36 appears to validate the results of de Grijs et al. (2013), with young clusters exhibiting an increasing binary fraction with radius.

8.3.2 NGC 2168 (M35)

The cluster M35 is slightly older than M36, and the radial distributions shown in figure 8.5 follow this fact. While a majority of the distributions still have increasing binary fraction with radius, there is a clear central area where stars have become mass segregated, with

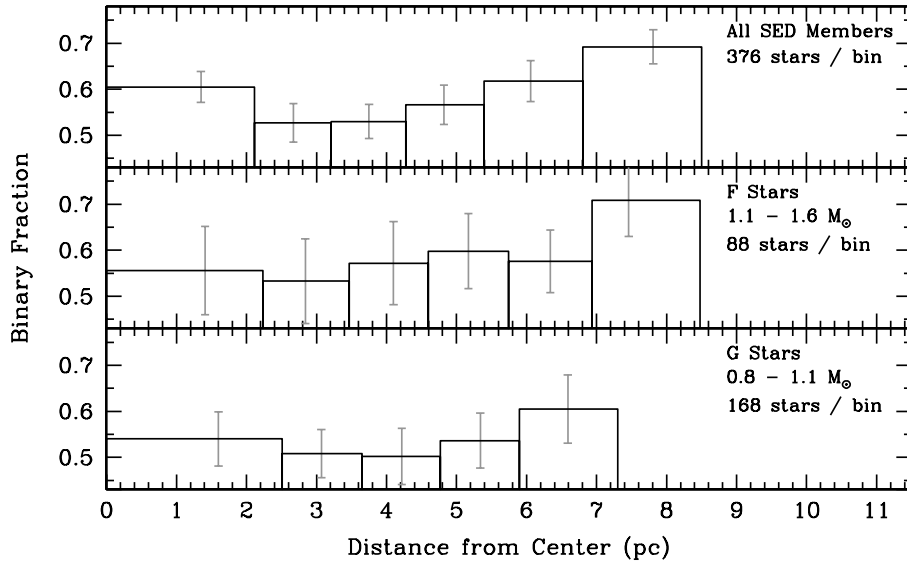


Figure 8.5: Binary radial distributions for various spectral classes in M35.

a much more prominent peak at the center than in M36. As in M36, the overall binary distribution matches very closely to the single mass range distributions.

8.3.3 NGC 2099 (M37)

Binary distributions for M37, which is even more evolved than M36 and M35, are shown in figure 8.6. Kalirai et al. (2001) determined the relaxation time of M37 to be ~ 300 Myr, giving M37 an age of $2.33 t_{rh}(0)$, which qualitatively matches with the overall M37 distribution as determined by BINOCs. The individual mass ranges, however, show varying distributions.

The A-class star distribution matches more closely to a $3 t_{rh}(0)$ distribution, with the central concentration of binaries higher than that on the edge. The F-class star distribution is slightly younger, matching a $2 t_{rh}(0)$ distribution, with the edge binary frequency matching that of the central region. Lastly, the G-class star distribution matches much

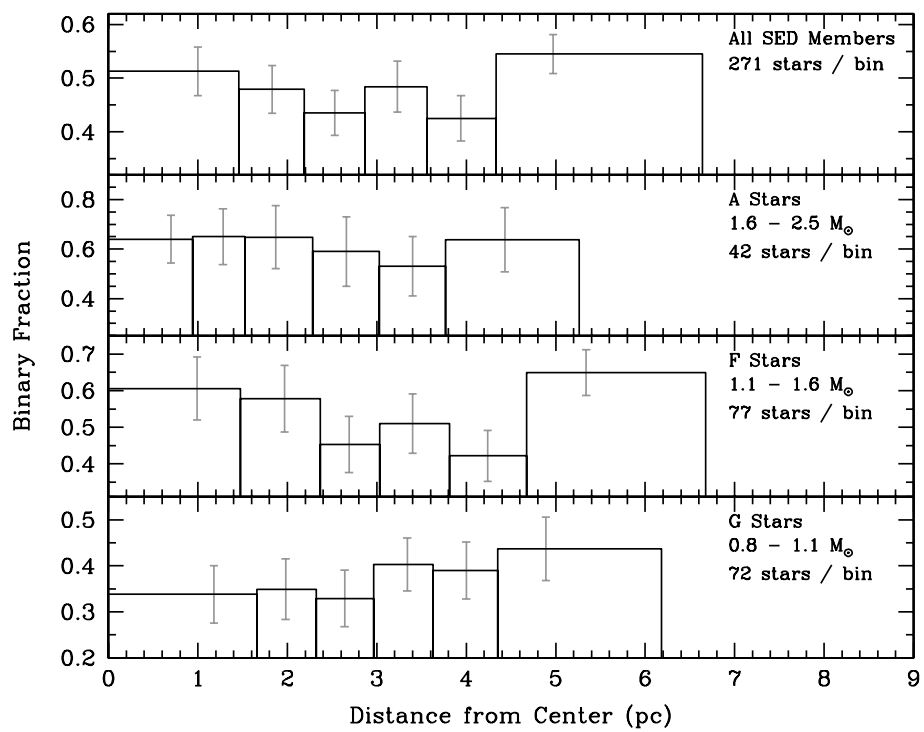


Figure 8.6: Binary radial distributions for various spectral classes in M37.

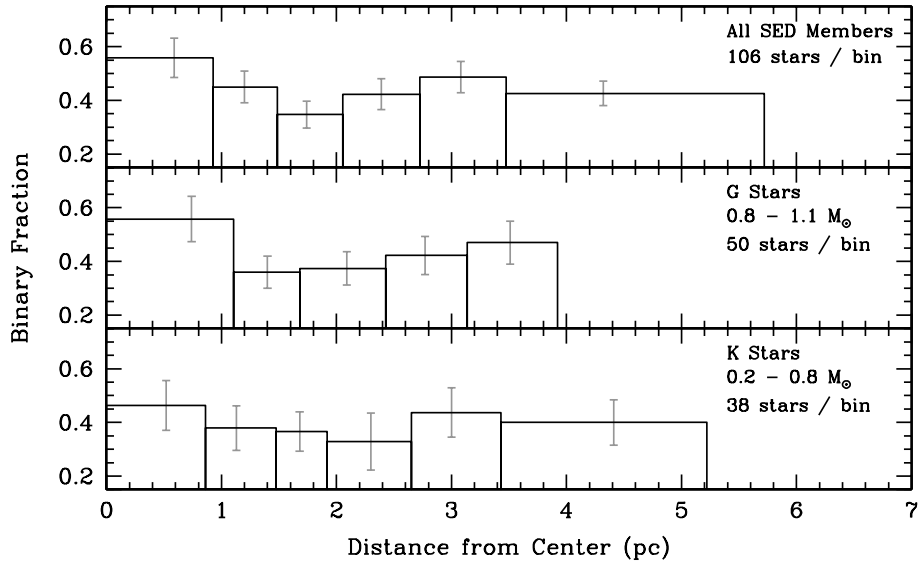


Figure 8.7: Binary radial distributions for various spectral classes in M67.

more closely to the young distributions seen in M36 and M35. A majority of the G-class star distribution has increasing binary frequency with radius.

8.3.4 M67

After a lifetime of 3.5 Gyr, all of M67’s stars should be mass segregated, but the radial distribution plots in figure 8.7 do not mirror that fact. F and K stars show general decreasing trends with radius, but G stars show a distribution more similar to that of M35. As described in §1.1.6, gravitational “collisions” with other large masses can strip away stars on the edges of open clusters. It appears that after enough tidal stripping events, the equilibrium which causes mass segregation has been completely disrupted. While M67 anchors the old edge of the analysis sample, it has been too compromised from its original form to yield any insights into binary migration.

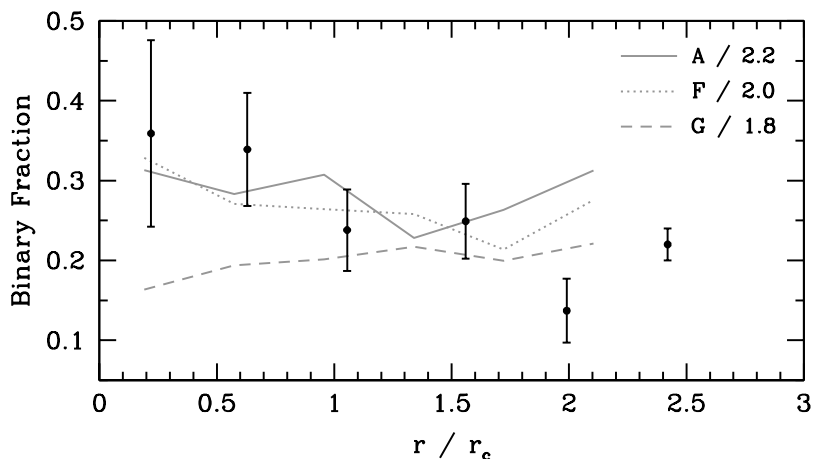


Figure 8.8: Comparison of BINOCS-derived M37 binary distributions (grey) to that of figure 4 of Elson et al. (1998) for NGC 1818 (black). NGC 1818 binary distribution is more evolved than any of the M37 populations.

8.4 Comparison to NGC 1818

The new BINOCS binary radial distributions can be used to reconcile the two discrepant NGC 1818 publications. The individual A-, F- and G-class star distributions from M37 are compared to the results of Elson et al. (1998) and de Grijs et al. (2013) in figures 8.8 and 8.9. To inter-compare the results from two clusters with different sizes, the x-axes have been scaled to multiples of cluster’s core radius: 2 pc for NGC 1818, and 2.3 pc for M37 (Kalirai et al. 2001). Similarly, the overall binary percentages are different between the clusters, and necessitates scaling along the y-axis. This is done in an arbitrary way, and the scaling factors are indicated in each plot’s legend.

In addition to scaling, the plots for NGC 1818 were not sampled in the same way as those in §8.3. To match Elson et al.’s results, binary percentages were re-computed for M37 in 0.88 pc-wide bins to match the data from the original figure. Similarly, *cumulative*

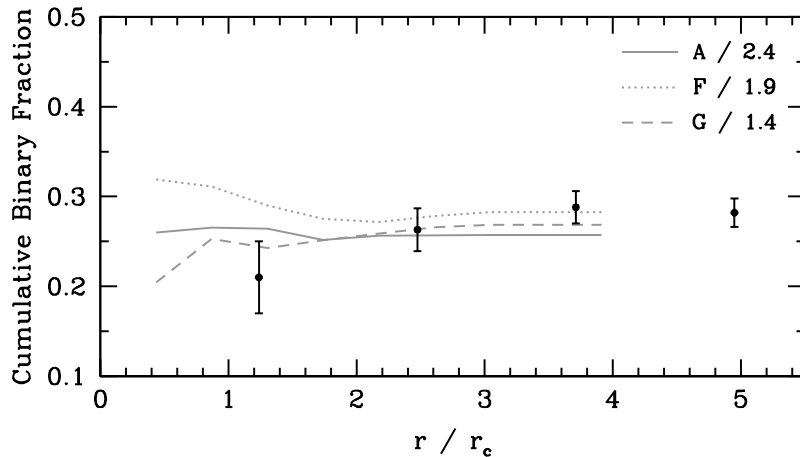


Figure 8.9: Comparison of BINOCS-derived M37 binary distributions (grey) to that of figure 3 of de Grijs et al. (2013) for NGC 1818 (black). NGC 1818 distribution decreases towards the center, which is only modeled by G-class stars in M37.

binary percentages were computed for M37 in steps of 1 pc to match the original figure in de Grijs et al. (2013).

In figure 8.8, while none of the M37 distributions match exactly, the A- and F-class star distributions seem to have the right shape. Additionally, looking at figure 8.2, the barrier between inner regions, where binaries are mass segregated, and outer regions where they are not, moves outward with time. It would appear that the NGC 1818 stars studied by Elson et al. (1998) are “older” than those in M37. Importantly, however, the Elson et al. binary distribution does not match M37’s G-class star distribution.

Oppositely, de Grijs et al.’s binary distribution *does* match M37’s G-class star distribution in figure 8.9, but not the distribution of A- or F-class stars. While all three distributions match the outer parts of the cluster (where the cumulative fraction is nearly constant), the dip in the inner regions is only reproduced M37’s G-class stars.

The results of Elson et al. (1998) and de Grijs et al. (2013) indicate that NGC 1818 is non-uniform, but the above results show NGC 1818 is not unique. If only A-class stars were studied in M37, one may conclude that the cluster has some mass segregation, whereas if only G-class stars were studied, the conclusion would be that there is no cluster mass segregation at all.

8.5 Discussion

The M37 results illustrate a critical point: for a cluster where all stars have a common *chronological* age, each mass range may have a different *dynamical* age. This is not unexpected, as the gravitational interaction cross-section should increase with increasing stellar mass. More massive stars should therefore experience a higher frequency of interactions, leading to quicker energy transfer and mass segregation. With M37 as a guide, NGC 1818's results need not conflict: the $2 - 5.5 M_{\odot}$ stars studied by Elson et al. may have had enough time in NGC 1818's ~ 30 Myr lifespan to have become completely mass segregated, while the $1.3 - 1.6 M_{\odot}$ stars analyzed by de Grijs et al. have not.

While clusters are often treated as uniform objects, it is obvious from this analysis that ensemble properties cannot always be assumed. Binary migration, and perhaps mass segregation for single stars as well, seems to happen on varying timescales depending on mass. Recent N-body simulations support this conclusion, and predict similar trends in radial distributions as a function of mass (Geller et al. 2015).

Chapter 9

Summary & Future Work

The BINOCS method is a significant improvement over current binary detection techniques; requiring an order of magnitude less time, generating mass estimates on an order of magnitude more stars, and enabling quantitative exploration of faint binary systems, which are unreachable by RV studies. Table 9.1 denotes the number of stars classified in RV surveys as compared to those for BINOCS . Only double-lined binary systems will have mass estimates, meaning only a handful of systems in all 4 clusters can be used for N-body simulation inputs. The BINOCS routine, on the other hand, provides mass estimates on more than an order of magnitude more binaries in each cluster, providing the statistics necessary for N-body inputs.

Cluster	RV Members	RV Binaries	Double-Lined	BINOCS Members	BINOCS Binaries
NGC 188	473	78	15	405	180
NGC 2168	360	136	24	258	1366
NGC 2682	524	88	4	642	285
NGC 6819	479	41	15	541	371

Table 9.1: Comparison of number of stars considered in RV studies to number of stars classified in BINOCS . Only double-lined RV binaries will have mass information. The BINOCS routine provides mass estimates on an order of magnitude or more stars than RV surveys.

The BINOCS method allows for robust, quick binary classification that will become especially powerful as new all-sky surveys are released. The BINOCS code was tested to ensure it produced reasonable results for binary detection and mass determination, when compared to previously-published studies based on multi-decade RV work.

Overall binary fractions were computed quickly using BINOCS for several clusters in the targeted dataset. Trends were quantified in binary fraction with respect to age, metallicity and Galactic radius. BINOCS results were then applied to the previously conflicted studies of binary star distributions in NGC 1818, and were used to show that different massed systems evolve dynamically with different timescales, which has only recently been confirmed by N-body simulations.

In addition, and necessary to developing these findings, this project has built a comprehensive photometric library on four open clusters, and added deep, wide-field near-IR photometry to four others. This additional open cluster photometry will enable a wide variety of explorations from the astronomical community on these fundamental objects.

Future work for the BINOCS project focuses on applying the insights gleaned from the BINOCS results back to simulation:

- **Modeling binary radial distributions after external collisions.** In §8.3, binary radial distributions for the young clusters M36, M35 and M37 matched nicely to the N-Body simulations results from Geller et al. (2013). Older clusters, such as NGC 2420 and M67 do not match perfectly to the simulation results, and the difference was posited to be due to external forces which disrupt the outer regions of the cluster. The simulations in Geller et al. (2013) model the galaxy as

a single point source, ignoring tidal effect from spiral arms or other large masses. Rerunning the simulations to include these tidal events may more accurately model observed old open clusters.

- **Running simulations with accurate starting binary populations.** The assumption of a uniform mass ratio distribution in numerical simulations such as Moyano Loyola & Hurley (2013) is not representative of realistic clusters. The BINOCS code can provide empirical initial conditions from the young clusters in the analysis sample: M36, M35, and M37. Recomputing ejection frequencies and related variables for clusters with the observed mass ratio distribution may produce different conclusions.
- **Benchmarking simulations using evolved open clusters.** BINOCS data for evolved clusters, such as NGC 2420 and M67 could be compared to N-Body simulations to check accuracy. Running simulations with realistic starting conditions for these clusters should be able to match the observed binary population. By applying BINOCS to clusters with various ages and metallicities, N-Body simulations of cluster evolution can be rigorously tested.
- **Expanding global binary fraction trend datasets.** The 16 clusters in the targeting sample were chosen to overlap with specific high-impact, publicly-available datasets to facilitate detailed binary population studies, like the one in §8. However, the BINOCS code can quickly generate global binary fractions for nearly any cluster which has complete photometry, and as mentioned in §7, the trends in binary fraction with metallicity and Galactic radius would be vastly enhanced by this

expansion. The LSST survey will provide all-sky coverage in optical wavelengths, providing deep optical data for any cluster. Combined with 2MASS and WISE, any nearby open cluster could be a candidate for inclusion in the analysis of §7.

Appendix A

Empirical Ridgelines

K	$U - V$	$B - V$	$V - R$	$V - I$	$V - K_S$	$J - K_S$	$H - K_S$	$V - [3.6]$	$V - [4.5]$
10.0	0.20	0.10	0.10	0.24	0.50	0.05	0.02	0.50	0.50
10.2	0.18	0.11	0.10	0.24	0.50	0.05	0.02	0.50	0.50
10.4	0.16	0.12	0.10	0.24	0.50	0.05	0.03	0.55	0.51
10.6	0.16	0.13	0.11	0.24	0.52	0.06	0.04	0.60	0.56
10.8	0.20	0.15	0.12	0.24	0.56	0.07	0.05	0.60	0.60
11.0	0.24	0.17	0.13	0.26	0.60	0.09	0.05	0.64	0.64
11.2	0.30	0.20	0.14	0.31	0.70	0.12	0.06	0.72	0.70
11.4	0.47	0.26	0.20	0.40	0.80	0.14	0.06	0.78	0.73
11.6	0.50	0.34	0.24	0.48	0.94	0.18	0.06	0.94	0.94
11.8	0.53	0.44	0.30	0.60	1.20	0.22	0.07	1.22	1.16
12.0	0.55	0.54	0.38	0.73	1.50	0.28	0.08	1.48	1.53
12.2	0.57	0.60	0.40	0.77	1.63	0.33	0.08	1.63	1.70
12.4	0.64	0.66	0.42	0.82	1.71	0.37	0.08	1.82	1.78
12.6	0.70	0.72	0.44	0.90	1.80	0.41	0.08	1.93	1.90
12.8	0.80	0.76	0.47	0.96	1.94	0.43	0.09	2.04	2.01
13.0	0.92	0.81	0.50	1.00	2.06	0.45	0.09	2.15	2.15
13.2	1.06	0.86	0.52	1.03	2.15	0.49	0.10	2.28	2.23
13.4	1.24	0.92	0.56	1.06	2.29	0.56	0.11	2.38	2.30
13.6	1.45	1.00	0.60	1.15	2.46	0.62	0.13	2.53	2.55
13.8	1.70	1.13	0.64	1.27	2.79	0.67	0.15	2.84	2.73
14.0	2.20	1.25	0.74	1.40	3.08	0.76	0.17	3.14	3.06
14.2		1.34	0.82	1.52	3.37	0.85	0.20	3.44	3.40
14.4		1.45	0.90	1.68	3.71	0.92	0.22	3.80	3.70
14.6		1.55	1.00	1.87	4.00	0.95	0.26	4.05	4.06
14.8						0.98	0.29		
15.0						1.00	0.32		
15.2						1.01	0.34		
15.4						1.01	0.35		
15.6						1.02	0.35		
15.8						1.01	0.35		
16.0						1.00	0.35		
16.2						1.00	0.35		
16.4						1.00	0.35		

Table A.1: Empirical ridgelines for M36.

V	$U - V$	$B - V$	$V - R$	$V - I$	$V - K_S$	$J - K_S$	$H - K_S$	$V - [3.6]$	$V - [4.5]$
11.0	-0.35		0.06	0.16	0.25	0.03	-0.04	0.34	0.30
11.2	-0.30		0.06	0.16	0.27	0.03	-0.04	0.34	0.30
11.4	-0.22	0.09	0.06	0.17	0.30	0.04	-0.04	0.38	0.32
11.6	-0.15	0.10	0.06	0.17	0.32	0.05	-0.03	0.40	0.34
11.8	-0.04	0.11	0.07	0.18	0.36	0.05	-0.03	0.45	0.38
12.0	0.05	0.13	0.07	0.19	0.40	0.06	-0.02	0.48	0.44
12.2	0.19	0.15	0.07	0.22	0.44	0.06	-0.02	0.50	0.52
12.4	0.25	0.18	0.07	0.23	0.50	0.07	-0.01	0.54	0.62
12.6	0.28	0.20	0.09	0.24	0.57	0.07	-0.01	0.60	0.70
12.8	0.38	0.23	0.11	0.27	0.63	0.09	-0.01	0.68	0.76
13.0	0.45	0.26	0.14	0.33	0.72	0.11	0.01	0.80	0.84
13.2	0.55	0.31	0.17	0.38	0.85	0.15	0.01	0.92	0.94
13.4	0.60	0.38	0.20	0.44	1.00	0.19	0.01	1.04	1.03
13.6	0.64	0.42	0.24	0.49	1.12	0.23	0.02	1.16	1.15
13.8	0.69	0.46	0.27	0.56	1.23	0.26	0.02	1.30	1.30
14.0	0.71	0.52	0.30	0.63	1.40	0.30	0.03	1.49	1.48
14.2	0.73	0.57	0.34	0.70	1.50	0.34	0.03	1.63	1.60
14.4	0.75	0.60	0.37	0.75	1.60	0.37	0.04	1.72	1.70
14.6	0.76	0.65	0.39	0.79	1.68	0.39	0.05	1.84	1.78
14.8	0.78	0.68	0.41	0.83	1.80	0.42	0.05	1.92	1.85
15.0	0.83	0.72	0.43	0.86	1.90	0.46	0.06	2.01	1.95
15.2	0.88	0.74	0.46	0.91	2.00	0.50	0.07	2.09	2.10
15.4	0.93	0.78	0.49	0.94	2.07	0.53	0.08	2.17	2.20
15.6	1.05	0.83	0.51	1.00	2.15	0.56	0.09	2.25	2.37
15.8	1.18	0.87	0.53	1.05	2.24	0.59	0.10	2.40	2.50
16.0	1.26	0.92	0.56	1.09	2.33	0.61	0.11	2.60	2.70
16.2	1.40	0.96	0.58	1.18	2.42	0.64	0.12	2.82	2.83
16.4	1.50	1.01	0.60	1.24	2.53	0.67	0.13	3.00	2.97
16.6	1.57	1.07	0.62	1.28	2.66	0.68	0.14	3.15	3.05
16.8	1.64	1.10		1.31	2.80	0.70	0.15	3.25	3.12
17.0	1.76	1.15		1.35	2.90	0.73	0.16	3.30	3.22
17.2	1.88	1.20		1.42	3.03	0.77	0.17	3.45	3.30
17.4	2.00	1.25		1.48	3.17	0.81	0.18	3.60	3.40
17.6	2.18	1.28		1.57	3.32	0.86	0.19	3.65	3.50
17.8	2.34	1.31		1.60	3.50	0.89	0.20	3.75	3.60
18.0	2.45	1.38		1.67	3.70	0.93	0.21	3.83	3.73
18.2		1.44		1.73	3.85	0.96	0.21	3.97	3.95
18.4		1.50		1.84	4.00	0.99	0.22	4.10	4.10
18.6		1.54		1.93	4.14	1.02	0.23	4.35	4.30
18.8		1.60		2.04	4.30	1.02	0.24	4.48	4.44
19.0		1.65		2.16	4.40	1.01	0.25	4.60	4.65

Table A.2: Empirical ridgelines for M35.

r	$g-r$	$g-i$	$g-K_S$	$J-K_S$	$H-K_S$	$g-[3.6]$	$g-[4.5]$
12.1	0.02	0.10	1.00	0.15	0.07	1.03	1.04
12.3	0.02	0.07	0.97	0.15	0.07	1.02	1.00
12.5	0.03	0.08	0.95	0.15	0.07	1.01	0.96
12.7	0.05	0.10	0.95	0.15	0.07	1.01	0.98
12.9	0.08	0.14	1.00	0.16	0.07	1.05	1.04
13.1	0.12	0.18	1.10	0.17	0.08	1.09	1.14
13.3	0.15	0.23	1.20	0.19	0.08	1.20	1.24
13.5	0.17	0.28	1.28	0.21	0.08	1.30	1.35
13.7	0.20	0.34	1.40	0.23	0.08	1.43	1.48
13.9	0.26	0.40	1.52	0.25	0.08	1.55	1.60
14.1	0.30	0.47	1.64	0.27	0.08	1.68	1.72
14.3	0.38	0.55	1.80	0.29	0.08	1.85	1.88
14.5	0.42	0.62	1.90	0.31	0.08	2.00	2.00
14.7	0.47	0.70	2.03	0.33	0.08	2.12	2.10
14.9	0.50	0.75	2.13	0.35	0.08	2.22	2.20
15.1	0.52	0.80	2.18	0.37	0.09	2.30	2.30
15.3	0.54	0.83	2.27	0.39	0.09	2.38	2.40
15.5	0.58	0.87	2.35	0.41	0.09	2.45	2.48
15.7	0.62	0.92	2.44	0.43	0.10	2.55	2.55
15.9	0.65	0.97	2.55	0.46	0.10	2.63	2.63
16.1	0.70	1.02	2.64	0.48	0.11	2.72	2.75
16.3	0.74	1.08	2.76	0.51	0.12	2.80	2.85
16.5	0.78	1.15	2.85	0.53	0.12	2.93	2.97
16.7	0.82	1.22	2.93	0.56	0.13	3.05	3.06
16.9	0.87	1.28	3.08	0.60	0.14	3.18	3.16
17.1	0.92	1.36	3.23	0.64	0.15	3.32	3.32
17.3	0.99	1.44	3.45	0.69	0.16	3.48	3.48
17.5	1.06	1.54	3.62	0.74	0.18	3.70	3.66
17.7	1.14	1.66	3.80	0.78	0.20	3.90	3.88
17.9	1.21	1.75	3.94	0.82	0.22	4.06	4.04
18.1	1.28	1.85	4.10	0.86	0.24	4.23	4.20
18.3	1.35	1.97	4.37	0.90	0.26	4.44	4.40
18.5	1.45	2.08	4.53	0.94	0.28	4.65	4.58
18.7	1.52	2.19	4.72	0.97	0.30	4.82	4.80
18.9	1.58	2.32	4.90	1.00	0.32	5.00	4.97
19.1	1.62	2.43	5.07	1.02	0.34	5.20	5.14
19.3	1.66	2.53	5.22	1.04	0.36	5.36	5.32
19.5	1.68	2.63	5.40	1.05	0.38	5.50	5.50
19.7	1.69	2.71	5.55	1.06	0.39	5.70	5.68
19.9	1.70	2.80	5.68	1.06	0.41	5.87	5.82
20.1	1.71	2.88	5.80	1.07	0.42	6.00	5.95
20.3	1.72	2.95	5.88	1.07	0.44	6.10	6.05
20.5	1.73	3.02	5.96	1.07	0.45	6.20	6.13
20.7	1.73	3.08	6.05	1.07	0.46	6.30	6.22
20.9	1.74	3.15	6.08	1.07	0.47	6.38	6.30
21.1	1.74	3.20		1.07	0.48	6.44	6.40
21.3	1.75	3.25		1.07	0.49	6.50	6.50
21.5	1.76	3.30		1.06	0.50	6.56	6.60

Table A.3: Empirical ridgelines for M37.

r	$u-g$	$g-r$	$g-i$	$g-z$	$g-K_S$	$J-K_S$	$H-K_S$	$g-[3.6]$	$g-[4.5]$
13.5	1.25	0.37		0.50			0.07	0.40	1.70
13.7	1.26	0.39	0.52	0.54	1.66	0.31	0.06	1.74	1.70
13.9	1.29	0.41	0.54	0.57	1.71	0.33	0.06	1.77	1.73
14.1	1.33	0.43	0.57	0.61	1.79	0.35	0.06	1.84	1.80
14.3	1.38	0.47	0.61	0.66	1.88	0.37	0.07	1.93	1.88
14.5	1.44	0.51	0.67	0.72	1.97	0.39	0.07	2.03	1.99
14.7	1.52	0.55	0.72	0.79	2.05	0.43	0.07	2.09	2.05
14.9	1.60	0.58	0.77	0.85	2.20	0.45	0.08	2.25	2.21
15.1	1.69	0.62	0.82	0.91	2.30	0.48	0.08	2.34	2.31
15.3	1.79	0.66	0.88	0.99	2.43	0.51	0.08	2.47	2.43
15.5	1.90	0.71	0.95	1.08	2.63	0.55	0.09	2.66	2.61
15.7	2.01	0.77	1.04	1.19	2.78	0.59	0.09	2.81	2.75
15.9	2.14	0.84	1.14	1.30	2.97	0.62	0.10	3.01	2.93
16.1	2.26	0.91	1.23	1.41	3.10	0.65	0.10	3.15	3.06
16.3	2.37	0.99	1.34	1.53	3.28	0.68	0.10	3.34	3.25
16.5	2.47	1.07	1.47	1.70	3.46	0.70	0.11	3.54	3.45
16.7	2.53	1.15	1.58	1.83	3.65	0.73	0.12	3.74	3.64
16.9	2.59	1.22	1.67	1.94	3.83	0.76	0.13	3.93	3.83
17.1	2.64	1.28	1.77	2.07	4.00	0.79	0.14	4.10	4.04
17.3	2.66	1.33	1.87	2.18	4.22	0.82	0.15	4.31	4.28
17.5	2.65	1.36	1.95	2.30	4.40	0.85	0.18	4.50	4.47
17.7	2.63	1.39	2.05	2.42	4.53	0.88	0.21	4.63	4.63
17.9	2.62	1.42	2.13	2.54	4.67	0.89	0.22	4.79	4.80
18.1	2.65	1.44	2.19	2.63	4.77	0.90	0.23	4.91	4.93
18.3		1.46	2.24	2.70	4.86	0.91	0.24	5.02	5.04
18.5		1.45	2.29	2.78	4.95	0.91	0.25	5.13	5.15
18.7		1.45	2.34	2.84	5.03	0.91	0.26	5.22	5.24
18.9		1.46	2.39	2.91	5.10	0.91	0.27	5.30	5.32
19.1		1.46	2.43	2.97	5.17	0.91	0.28	5.38	5.40
19.3		1.45	2.47	3.04	5.27	0.92	0.29	5.47	5.50
19.5		1.45	2.52	3.12	5.34	0.92	0.30	5.54	5.58
19.7		1.45	2.57	3.19	5.40	0.92	0.30	5.60	5.65
19.9		1.46	2.61	3.25	5.46	0.92	0.29	5.67	5.72
20.1		1.48	2.63	3.29	5.57	0.92	0.28	5.78	5.84
20.3		1.47	2.67	3.34	5.59	0.91	0.28	5.81	5.88
20.5		1.46	2.71	3.42	5.63	0.90	0.28	5.86	5.94
20.7		1.49	2.71	3.42	5.68	0.89	0.28	5.92	6.01
20.9		1.50	2.68	3.33	5.74	0.88	0.28	5.99	6.09

Table A.4: Empirical ridgelines for M67. *ugriz* ridgelines copied from (An et al. 2009).

r	$u-g$	$g-r$	$g-i$	$g-z$	$g-K_S$	$J-K_S$	$H-K_S$	$g-[3.6]$	$g-[4.5]$
14.5	1.13	0.24	0.30	0.29	1.30	0.26	0.06	1.30	1.30
14.7	1.12	0.21	0.27	0.27	1.25	0.25	0.06	1.27	1.30
14.9	1.11	0.21	0.27	0.27	1.25	0.25	0.05	1.27	1.30
15.1	1.11	0.23	0.27	0.28	1.24	0.25	0.05	1.29	1.30
15.3	1.10	0.23	0.29	0.30	1.27	0.25	0.04	1.32	1.33
15.5	1.10	0.26	0.33	0.33	1.35	0.26	0.04	1.40	1.40
15.7	1.10	0.28	0.37	0.38	1.42	0.28	0.04	1.46	1.46
15.9	1.11	0.30	0.41	0.42	1.50	0.29	0.04	1.53	1.52
16.1	1.13	0.33	0.45	0.46	1.57	0.31	0.04	1.60	1.61
16.3	1.16	0.35	0.48	0.51	1.64	0.33	0.04	1.66	1.70
16.5	1.19	0.38	0.52	0.56	1.70	0.35	0.04	1.74	1.76
16.7	1.23	0.42	0.57	0.61	1.80	0.37	0.05	1.84	1.83
16.9	1.29	0.45	0.61	0.67	1.88	0.39	0.06	1.94	1.94
17.1	1.36	0.49	0.67	0.73	1.97	0.42	0.07	2.05	2.05
17.3	1.45	0.52	0.72	0.80	2.10	0.44	0.08	2.16	2.18
17.5	1.55	0.56	0.79	0.88	2.23	0.47	0.09	2.30	2.26
17.7	1.66	0.61	0.86	0.97	2.39	0.50	0.11	2.48	2.42
17.9	1.78	0.68	0.91	1.05	2.52	0.54	0.12	2.60	2.55
18.1	1.90	0.73	0.99	1.14	2.70	0.59	0.13	2.76	2.72
18.3	2.02	0.81	1.09	1.25	2.88	0.63	0.14	2.92	2.90
18.5	2.13	0.88	1.19	1.38	3.03	0.66	0.16	3.14	3.10
18.7	2.29	0.96	1.29	1.49	3.24	0.70	0.18	3.32	3.30
18.9		1.03	1.40	1.61	3.43	0.74	0.20	3.50	3.50
19.1		1.12	1.53	1.76	3.60	0.77	0.22	3.65	3.66
19.3		1.20	1.65	1.90	3.80	0.80	0.24	3.88	3.87
19.5		1.25	1.75	2.03	3.98	0.83	0.26	4.07	4.10
19.7		1.31	1.84	2.15	4.13	0.85	0.28	4.30	4.25
19.9		1.36	1.94	2.30	4.30	0.86	0.30	4.47	4.44
20.1		1.39	2.03	2.51	4.41	0.86	0.31	4.65	4.65
20.3		1.42	2.11	2.62	4.55	0.86	0.33	4.80	4.79
20.5		1.44	2.18	2.67	4.68	0.86	0.35	4.94	5.00
20.7		1.45	2.25	2.73	4.80	0.86	0.37	5.08	5.20
20.9		1.46	2.31	2.78	4.90	0.86	0.39		
21.1		1.46	2.35	2.85	5.00	0.86	0.40		
21.3		1.46	2.39	2.93	5.08	0.86	0.41		

Table A.5: Empirical ridgelines for NGC 2420. $ugriz$ ridgelines copied from (An et al. 2009).

Bibliography

Abazajian, K. N., Adelman-McCarthy, J. K., Agüeros, M. A., Allam, S. S., Allende Prieto, C., An, D., Anderson, K. S. J., Anderson, S. F., Annis, J., Bahcall, N. A., Bailer-Jones, C. A. L., Barentine, J. C., Bassett, B. A., Becker, A. C., Beers, T. C., Bell, E. F., Belokurov, V., Berlind, A. A., Berman, E. F., Bernardi, M., Bickerton, S. J., Bizyaev, D., Blakeslee, J. P., Blanton, M. R., Bochanski, J. J., Boroski, W. N., Brewington, H. J., Brinchmann, J., Brinkmann, J., Brunner, R. J., Budavari, T., Carey, L. N., Carliles, S., Carr, M. A., Castander, F. J., Cinabro, D., Connolly, A. J., Csabai, I., Cunha, C. E., Czarapata, P. C., Davenport, J. R. A., de Haas, E., Dilday, B., Doi, M., Eisenstein, D. J., Evans, M. L., Evans, N. W., Fan, X., Friedman, S. D., Frieman, J. A., Fukugita, M., Gänsicke, B. T., Gates, E., Gillespie, B., Gilmore, G., Gonzalez, B., Gonzalez, C. F., Grebel, E. K., Gunn, J. E., Györy, Z., Hall, P. B., Harding, P., Harris, F. H., Harvanek, M., Hawley, S. L., Hayes, J. J. E., Heckman, T. M., Hendry, J. S., Hennessy, G. S., Hindsley, R. B., Hoblitt, J., Hogan, C. J., Hogg, D. W., Holtzman, J. A., Hyde, J. B., Ichikawa, S.-i., Ichikawa, T., Im, M., Ivezić, Z., Jester, S., Jiang, L., Johnson, J. A., Jorgensen, A. M., Jurić, M., Kent, S. M., Kessler, R., Kleinman, S. J., Knapp, G. R., Konishi, K., Kron, R. G., Krzesinski, J., Kuropatkin, N., Lampeitl, H., Lebedeva, S., Lee, M. G., Lee, Y. S., French Leger, R., Lépine, S., Li, N., Lima, M., Lin, H., Long, D. C., Loomis, C. P., Loveday, J., Lupton, R. H., Magnier, E., Malanushenko, O., Malanushenko, V., Mandelbaum, R., Margon, B., Marriner, J. P., Martínez-Delgado, D., Matsubara, T., McGehee, P. M., McKay, T. A., Meiksin, A., Morrison, H. L., Mullally, F., Munn, J. A., Murphy, T., Nash, T., Nebot, A., Neilsen, E. H. J., Newberg, H. J., Newman, P. R., Nichol, R. C., Nicinski, T., Nieto-Santisteban, M., Nitta, A., Okamura, S., Oravetz, D. J., Ostriker, J. P., Owen, R., Padmanabhan, N., Pan, K., Park, C., Pauls, G., Peoples, J. J., Percival, W. J., Pier, J. R., Pope, A. C., Pourbaix, D., Price, P. A., Purger, N., Quinn, T., Raddick, M. J., Re Fiorentin, P., Richards, G. T., Richmond, M. W., Riess, A. G., Rix, H.-W., Rockosi, C. M., Sako, M., Schlegel, D. J., Schneider, D. P., Scholz, R.-D., Schreiber, M. R., Schwobe, A. D., Seljak, U., Sesar, B., Sheldon, E., Shimasaku, K., Sibley, V. C., Simmons, A. E., Sivarani, T., Allyn Smith, J., Smith, M. C., Smolčić, V., Snedden, S. A., Stebbins, A., Steinmetz, M., Stoughton, C., Strauss, M. A., SubbaRao, M., Suto, Y., Szalay, A. S., Szapudi, I., Szkody, P., Tanaka, M., Tegmark, M., Teodoro, L. F. A., Thakar, A. R., Tremonti, C. A., Tucker, D. L., Uomoto, A., vanden Berk, D. E., Vandenberg, J., Vidrih, S., Vogeley, M. S., Voges, W., Vogt, N. P., Wadadekar, Y., Watters, S., Weinberg, D. H., West, A. A., White, S. D. M., Wilhite, B. C., Wonders, A. C., Yanny, B., Yocum, D. R., York, D. G., Zehavi, I., Zibetti, S.,

- & Zucker, D. B. 2009, *The Astrophysical Journal Supplement*, 182, 543
- Alexander, D. R. & Ferguson, J. W. 1994, *The Astrophysical Journal*, 437, 879
- Allard, F., Homeier, D., & Freytag, B. 2012, *Philosophical Transactions of the Royal Society A: Mathematical*, 370, 2765
- An, D., Pinsonneault, M. H., Masseron, T., Delahaye, F., Johnson, J. A., Terndrup, D. M., Beers, T. C., Ivans, I. I., & Ivezić, Z. 2009, *The Astrophysical Journal*, 700, 523
- Balaguer-Núñez, L., Jordi, C., Galadí-Enríquez, D., & Zhao, J. L. 2004, *Astronomy and Astrophysics*, 426, 819
- Barmby, P. & Huchra, J. P. 2001, *The Astronomical Journal*, 122, 2458
- Benjamin, R. A., Churchwell, E., Babler, B. L., Bania, T. M., Clemens, D. P., Cohen, M., Dickey, J. M., Indebetouw, R., Jackson, J. M., Kobulnicky, H. A., Lazarian, A., Marston, A. P., Mathis, J. S., Meade, M. R., Seager, S., Stolovy, S. R., Watson, C., Whitney, B. A., Wolff, M. J., & Wolfire, M. G. 2003, *The Publications of the Astronomical Society of the Pacific*, 115, 953
- Bessell, M. S. 1990, *Astronomical Society of the Pacific*, 102, 1181
- Binney, J. & Merrifield, M. 1998, *Galactic Astronomy* (Princeton University Press)
- Bressan, A., Bressan, A., Marigo, P., Girardi, L., Salasnich, B., Salasnich, B., Dal Cero, C., Dal Cero, C., Rubele, S., Rubele, S., Nanni, A., & Nanni, A. 2012, *Monthly Notices of the Royal Astronomical Society*, 427, 127
- Caffau, E., Ludwig, H. G., Steffen, M., Freytag, B., & Bonifacio, P. 2011, *Solar Physics*, 268, 255
- Cardelli, J. A., Clayton, G. C., & Mathis, J. S. 1989, *Astrophysical Journal*, 345, 245
- Carney, B. W., Lee, J.-W., & Dodson, B. 2005, *The Astronomical Journal*, 129, 656
- Carroll, B. W. & Ostlie, D. A. 2006, *Introduction to Modern Astrophysics*, 2nd edn.
- Castelli, F. & Kurucz, R. L. 2003, *Modelling of Stellar Atmospheres*, 210
- Chapman, N. L., Mundy, L. G., Lai, S.-P., & Evans II, N. J. 2008, *arXiv.org*, 496
- de Grijs, R., Li, C., Zheng, Y., Deng, L., Hu, Y., Kouwenhoven, M. B. N., & Wicker, J. E. 2013, *The Astrophysical Journal*, 765, 4
- Dias, W. S., Alessi, B. S., Moitinho, A., & Lépine, J. R. D. 2002, *Astronomy and Astrophysics*, 389, 871
- Dotter, A., Chaboyer, B., Jevremović, D., Baron, E., Ferguson, J. W., Sarajedini, A., & Anderson, J. 2007, *The Astronomical Journal*, 134, 376

- Dziembowski, W. A., Pamiatnykh, A. A., & Sienkiewicz, R. 1992, *Acta Astronomica* (ISSN 0001-5237), 42, 5
- Elson, R. A. W., Sigurdsson, S., Davies, M., Hurley, J., & Gilmore, G. 1998, *Monthly Notices of the Royal Astronomical Society*, 300, 857
- Fan, X. 1999, *The Astronomical Journal*, 117, 2528
- Fazio, G. G., Hora, J. L., Allen, L. E., Ashby, M. L. N., Barmby, P., Deutsch, L. K., Huang, J. S., Kleiner, S., Marengo, M., Megeath, S. T., Melnick, G. J., Pahre, M. A., Patten, B. M., Polizotti, J., Smith, H. A., Taylor, R. S., Wang, Z., Willner, S. P., Hoffmann, W. F., Pipher, J. L., Forrest, W. J., McMurty, C. W., McCreight, C. R., McKelvey, M. E., McMurray, R. E., Koch, D. G., Moseley, S. H., Arendt, R. G., Mentzell, J. E., Marx, C. T., Losch, P., Mayman, P., Eichhorn, W., Krebs, D., Jhabvala, M., Gezari, D. Y., Fixsen, D. J., Flores, J., Shakoorzadeh, K., Jungo, R., Hakun, C., Workman, L., Karpati, G., Kichak, R., Whitley, R., Mann, S., Tollestrup, E. V., Eisenhardt, P., Stern, D., Gorjian, V., Bhattacharya, B., Carey, S., Nelson, B. O., Glaccum, W. J., Lacy, M., Lowrance, P. J., Laine, S., Reach, W. T., Stauffer, J. A., Surace, J. A., Wilson, G., Wright, E. L., Hoffman, A., Domingo, G., & Cohen, M. 2004, *The Astrophysical Journal Supplement Series*, 154, 10
- Ferguson, J. W., Alexander, D. R., Allard, F., Barman, T., Bodnarik, J. G., Hauschildt, P. H., Heffner-Wong, A., & Tamanai, A. 2005, *The Astrophysical Journal*, 623, 585
- Fukugita, M., Ichikawa, T., Gunn, J. E., Doi, M., Shimasaku, K., & Schneider, D. P. 1996, *The Astronomical Journal*, 111, 1748
- Geller, A. M., de Grijs, R., Li, C., & Hurley, J. R. 2013, *The Astrophysical Journal*, 779, 30
- . 2015, arXiv.org, 5198
- Geller, A. M. & Mathieu, R. D. 2012, *The Astronomical Journal*, 144, 54
- Geller, A. M., Mathieu, R. D., Braden, E. K., Meibom, S., Platais, I., & Dolan, C. J. 2010, *The Astronomical Journal*, 139, 1383
- Geller, A. M., Mathieu, R. D., Harris, H. C., & McClure, R. D. 2008, *The Astronomical Journal*, 135, 2264
- . 2009, *The Astronomical Journal*, 137, 3743
- Girardi, L., Bertelli, G., Bressan, A., Chiosi, C., Groenewegen, M. A. T., Marigo, P., Salasnich, B., & Weiss, A. 2002, *Astronomy and Astrophysics*, 391, 195
- Gozzoli, E., Tosi, M., Marconi, G., & Bragaglia, A. 1996, *Monthly Notices of the Royal Astronomical Society*, 283, 66
- Grevesse, N. & Noels, A. 1993, *Physica Scripta T*, 47, 133

- Grevesse, N. & Sauval, A. J. 1998, *Space Science Reviews*, 85, 161
- Gunn, J. E., Siegmund, W. A., & al, E. J. M. e. 2006, *arXiv.org*, 2332
- Harris, W. E. 1996, *Astronomical Journal* v.112, 112, 1487
- Hartman, J. D., Gaudi, B. S., Holman, M. J., McLeod, B. A., Stanek, K. Z., Barranco, J. A., Pinsonneault, M. H., Meibom, S., & Kalirai, J. S. 2008, *The Astrophysical Journal*, 675, 1233
- Heggie, D. C. 1975, *Monthly Notices of the Royal Astronomical Society*, 173, 729
- Hole, K. T., Geller, A. M., Mathieu, R. D., Platais, I., Meibom, S., & Latham, D. W. 2009, *The Astronomical Journal*, 138, 159
- Hurley, J. & Tout, C. A. 1998, *Monthly Notices of the Royal Astronomical Society*, 300, 977
- Hurley, J. R., Pols, O. R., Aarseth, S. J., & Tout, C. A. 2005, *Monthly Notices of the Royal Astronomical Society*, 363, 293
- Hurley, J. R., Tout, C. A., Aarseth, S. J., & Pols, O. R. 2001, *Monthly Notices of the Royal Astronomical Society*, 323, 630
- Iglesias, C. A. & Rogers, F. J. 1993, *Astrophysical Journal*, 412, 752
- . 1996, *Astrophysical Journal* v.464, 464, 943
- Irwin, A. W. 2004, Technical Report (<http://freeeos.sourceforge.net>)
- Jones, B. F. & Prosser, C. F. 1996, *The Astronomical Journal*, 111, 1193
- Kalirai, J. S., Ventura, P., Richer, H. B., Fahlman, G. G., Durrell, P. R., D'Antona, F., & Marconi, G. 2001, *The Astronomical Journal*, 122, 3239
- Kippenhahn, R., Thomas, H. C., & Weigert, A. 1965, *Zeitschrift für Astrophysik*, 61, 241
- Lada, C. J. & Lada, E. A. 2003, *Annual Review of Astronomy & Astrophysics*, 41, 57
- Lejeune, T., Cuisinier, F., & Buser, R. 1998, *Astronomy and Astrophysics Supplement*, 130, 65
- Li, C., de Grijs, R., & Deng, L. 2013, *Monthly Notices of the Royal Astronomical Society*, 436, 1497
- Marigo, P. & Aringer, B. 2009, *Astronomy and Astrophysics*, 508, 1539
- Mathieu, R. D. & Latham, D. W. 1986, *The Astronomical Journal*, 92, 1364
- Mathieu, R. D., Latham, D. W., & Milone, A. E. 1997, *The Third Pacific Rim Conference on Recent Development on Binary Star Research. Proceedings of a conference sponsored by Chiang Mai University*, 130, 113

- Mihalas, D., Hummer, D. G., Mihalas, B. W., & Daepfen, W. 1990, *Astrophysical Journal*, 350, 300
- Milliman, K. E., Mathieu, R. D., Geller, A. M., Gosnell, N. M., Meibom, S., & Platais, I. 2014, *The Astronomical Journal*, 148, 38
- Milone, A. P., Piotto, G., Bedin, L. R., Aparicio, A., Anderson, J., Sarajedini, A., Marino, A. F., Moretti, A., Davies, M. B., Chaboyer, B., Dotter, A., Hempel, M., Marín-Franch, A., Majewski, S., Paust, N. E. Q., Reid, I. N., Rosenberg, A., & Siegel, M. 2012, *Astronomy and Astrophysics*, 540, 16
- Moyano Loyola, G. R. I. & Hurley, J. R. 2013, *Monthly Notices of the Royal Astronomical Society*, 434, 2509
- Pandey, A. K., Sharma, S., Upadhyay, K., Ogura, K., Sandhu, T. S., Mito, H., & Sagar, R. 2007, *Publications of the Astronomical Society of Japan*, 59, 547
- Piotto, G., Bedin, L. R., Anderson, J., King, I. R., Cassisi, S., Milone, A. P., Villanova, S., Pietrinferni, A., & Renzini, A. 2007, *The Astrophysical Journal*, 661, L53
- Platais, I., Kozhurina-Platais, V., Mathieu, R. D., Girard, T. M., & van Altena, W. F. 2003, *The Astronomical Journal*, 126, 2922
- Probst, R. G., Gaughan, N., Abraham, M., Andrew, J., Daly, P., Hileman, E., Huntten, M., Liang, M., Merrill, K. M., Repp, R., & Shaw, R. 2004, in *Ground-based Instrumentation for Astronomy*. Edited by Alan F. M. Moorwood and Iye Masanori. *Proceedings of the SPIE*, ed. A. F. M. Moorwood & M. Iye, National Optical Astronomy Observatory, USA (SPIE), 1716–1724
- Raghavan, D. & McAlister, H. A. 2009, *American Astronomical Society*, 213, 387
- Rogers, F. J., Swenson, F. J., & Iglesias, C. A. 1996, *Astrophysical Journal* v.456, 456, 902
- Sanner, J., Altmann, M., Brunzendorf, J., & Geffert, M. 2000, *Astronomy and Astrophysics*, 357, 471
- Sawyer, D. G., Daly, P. N., Howell, S. B., Huntten, M. R., & Schweiker, H. 2010, in *Proceedings of the SPIE*, ed. I. S. McLean, S. K. Ramsay, & H. Takami, National Optical Astronomy Observatory, United States (SPIE), 77353A–77353A–12
- Sharma, S., Pandey, A. K., Ogura, K., Mito, H., Tarusawa, K., & Sagar, R. 2006, *The Astronomical Journal*, 132, 1669
- Skrutskie, M. F., Cutri, R. M., Stiening, R., Weinberg, M. D., Schneider, S., Carpenter, J. M., Beichman, C., Capps, R., Chester, T., Elias, J., Huchra, J., Liebert, J., Lonsdale, C., Monet, D. G., Price, S., Seitzer, P., Jarrett, T., Kirkpatrick, J. D., Gizis, J. E., Howard, E., Evans, T., Fowler, J., Fullmer, L., Hurt, R., Light, R., Kopan, E. L., Marsh, K. A., McCallon, H. L., Tam, R., Van Dyk, S., & Wheelock, S. 2006, *The Astronomical Journal*, 131, 1163

- Stetson, P. B. 1987, *Astronomical Society of the Pacific*, 99, 191
- Stetson, P. B., McClure, R. D., & Vandenberg, D. A. 2004, *The Publications of the Astronomical Society of the Pacific*, 116, 1012
- Thompson, B., Frinchaboy, P., Kinemuchi, K., Sarajedini, A., & Cohen, R. 2014, *The Astronomical Journal*, 148, 85
- von Hippel, T. & Sarajedini, A. 1998, *The Astronomical Journal*, 116, 1789
- Wright, E. L., Eisenhardt, P. R. M., Mainzer, A. K., Mainzer, A. K., Ressler, M. E., Cutri, R. M., Jarrett, T., Kirkpatrick, J. D., Padgett, D., McMillan, R. S., Skrutskie, M., Stanford, S. A., Cohen, M., Walker, R. G., Mather, J. C., Leisawitz, D., Gautier, T. N. I., Gautier, T. N. I., McLean, I., Benford, D., Lonsdale, C. J., Blain, A., Mendez, B., Irace, W. R., Duval, V., Liu, F., Royer, D., Heinrichsen, I., Howard, J., Shannon, M., Kendall, M., Walsh, A. L., Larsen, M., Cardon, J. G., Schick, S., Schwalm, M., Abid, M., Fabinsky, B., Naes, L., & Tsai, C.-W. 2010, *The Astronomical Journal*, 140, 1868
- Yadav, R. K. S., Bedin, L. R., Piotto, G., Anderson, J., Cassisi, S., Villanova, S., Platais, I., Pasquini, L., Momany, Y., & Sagar, R. 2008, *Astronomy and Astrophysics*, 484, 609
- Yi, S., Demarque, P., Kim, Y.-C., Lee, Y.-W., Ree, C. H., Lejeune, T., & Barnes, S. 2001, *The Astrophysical Journal Supplement Series*, 136, 417

VITA

Personal Background Benjamin Adler Thompson
Oberlin, OH
Son of Robert and Janis Thompson
Married Christina Marie Madison, June 27, 2014

Education Diploma, Oberlin High School, Oberlin, OH, 2006
Bachelor of Arts, Astrophysics, Ohio Wesleyan University,
Delaware, OH, 2010
Doctor of Philosophy, Physics, Texas Christian University,
Fort Worth, 2015

Experience Summer research assistant, Oberlin College, Oberlin, OH,
2009-2010
Teaching assistantship, Texas Christian University, Fort
Worth, 2010-2014
Research assistantship, Texas Christian University, Fort
Worth, 2014-2015

Professional Memberships American Astronomical Society

ABSTRACT

BINARY INFORMATION FROM OPEN CLUSTERS USING SEDS (BINOCS) PROJECT: THE DYNAMICAL EVOLUTION OF THE BINARY POPULATION IN CLUSTER ENVIRONMENTS

by Benjamin A Thompson, Ph.D., 2015
Department of Physics and Astronomy
Texas Christian University

Peter M. Frinchaboy III, Assistant Professor of Physics

A majority of stars are formed in open clusters, and then ejected into the Galactic field population through tidal effects from external masses, as well as internal gravitational interactions. Therefore, understanding the internal dynamics of open clusters, through N-Body simulations, will inform the growth of the Galactic stellar population. A major input into these N-Body simulations is the frequency and mass distribution of binary star systems, which are currently based on statistics derived from the field population, but the distributions of binaries in clusters may be different. Current binary detection techniques, such as radial velocity surveys, have drawbacks which limit their usefulness for detailed studies over large mass ranges. As presented in the literature, different mass ranges may produce different interpretations of the observed binary population, e.g, as published recently for NGC 1818. A clearer picture of the binary population, covering a wide mass range, is needed to improve the understanding of cluster binary populations, which will inform cluster simulations. We introduce a new binary detection method, Binary INformation from Open Clusters Using SEDs (BINOCS). Using newly-observed

multi-wavelength photometric catalogs (0.3 – 8 micron) of the key open clusters M35, M36, M37, M67 and NGC 2420, the BINOCs method is able to determine accurate component masses for unresolved cluster binaries. We present results on the dynamical evolution of binaries from 0.4 – 2.5 M_{\odot} within these key clusters, and explore how these results change with mass.